The Dissertation Committee for Feng He Certifies that this is the approved version of the following Dissertation:

COHERENT PHONON DYNAMICS IN SEMICONDUCTORS

Committee:

Yaguo Wang, Supervisor

Raymond L. Orbach

Li Shi

Seth R. Bank

Chih-Kang Shih

COHERENT PHONON DYNAMICS IN SEMICONDUCTORS

by

Feng He

Dissertation

Presented to the Faculty of the Graduate School of
The University of Texas at Austin
in Partial Fulfillment
of the Requirements
for the Degree of

Doctor of Philosophy

The University of Texas at Austin
August 2018

Dedication

To my parents and grandparents

Acknowledgements

First of all, I would like to thank my supervisor Dr. Yaguo Wang for her support. I am very grateful for her trust and guidance in my research and for the opportunities she provided to work at various laboratories. I would also like to thank my committee members: Prof. Raymond Orbach, Prof. Li Shi, Prof. Seth R. Bank and Prof. Chih-Kang Shih for serving as my committee members and providing very valuable feedback on my research.

In addition, I would like to express my utmost gratitude to Prof. Raymond Orbach for proving a weekly discussion on my research and all the valuable suggestions. I would like to thank Prof. Seth R. Bank for giving suggestions from the material growth side. I thank Prof. Afu Lin for proving Raman scattering set up.

My sincere thanks go to Prof. Wenzhi Wu, who taught me the pump-probe experiment and shared experimental experiences with me. I would like to thank my lab mates: Dr. Ke Chen, Xianghai Meng, Jihoon Jeong, Yongjian Zhou, Sarah Cameron and Madison Facchini for all their help and valuable discussions. I would also like to thank our collaborators: Nathanal Sheehan, Emily S. Walker and Rodolfo Salas for proving MBE growth samples for us to measure and Nathanial Sheehan for teaching me the membrane transfer process. I thank Jason Kim in Prof. Afu Lin's group for providing help in Raman scattering and PL measurement.

I want to express special thanks to Dr. Samual Teitelbaum (Stanford University) and Dr. Michael Först (Max Planck Institute) for the discussion of nonlinear phononics and for sharing their simulation code with me.

Last but not least, I would like to thank my father, Mr. Riyang He and my mother, Mrs. Zhou Chen for their lifetime support and encouragement. They taught me to be optimistic and how to deal with difficulties. To all my friends, thank you for being around, I will not feel lonely.

Abstract

COHERENT PHONON DYNAMICS IN SEMICONDUCTORS

Feng He, Ph.D.
The University of Texas at Austin, 2018

Supervisor: Yaguo Wang

Ultrafast pump-probe spectroscopy is a powerful experimental technique to study the light-matter interaction and ultrafast dynamics in solids. In many semiconductors, under ultrafast laser irradiation, phonons (quantized lattice vibrations) with both temporal and spatial coherence can be generated conveniently. When a stronger laser pulse excites coherent phonons that induce refractive index change, and thus the reflectivity change of the materials, the time-dependent phonon dynamics can be detected by a delayed probe pulse. The generation and detection of coherent phonons provide an opportunity to understand the fundamental physics between light and matter interaction, as well as a path to manipulate other physical processes, for applications such as sound amplification stimulated emission (SASER), phonon mode manipulation, ultrafast phase switching, superconductivity enhancement and manipulation of magnetism[1-5].

This thesis presents a series of time-resolved studies of coherent phonons in three semiconductor systems, including bulk CdSe, Bi_2Te_3/Sb_2Te_3 superlattice and GaAs/AlAs superlattice. In bulk CdSe, a material extensively studied for quantum dot photoelectronics, coherent phonons serve as the probe for the reversible ultrafast melting. In Bi_2Te_3/Sb_2Te_3 superlattice, a material system used for thermoelectrics, the coherent thermal phonons are excited directly and are found to be selectively filtered in the superlattice structure compared with bulk materials. In GaAs/AlAs superlattice, a quantum well structure for photodetectors and lasers, a strong quantum coherent coupling among different phonon modes is observed. A similar coherent coupling between photons and phonons has been used to induce and enhance superconductivity[6,7] and mimic the magnetic field[8]. However, direct observation of nonlinear phonon coupling is rare. Moreover, a novel technique based on surface plasmon resonance has been implemented into the pump-probe spectrometer to improve detection efficiency.

Keywords: pump-probe technique, coherent phonon, quantum coherent coupling

Table of Contents

List of Tables

List of Figures

Introduction

Light-matter interaction is not only important in physics, but also belongs to our daily life. It is the mechanism which governs our perception of colors, the feeling of the sun on our skin and nowadays our chance to enjoy the high-speed Internet.

To study light-matter interaction and carrier dynamics, the ultrafast pump-probe spectroscopy is a powerful tool. In the pump-probe experiment, the system under study is first pumped with a short laser pulse and excited carriers are generated. The excited carriers will modulate the dielectric function, and thus the refractive index of the material. Then this change will be probed by a second, less intense laser pulse by measuring the reflection/transmission change at time delay τ depending on whether the material is opaque or transparent as long as the lifetime of the excitations is longer than the pulse duration.

The interest in the phonons in semiconductors is driven by their important role in energy transfer. With an ultrafast pulse, the temporal and spatial coherence of phonons will be generated in the solids. The coherent phonons give an opportunity to understand the fundamental physics between light and matter interaction and also a path to manipulate other physical processes[1-5].

In the case of coherent phonons, semi-classical descriptions have been addressed. Historically, impulsive stimulated Raman scattering (ISRS) was first proposed in the 70s and has been successfully applied to explain the coherent phonon generation in transparent crystals and liquids[9-11]. The displacive excitation of coherent phonons (DECP) was first proposed in 1992[12] to explain observations in certain opaque materials, such as Bismuth (Bi), Antimony (Sb), Telluride (Te), etc.,[13] which cannot be explained by ISRS[13]. Afterwards, additional experimental results led to theoretical study which concluded that DECP is just a special case of ISRS, and only matters when the imaginary part of the Raman tensor dominates[14-16].

This thesis presents the time-resolved studies of coherent phonons in semiconductors. The work presented here is based on three pump-probe experiments in semiconductors. The three experiments are conceptually similar: a strong laser pulse excites coherent phonons and a delayed probe pulse measures the reflectivity change of the samples as a function of time. Different properties have been pursued from three different semiconductors. The first experiment shows the thermal reversible ultrafast melting in bulk CdSe. The second experiment directly measures the coherent thermal phonons in the Bi_2Te_3/Sb_2Te_3 superlattice and compare with that in bulk Bi_2Te_3. And the third experiment reveals the evidence of quantum coherent coupling in the GaAs/AlAs superlattice.

This work is presented in the following scheme:

- In Chapter 1, a theoretical background needed for the description of photon and phonon dynamics and their interactions in quantum mechanics is given. A description of a bosonic system is presented and the generation and detection mechanisms for coherent phonons are described. A new approach to understand heat transport in superlattices, i.e. coherent heat transport is then introduced.

- In Chapter 2, the pump-probe technique is described in detail. The characterization of our experimental systems is discussed first and then two set-ups with specific experimental steps are presented.
- Chapter 3 is dedicated to the measurements of coherent phonons in three different semiconductor materials. The first section shows the thermal reversible ultrafast melting in bulk CdSe. The second section directly measures the coherent thermal phonons in the Bi_2Te_3/Sb_2Te_3 superlattice and compare with bulk Bi_2Te_3. The third section reveals the evidence of quantum coherent coupling in the GaAs/AlAs superlattice.
- Chapter 4 describes the surface plasmon resonance (SPR) technique. The concept of SPR and the two common configurations with prisms, Kretschmann and Otto configuration, to generate SPR are briefly introduced. Then the methods for preparing the samples for SPR and how SPR is implement into the pump-probe measurement with some of the results.
- The last Chapter summarizes all the results described in this thesis and the prospective of the research project.

- Finally, a perturbation process as well as the Matlab code for solving coupled equations of motion are collected in the Appendices.

Chapter 1: Coherent Phonons

At finite temperature, atoms in materials vibrate around their equilibrium positions with amplitudes that depend on the temperature. They are always in motion and even at zero temperature, according to quantum mechanics, there will be zero-point vibrations[17]. Since in crystals these vibrations must satisfy periodic boundary conditions due to the crystal symmetry, atomic vibrations are then collective and can be analyzed in terms of normal modes. Therefore, phonons are defined as quantized lattice vibrations, characterized with frequency ω, wave vector k, phonon velocity v and lifetime τ. Usually, the atomic motions at different locations in the crystal are at different stages and their relative phase is randomized. We can call them incoherent phonons. Under some special conditions, for example, with impulsive force, the atoms will keep in pace with their neighbors, or stay in phase; we can then call these atomics motions coherent phonons because they can now interfere with each other like waves.

There have been a lot of works that report observation of coherent phonons in a variety of transparent[18-21] and opaque materials[22-36].

The goal of this chapter is to show physical mechanisms of excitation of coherent phonons by ultrashort pulses. The first section briefly covers the Bosonic system, especially the quantum states and quantum coherent coupling between photon and phonon, which aims to describe phonons as analogous to photons. The second section reveals the generation and detection mechanisms for coherent phonons. The third section introduces a new approach to understand heat transport in superlattices, i.e. coherent heat transport.

1.1 BOSONIC SYSTEM

In quantum mechanics, a boson is a particle that follows Bose-Einstein statistics. Radiation fields (e.g. light) and intermolecular vibrations in a lattice are typical examples of bosonic system and they can be modeled as a harmonic oscillator. In this section, the bosonic system is briefly introduced.

1.1.1 Photon System

Classically an electromagnetic field consists of waves with well-defined amplitude and phase. Such is not the case when we treat the field quantum mechanically. There are fluctuations associated with both the amplitude and phase of the field due to Heisenberg uncertainty rules[37]. Let us first start with the basic canonical commutation relations in a system with *N* photons.

$$\begin{gathered}[\hat{a}_k, \hat{a}_l] = \left[\hat{a}_k^\dagger, \hat{a}_l^\dagger\right] = 0, \\ \left[\hat{a}_k, \hat{a}_l^\dagger\right] = \delta_{kl}\end{gathered} \tag{1.1}$$

where $\hat{a}_k$ is annihilation operator and $\hat{a}_k^\dagger$ is creation operator, with $k = 1,2 \dots, N$. They can decrease or increase the number state by single quanta, i.e.

$$\begin{gathered}\hat{a}_k|n_k\rangle = \sqrt{n_k}|n_k - 1\rangle, \\ \hat{a}_k^\dagger|n_k\rangle = \sqrt{n_k + 1}|n_k + 1\rangle\end{gathered} \tag{1.2}$$

where $|n_k\rangle$ is the number state basis which satisfies the orthonormality and completeness such that for k-th mode,

$$\langle m_k|n_k\rangle = \delta_{mn} \;\; m, n \in \mathbb{N}, \\ \sum_0^\infty |n_k\rangle\langle n_k| = 1 \tag{1.3}$$

From these, we also have

$$\hat{a}_k|0_k\rangle = 0, \\ |n_k\rangle = \frac{1}{\sqrt{n!}}\left(\hat{a}_k^\dagger\right)^n|0_k\rangle \tag{1.4}$$

where $|0_k\rangle$ is the vacuum state for the k-th mode.

If we consider the uncoupled harmonic system, the free Hamiltonian of the system is given by

$$H_0 = \sum_{k=1}^{N} \hbar\omega_k\left(\hat{a}_k^\dagger\hat{a}_k + \frac{1}{2}\right) = \sum_{k=1}^{N} \hbar\omega_k\left(n_k + \frac{1}{2}\right) \tag{1.5}$$

Position- and momentum-like operators $\hat{q}$ and $\hat{p}$ for each mode are defined as

$$\hat{q}_k = \frac{\hat{a}_k + \hat{a}_k^\dagger}{\sqrt{2}}, \qquad \hat{p}_k = \frac{\hat{a}_k - \hat{a}_k^\dagger}{i\sqrt{2}} \tag{1.6}$$

Interaction Hamiltonian is very important in a system. It can be linear or bilinear[37] and can be realized experimentally through a parametric process. The most general Hamiltonian is

$$H = \sum_{k=1}^{N} g_k^{(1)}\hat{a}_k^\dagger + \sum_{k=1}^{N} g_{kl}^{(2)}\hat{a}_k^\dagger\hat{a}_l + \sum_{k=1}^{N} g_{kl}^{(3)}\hat{a}_k^\dagger\hat{a}_l^\dagger + h.c. \tag{1.7}$$

This Hamiltonian shows three parts and their Hermitian conjugate. The first part is linear in the field modes, and the corresponding unitary evolution is associated with the displacement operator. The second part describes the linear mixing of the modes and shows the number conservation of the quanta, i.e. creation of one mode will annihilate the other mode. The third part describes the important single and two-mode squeezing. Nevertheless, for our purpose, a single mode description is enough. The time evolution of the density matrix is described in terms of the Heisenberg equation[37-39]

$$\frac{d\rho(t)}{dt} = \frac{i}{\hbar}[\mathcal{H}(t), \rho(t)] \tag{1.8}$$

where $\rho(t) = |\psi, t\rangle\langle\psi, t|$ is defined as the density operator for the system, which has a state vector (in the Schrödinger picture) $|\psi, t\rangle$.

The electromagnetic field in free space is described by the Maxwell equations, and in the quantization process it's described by quantum electrodynamics.

1.1.2 Phonon System

The analogy to the harmonic oscillators will not only apply to travelling electromagnetic waves (photons), but also the quanta of lattice vibrations (phonons), which are also bosons.

Although photons and phonons are both bosons, they do have some differences. Table 1.1 shows a simple comparison for photons and phonons from different aspects[40,41]. Nevertheless, we still borrow well-known tools from quantum optics to deal with the phonon system as analogous to the photon system.

Phonons can also be defined by creation and annihilation operators, where we use $\hat{b}^\dagger$ and $\hat{b}$ to distinguish from photon operators $\hat{a}^\dagger$ and $\hat{a}$. They also satisfy the canonical commutation relations $\left[\hat{b}, \hat{b}^\dagger\right] = 1$.

	Phonon	**Photon**
Type of Boson	Type-II composite (collective excitations)	simple
Propagation media	discrete	continuous
Interactions	highly interactive	Interactive in non-linear media, non-interactive in linear media
Mass	massive	massless
Macroscopic description	Wave equation for elastic continuum	Maxwell equations
Microscopic description	Schrödinger equation	Quantum electrodynamics

Table 1.1: Comparison between phonon and photon (Ref. 41).

1.1.3 Gaussian States

Gaussian states are quantum mechanical states that have Gaussian wave functions. They all can be dealt with Gaussian Wigner functions[37,39]. The states commonly generated in the laboratory are Gaussian[42], and important examples are vacuum, coherent, squeezed and thermal, which are discussed as follows:

1.1.3.1 Coherent States

A coherent state $|\alpha\rangle$ is the eigenstate of the annihilation operator $\hat{a}$ with an eigenvalue α, i.e.,

$$\hat{a}|\alpha\rangle = \alpha|\alpha\rangle, \qquad \alpha \in \mathbb{C} \tag{1.9}$$

In terms of the number states, they can be written as

$$|\alpha\rangle = e^{-|\alpha|^2/2} \sum_{n=0}^{\infty} \frac{\alpha^n}{\sqrt{n!}} |n\rangle \tag{1.10}$$

An alternative definition is given in terms of the displacement operator $\mathfrak{D}(\alpha)$ by applying the displacement field on the vacuum state $|0\rangle$ (a special case of coherent state):

$$|\alpha\rangle = \mathfrak{D}(\alpha)|0\rangle \tag{1.11}$$

where

$$\mathfrak{D}(\alpha) = \exp[\alpha\hat{a}^\dagger - \alpha^*\hat{a}] \tag{1.12}$$

The displacement operator is a unitary operator:

$$\mathfrak{D}^\dagger(\alpha) = \mathfrak{D}(-\alpha) = \mathfrak{D}^{-1}(\alpha) \tag{1.13}$$

A field in a coherent state is a minimum-uncertainty state with equal uncertainties in the two quadrature components. We can also say that the coherent states are the displaced form of the harmonic oscillator ground states.

Here are some properties of coherent states:

The mean number of bosons in $|\alpha\rangle$ is given by

$$\langle \hat{a}^{\dagger}\hat{a} \rangle = |\alpha|^2 \tag{1.14}$$

The coherent state is a minimum uncertainty state so that the variance of quadrature operator is

$$\Delta\hat{x}_{\phi} = \frac{1}{2} \tag{1.15}$$

where ϕ is the phase of the state $|\alpha\rangle$ and $\Delta\hat{x}_{\phi}$ is the same with the vacuum state.

The set of all coherent state is a complete set

$$\sum_{0}^{\infty} |\alpha\rangle\langle\alpha| = 1 \tag{1.16}$$

The orthogonal is not satisfied, i.e. two coherent states are not orthogonal:

$$\langle \alpha|\alpha' \rangle = \exp\left[-\frac{1}{2}|\alpha|^2 - \frac{1}{2}|\alpha'|^2 + \alpha'\alpha^*\right] \tag{1.17}$$

and

$$|\langle \alpha|\alpha' \rangle|^2 = \exp[-|\alpha - \alpha'|^2] \tag{1.18}$$

More details and further discussions about the quantum coherent state can be found in books[37,39].

1.1.3.2 Squeezed States

We can see that the coherent state has some similarities with the classical states, while squeezed states show purely quantum features of the system. They are defined as

$$|\alpha, \xi\rangle = \mathcal{S}(\xi)\mathfrak{D}(\alpha)|0\rangle \tag{1.19}$$

where the $\mathcal{S}(\xi)$ is squeezing operator and is defined as

$$\mathcal{S}(\xi) = exp\left(\frac{1}{2}\xi^*\hat{a}^2 - \frac{1}{2}\xi\hat{a}^{\dagger 2}\right) \tag{1.20}$$

and $\xi = re^{i\theta}$ is known as squeezing parameter and θ is its phase.

The squeezing operator is also a unitary operator

$$\mathcal{S}^{\dagger}(\xi) = \mathcal{S}(-\xi) = \mathcal{S}^{-1}(\xi) \tag{1.21}$$

The variance of quadrature operator is

$$\Delta\hat{x}_{\phi} = \frac{1}{2}[e^{2r}\sin^2(\phi - \theta/2) + e^{-2r}\cos^2(\phi - \theta/2)] \tag{1.22}$$

For example, if $\phi = \theta/2$, then $\Delta\hat{x}_{\theta/2} = \frac{1}{2}e^{-2r}$, and the quadrature fluctuations can be "squeezed" below the vacuum level at the expense of increased fluctuations.

As shown in Fig. 1.1[41]: (a) is a vacuum state, (b) is a coherent state, where they both have the minimum uncertainty and a circular contour in the uncertainty quadrature contour. Moreover, (c) and (d) with the elliptically shaped uncertainty contours are the squeezed states. In this case, the areas are the same, $\frac{1}{2}$.

Squeezed states have attracted great interest since they can be below the vacuum level for certain quadrature and can be used to enhance precision measurements. They are promising for applications to enhance measurement in either phase or amplitude, for example, in measuring gravitational wave. Recently, squeezed states have been used in quantum information processing, relying on the fact that the squeezed state is related to quantum entanglement[43-45].

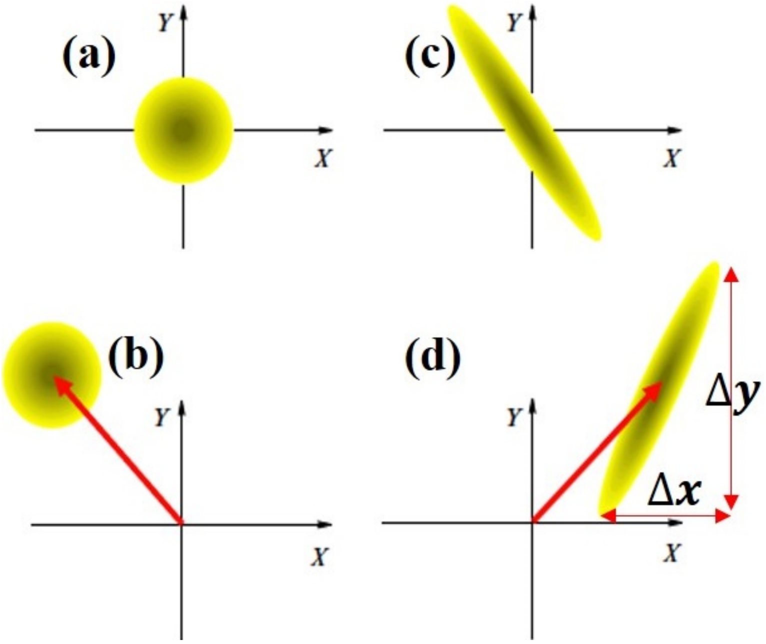

Figure 1.1 Contour in phase space for Coherent state and squeezed state: (a) vacuum state; (b) coherent state; (c) and (d) are squeezed states (Ref. 41).

1.1.3.3 Thermal States

Another important example among the quantum harmonic oscillator states is the thermal states. They are states of the harmonic oscillator which present the thermal boson population. The mean number of thermal bosons is given by [37,39]

$$\langle \hat{a}^\dagger \hat{a} \rangle = \langle \hat{n}_\beta \rangle = \frac{1}{e^{\beta\omega} - 1} \tag{1.23}$$

These states describe harmonics oscillators at thermal equilibrium at temperature T. The inverse temperature β is defined as $\beta = 1/k_B T$, where k_B is Boltzmann constant. The density matrix of such a state is

$$\rho_\beta = \frac{\exp(-\beta\omega\hat{a}^\dagger\hat{a})}{\mathrm{Tr}[\exp(-\beta\omega\hat{a}^\dagger\hat{a})]} \tag{1.24}$$

Where $\mathrm{Tr}[\exp(-\beta\omega\hat{a}^\dagger\hat{a})]$ represents the trace of $\exp(-\beta\omega\hat{a}^\dagger\hat{a})$.

In the Fock basis, let $|n\rangle$ such that $\hat{a}^\dagger\hat{a}|n\rangle = n|n\rangle$, the thermal state then can be written as

$$\rho_\beta = \left(1 - e^{-\beta\omega}\right)\sum_n e^{-\beta n}\,|n\rangle\langle n| \tag{1.25}$$

The thermal state Wigner function is a Gaussian function centered at the origin of the phase space, as the vacuum state, however, the thermal Wigner function is broader than a vacuum state. Moreover, in the case of a vacuum state, the number of bosons in the harmonic oscillator is zero, while the number in thermal state is given in Eq. (1.23). A broader quasi-probability distribution means a large variance and hence, noise in the measurement of $\hat{q}$ and $\hat{p}$. With higher temperature, there is larger noise.

1.1.4 Photon-phonon Quantum Coherent Coupling

Nonlinear optics has had a great impact on modern science and technology. The interactions between optical and mechanical cavities have attracted great interests in multiple applications[1-5]. In this cavity, light is coupled through an optical cavity mode and confined within this resonator where it excites the mechanical modes, which are usually acoustic modes, of the resonator. Strong coupling usually takes place in the highly nonlinear region and the coupling rate between two states should dominate over their own decoherence rate to other channels, normally the local environment. As shown in Fig. 1.2, if the coherent coupling rate Ω_c between the optical and mechanical cavity exceeds both the optical and mechanical decoherence rate κ and γ, where $\gamma = \Gamma_m k_B T/\hbar\Omega_m$ with Γ_m and Ω_m to be dissipation rate and frequency of the mechanical oscillator respectively, then the 'quantum coherent' coupling can happen between the optical and mechanical cavity, i.e. the coherent exchange of energy between the optical field (photon) and the mechanical oscillator (phonon) becomes reversible[46,47 48-51].

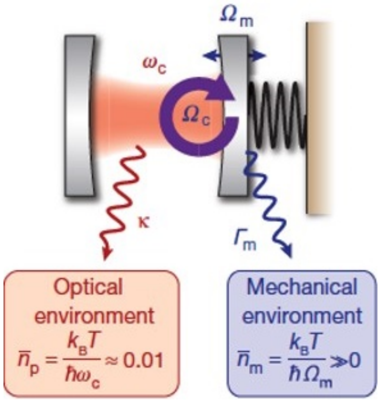

Figure 1.2 A schematic of an optomechanical cavity: an optical cavity with frequency ω_c and mechanical oscillator Ω_m have decoherence rates κ and γ respectively; the quantum coherent coupling rate is Ω_c. (Ref. 45)

Fainstein et al. also reported the strong optical-mechanical coupling in a vertical GaAs/AlAs microcavity for sub-terahertz phonons[52]. It is likely that there is quantum coherent coupling between phonon and phonon as well.

1.1.5 Phonon Squeezed States

Analogous to photon, the phonon state can also be coherent, squeezed, thermal or a combination of them. The phonon squeezed state has attracted a lot of attention since it can achieve lower quantum noise. In addition, squeezed phonons have been considered in various approaches to the ground state of strongly correlated electron-phonon problems[19,53]. It is proposed that it's not necessary to look for reduction of the fluctuation of the lattice amplitude operator below the vacuum level in order to claim the presence of squeezing in phonons; instead we can measure the corresponding fluctuations with doubled frequency modes[19,20,42,54]. The first experiment claiming the detection of the squeezed phonon modes was done by Merlin's group[19]. In this experiment, the squeezed phonon modes were generated in a transparent crystal with an ultrafast pulse of laser and the Hamiltonian of the system is described by

$$\begin{gathered} H = H_0 + H_{int} \\ H_0 = \sum_{1,2} \hbar\omega_j \left(a_i^\dagger a_i + \frac{1}{2}\right) + \sum_j \hbar\omega_j \left(b_j^\dagger b_j + \frac{1}{2}\right) \\ \mathcal{H}_{int} = \hbar \sum_q g_q \left(b_q^\dagger b_{-q}^\dagger + b_q b_{-q}\right) \end{gathered} \tag{1.26}$$

where g_q is the coupling constant. The measurements were performed by standard pump-probe measurement and the phonon states were monitored by measuring the transmission of the probe pulse which is sensitive to the changes in refractive index modulated by the mean square displacement of the atomic positions. Although, this conclusion was criticized by pointing out the experimental techniques used lacked the determination of the reference vacuum state variance[55].

1.1.5.1 Second-order Raman Scattering

Hu et al.[56] proposed a second-order Raman scattering (SORS) process for phonon squeezing through both continuous wave SORS and impulsive SORS where the frequency of the modes satisfies $\omega_q + \omega_{-q} = \omega_1 - \omega_2$. In the impulsive SORS, the energy transfer from photons to two phonons is instantaneous. The Hamiltonian for this SORS process is

$$\begin{gathered} H = H_0 + H_{int} \\ H_0 = \sum_{i=1,2} \hbar\omega_i \left(b_i^\dagger b_i + \frac{1}{2}\right) + \sum_j \hbar\omega_j \left(b_j^\dagger b_j + \frac{1}{2}\right) \\ \mathcal{H}_{int} = \hbar \sum_q \left(\xi a_1^\dagger a_2 b_q^\dagger b_{-q}^\dagger + c.c.\right) \end{gathered} \tag{1.27}$$

There are materials in which the first-order Raman scattering is either weak or prohibited[20], while the second-order Raman can generate phonon squeezed states. The squeezing factor is fully determined by the strength of the photon-phonon coupling constant ξ.

1.1.5.2 Resonant Parametric Down-conversion

A new proposed scheme to generate phonon quadrature squeezing is through a phonon parametric process, e.g. the process of decaying one LO phonon into two LA modes, where LO stands for longitudinal phonon and LA longitudinal acoustic phonon. The three-phonon process has been proposed as the main anharmonic scattering mechanism and also the main phonon decaying mechanism for a long time[57,58]. Yet due to the large population of phonons in the material, it's hard to observe the three-phonon scattering process directly.

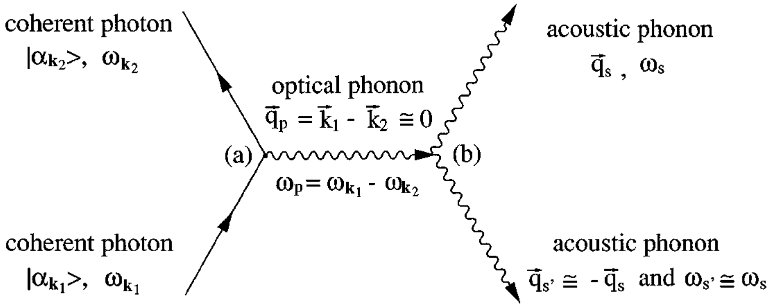

Figure 1.3 A schematic diagram of a three-phonon parametric process. (a) shows the stimulated Raman process creating a coherent optical phonon by a pair of coherent photons; (b) shows a three-phonon anharmonic process. Solid line represents photons and dashed line represents phonons (Ref. 40).

As shown in Fig. 1.3[40], first a coherent optical phonon ω_p which is Raman active and near the Brillouin zone center can be created by the stimulated Raman scattering process where the subscripts k_1 (k_2) refers to the higher (lower) coherent photon from the coherent laser source, secondly the generated pump mode ω_p interacts with two lower acoustic modes ω_s and $\omega_{s'}$ with the same frequency and opposite wavevector through a three-phonon process. This process is also called phonon breakdown[57,58] (see Fig. 1.4). The two lower acoustic modes can be prepared in a squeezed state with an appropriate initial state.

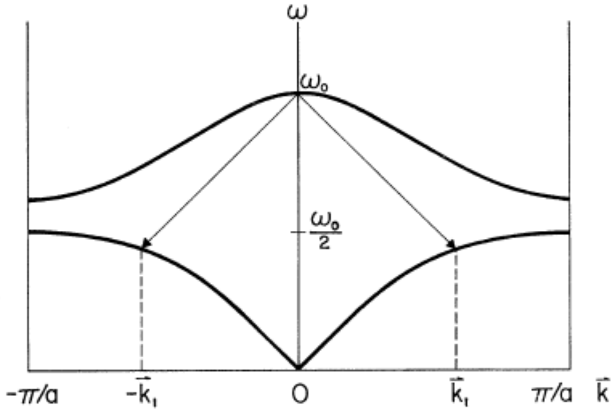

Figure 1.4 A schematic diagram of the decay of a zone center optical phonon with energy $\hbar\omega_0$ decay into two acoustic phonons with half the energy $\hbar\omega_0/2$ and opposite wavevectors $\pm k_1$. (Ref. 57)

Three-phonon interaction is the lowest order perturbation to the harmonic Hamiltonian and the dominant anharmonic process in most materials. Teitelbaum et al. has directly observed anharmonic decay of the photoexcited coherent A_{1g} into target modes by observation of the buildup of the coherent oscillations of the target modes using ultrafast diffuse x-ray scattering[34,59]. They claim this three-phonon scattering process can be understood as a parametric resonance process and prepare the target modes in squeezed state. Moreover, they have extracted the anharmonic coupling constant which is comparable with the first principles calculations[59]. The Hamiltonian for the three-phonon system is described as

$$\begin{gathered} H = H_0 + H_{int} \\ H_0 = \sum_j \hbar\omega_j \left(b_j^\dagger b_j + \frac{1}{2}\right) \\ \mathcal{H}_{int} = \hbar \sum_q g_q \left(b_0 b_q^\dagger b_{-q}^\dagger + b_0^\dagger b_q b_{-q}\right) \end{gathered} \tag{1.28}$$

1.2 COHERENT PHONON GENERATION AND DETECTION

With an ultrashort pulse interacting with condensed matter, the atoms are excited coherently, i.e. all the atoms oscillate with a constant phase relation. This enables us to observe their motions in real-time, instead of just time-averaged mean displacement, which is reflected as temperature. Moreover, the excitation happens at a well-defined time zero, when the pump pulse arrives the sample surface, which enables the investigation of the system relaxation process.

To explain the mechanism of coherent phonon generation, two theoretical concepts have been proposed; impulsive stimulated Raman scattering (ISRS) and displacive excitation of coherent phonons (DECP). The former was first proposed in the 70s and has been successfully applied to explain the coherent phonon generation in transparent crystals and liquids[9-11]. The latter was first proposed in 1992[12] to explain observations in certain opaque materials, such as Bismuth (Bi), Antimony (Sb), Telluride (Te), etc.,[13] that, at first glance, did not match with ISRS[13]. Later on, additional theoretical and experimental results showed that DECP is just a special case of ISRS, and only matters when the imaginary part of the Raman tensor dominates[14-16].

Both theories are based on the same general equation of motion for phonons, describing the time dependent normal mode Q of an atom with mass m as it were driven by a harmonic oscillator.

$$\frac{d^2Q}{dt^2} + 2\gamma\frac{dQ}{dt} + \omega_0^2 Q = \frac{F}{m} \tag{1.29}$$

where ω_0 is the frequency of the phonon, γ the phenomenological damping constant, which is introduced to consider multiple decaying mechanisms of the phonon, and F denotes the driving force due to the electrical field of pump laser pulse. The damping constant γ is related to decaying time τ by $\gamma = 1/\tau$. There are usually phase-destroying mechanism T_2 and population decreasing mechanism T_1 contributions to the decaying time τ in a way that[38,60]

$$\frac{1}{\tau} = \frac{1}{2T_1} + \frac{1}{T_2} \tag{1.30}$$

Interestingly, Laubereau et. al proposed the ISRS can give the following information: dephasing time, collective beating, inhomogeneous broadening and phonon lifetime[61].

The main difference between these two theoretical approaches is in the driving force. For ISBS, the force is a Delta-function term if the pulse width is much shorter than the phonon period, and for DECP, the force is like a Heaviside-function via potential shift in the excited state. Classically, this difference can be illustrated by a pendulum model (see Fig. 1.5): while the impulsive force in ISBS can be analogous to a sudden kick to the pendulum, changing its kinetic energy, the force associated with DECP can be analogous to a quick shift of the suspension point, changing its potential energy[62]. This analogy is valid since we can consider the phonon as classical harmonic oscillator.

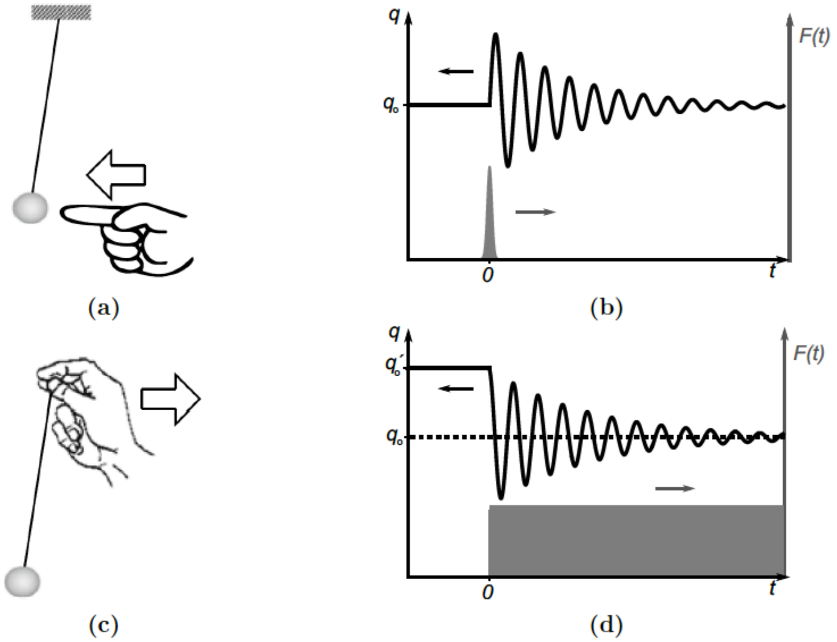

Figure 1.5 Two generation models of coherent phonons. (a) and (b) ISBS; (c) and (d) DECP. (a) and (c) show a classical analogue description of pendulum; (b) and (d) show a time resolved force term (grey area) and displacement (solid line). (Ref. 62)

1.2.1 Impulsive Stimulated Raman Scattering (ISRS)

In the framework of ISRS, phonons are excited by Raman process which is a two-photon process (see Fig. 1.6). When the incident photons are scattered within a medium, most of the scattered photons will have the same frequency as the incident photons ($\omega_s = \omega_i$). This type of elastic scattering is called Rayleigh scattering. Meanwhile, there is also a small amount of inelastic scattering happening where the scattered photons will lose energy or gain energy and have a different frequency other than ω_i. This phenomenon was first observed by C.V. Raman and was thus named Raman scattering. Depending on whether the scattered photons lose or gain energy, they are called Stokes or Anti-stokes Raman scattering respectively.

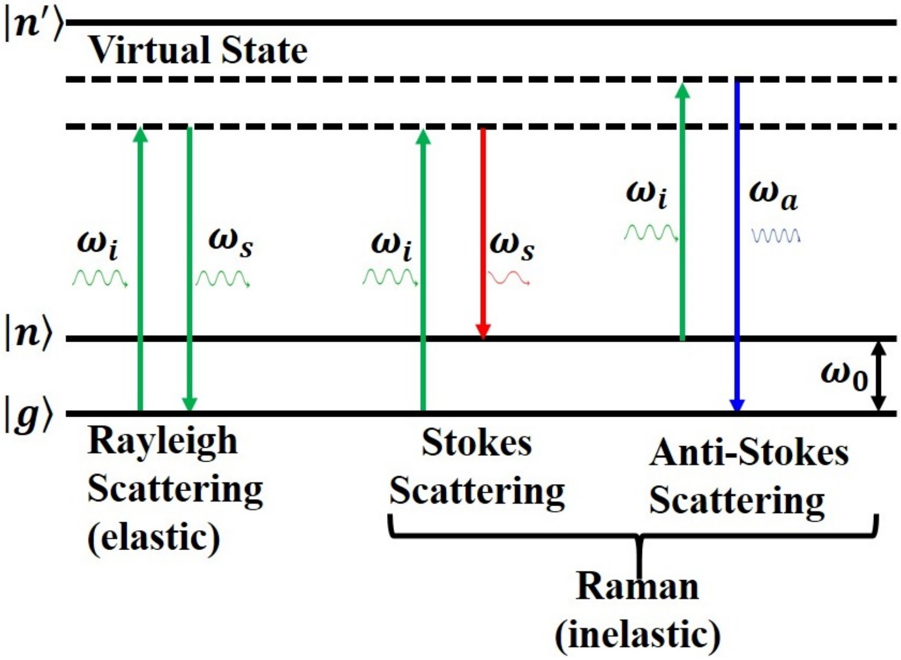

Figure 1.6 Rayleigh scattering (left), Stokes (middle) and anti-stokes (right) Raman scattering.

In the Stoke Raman scattering process, a material in state $|g\rangle$ undergoes a transition to the final state $|n\rangle$ via a virtual state, which is a superposition of many excited states and may not be coincident with a real state, by absorbing a photon with frequency ω_i and emitting a photon with frequency ω_s, meanwhile creating a phonon with frequency ω_0 under the energy conservation law $\hbar\omega_0 = \hbar(\omega_i - \omega_s)$. The scattered photon is called the Stokes line. While in the Anti-Stokes Raman scattering process, the transition from $|n\rangle$ to $|g\rangle$ via a virtual state with absorption of a photon ω_i and emission of a photon ω_a leads to annihilation of a phonon with frequency $\omega_0 = \omega_a - \omega_i$.

Normally, the Anti-Stokes line is much weaker than the Stokes line. There are techniques, such as Coherent Anti-Stokes Raman Scattering (CARS)[63], to enhance the intensity of Anti-Stokes line.

There are two different configurations to generate stimulated Raman scattering. One is to focus an intense laser ω_i on the material. If the material possesses Raman active vibration modes, which means polarizability change can be induced by this vibration[64], and the laser fluence is over the threshold, stimulated Raman scattering can happen and coherent emission of photons with frequency $\omega_i - \omega_0$ and $\omega_i + \omega_0$ can be observed, where ω_0 is the vibration mode frequency. The other configuration is to overlap two laser beams with frequency and wavevector to be (ω_1, k_1) and (ω_2, k_2) which satisfy energy conservation $\hbar\omega_0 = \hbar(\omega_2 - \omega_1)$ and momentum conservation $k_{phonon} = k_2 - k_1$ where ω_0 and k_{phonon} are the frequency and wavevector for the phonon respectively, then stimulated Raman scattering can happen and light with frequency ω_1 will be amplified at the expense of output ω_2 and generate coherent phonon at ω_0 without the requirement of a threshold[65]. For ultrafast lasers, there's a bandwidth $\Delta\omega_i$ associated. As long as $\Delta\omega_i \gg \omega_0$, in a single pulse, there would be a large number of pairs of frequency ω_1 and ω_2 that satisfy $\hbar\omega_0 = \hbar(\omega_2 - \omega_1)$. Regularly, $\Delta\omega_i \sim 1\ eV$ for femtosecond lasers, while the vibration modes in the material are on the order of $1 \sim 10\ meV$.

The two key requirements for ISRS are the existence of Raman active modes in the material, as well as the shorter pulse duration Δt than the phonon period ω_0^{-1}.

Therefore, in the interaction between the ultrashort laser pulse and the matter, ISRS is an essential aspect. In the ISRS generated by ultrashort laser pulse, the incoming higher-frequency photons are coherently scattered into lower-frequency photons, which are still within the laser bandwidth, in the forward direction (forward-scattering) by creating a standing wave ($k_{phonon} = 0$) and can be detected by a time delayed coherent probe pulse.

Raman scattering can be treated classically with a model describing the dynamics of normal coordinate Q by assuming the polarizability α will vary with the inter-atomic distance[64,65]. The second-order polarizability tensor α is expressed as

$$\alpha = \begin{pmatrix} \alpha_{xx} & \alpha_{xy} & \alpha_{xz} \\ \alpha_{yx} & \alpha_{yy} & \alpha_{yz} \\ \alpha_{zx} & \alpha_{zy} & \alpha_{zz} \end{pmatrix} \tag{1.31}$$

and can be expanded in Taylor series with respect to the atomic normal coordinates,

$$\alpha(t) = \alpha_0 + \left(\frac{\partial \alpha}{\partial Q}\right)\bigg|_0 Q(t) + \frac{1}{2}\left(\frac{\partial^2 \alpha}{\partial Q^2}\right)\bigg|_0 Q^2(t) + \cdots \tag{1.32}$$

where α_0 is the polarizability when the inter-atomic distance is fixed at the equilibrium position, Q is the normal coordinate of phonon ω_0 and the subscript "0" on the derivatives indicates expanding at the equilibrium condition. In the harmonic approximation, higher orders can be neglected, and thus

$$\alpha(t) = \alpha_0 + \left(\frac{\partial \alpha}{\partial Q}\right)\bigg|_0 Q(t) \tag{1.33}$$

The polarizability induced by an external optical field $E(z, t)$ (for simplicity, we will only consider linear polarized light propagating in the z direction) is

$$P(z,t) = N\alpha E(z,t) \tag{1.34}$$

where N is the volumetric density of molecules. Thus, the external force is given by

$$F(t) = \frac{1}{2}\left(\frac{\partial \alpha}{\partial Q}\right)\bigg|_0 |E(z,t)|^2 \tag{1.35}$$

Inserting the expression of F into the phenomenological equation of motion Eq. (1.29), we get

$$\frac{d^2Q}{dt^2} + 2\gamma\frac{dQ}{dt} + \omega_0^2 Q = \frac{1}{2M}\left(\frac{\partial \alpha}{\partial Q}\right)\bigg|_0 |E(z,t)|^2 \tag{1.36}$$

where M is the effective mass of the phonon. The elements in the polarizability tensor α are derived from crystal symmetries depending on the selection rules, and zeros mean the modes are not Raman active.

Taking the input pulse as a Delta function[65], the only important term on the left side of Eq. (1.36) is the first term, yielding the oscillating velocity induced by the pump pulse is

$$\frac{dQ}{dt} = \frac{1}{2M}\left(\frac{\partial \alpha}{\partial Q}\right)\bigg|_0 \int dt|E(z,t)|^2 \tag{1.37}$$

Equation (1.37) gives damping-free oscillations. If we introduce the phenomenological damping term, then the solution for the normal coordinate Q can be

$$Q(t) = \left[\frac{1}{2M\omega_0}\left(\frac{\partial \alpha}{\partial Q}\right)\bigg|_0 \int dt|E(z,t)|^2\right] \cdot \sin[(\omega_0^2 - \gamma^2)t]\, e^{-\gamma t} \tag{1.38}$$

We can see the phonon amplitude is proportional to the laser fluence, and if we consider a real pulse function, such as Gaussian pulse, it will also be inversely proportional to the pulse duration, i.e. the shorter the pulse is, the more atoms will displace from the equilibrium position, and thus the larger the phonon amplitude is.

From Eq. (1.38), we can see by ultrashort laser pulse, a coherent vibrational wave in the z direction can be generated and the oscillations are described by a sinusoidal function, which is a signature generated by an impulsive pulse. We can see later it's different in DECP.

1.2.2 Displacive Excitation of Coherent Phonon (DECP)

The DECP was first proposed in 1992 by Zeiger and co-works[12] to explain observations in certain opaque materials, such as Bi, Sb and Te, etc. It was argued that ISRS is not responsible for the coherent generation in those materials because of two main findings: (i) the oscillation $Q(t)$ has a cosine dependence instead of sinusoidal function; (ii) only A_{1g} mode has been observed while the other E_g mode has not been detected, although both of them are Raman active modes[13,66].

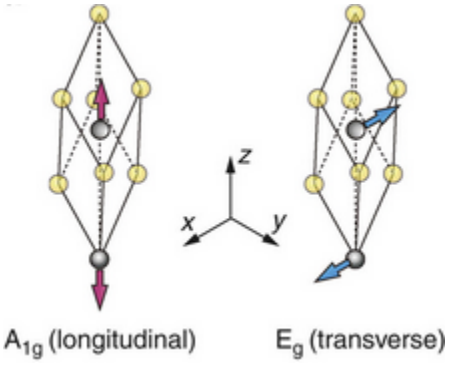

Figure 1.7 Crystalline structure of bismuth and antimony indicating the directions of the A_{1g} and E_g modes (Ref. 66).

Figure 1.7 depicts the two phonon modes in Bi: (left) the fully symmetric A_{1g} mode, which is also referred as the breathing mode, is a longitudinal mode with two atoms along the body diagonal moving oppositely with frequency around 2.93 THz; (right) E_g mode is a degenerated mode in x-y plane, where the two atoms move oppositely along the x-axis or y-axis with frequency around 1.5 THz[66].

In the DECP process, the equilibrium positions of atoms are substantially altered due to the high-density photo excitation of electrons induced by the pump light (see Fig. 1.8). The electronically excited system then relaxes to a quasi-equilibrium state in a shorter time scale than it takes for lattice/nuclei return to equilibrium. If the material has A_{1g} mode, the nuclei will displace to the quasi-equilibrium coordinate and vibrate coherently around it. DECP requires a significant absorption of the pump to disturb the electronic system while ISRS doesn't, and thus phonon amplitude at time zero in DECP is proportional to the maximum excited electron density.

Later on, it was challenged by Garrett and Merlin[15] since the E_g mode was observed in Sb. They claimed DECP is just a special case of ISRS. With a more careful theoretical study[14], Stevens and Merlin demonstrated that there were two separate tensors responsible for the stimulated Raman scattering, one accounting for the phonon-induced modulation of the susceptibility and the other for the dependence of the coherent phonon amplitude on the light intensity. They have the same real part which is associated with the impulsive generation of phonons, but a different imaginary part[14]. DECP is inherent to metals, semi-metals and narrow bandgap semiconductors and related to inter-atomic displacement under strong ionization[42].

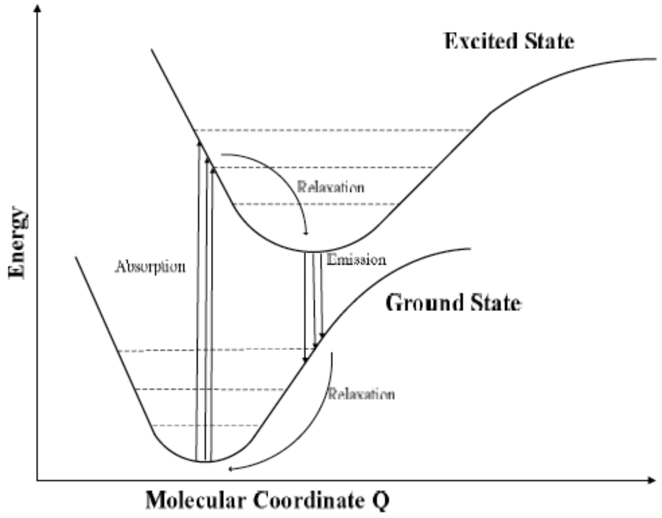

Figure 1.8 Illustration of DECP process: excitation and relaxation of the electrons from an equilibrium coordinate to a quasi-equilibrium coordinate leads to the kick-start of the lattice vibrations. The dashed lines are the bounded vibrational states (Ref. 107).

In summary, in order to describe the mechanism of coherent phonon generation, ISBS theory and DECP theory have been proposed. Actually ISBS and DECP are just two forms of stimulated scattering by phonons[14]. Both theories are described by two different tensors that have identical real part but different imaginary part[14]. Therefore, in the transparent region, ISRS and DECP are identical mechanisms, while in the absorption region, i.e. opaque materials, where the imaginary part dominates, the mechanism of coherent phonon generation is displacive.

1.2.3 Acoustic Phonon Propagation in Superlattice Structure

The importance of phonons and their interactions in the bulk materials have been extensively studied. With fast development of the nanotechnology, quantum effects need to be considered when studying phonon transport in nanostructures. Since dimensional confinement restricts the phase space of the phonons, it will certainly affect carrier-phonon interactions in the nanostructures. Semiconductor superlattice structures have been widely used and studied, like semiconductor lasers[67], terahertz sources[68,69], thermal electric devices[70] and recently, people are trying to make "phonon lasers", called SASER[71].

A superlattice structure is a periodic structure of layers of two or more materials. Figure 1.9 (a) depicts a finite SL system with acoustic phonons propagating through the SL perpendicular to the interfaces. The system consists of *N* periods of alternating layers of material *A* with thickness d_A and material *B* with thickness d_B, so the period thickness is $D = d_A + d_B$. In the elastic continuum model, the phonon dispersion relation is given by[72-75]

$$\cos(qD) = \cos\left(\frac{\omega d_A}{v_A}\right)\cos\left(\frac{\omega d_B}{v_B}\right) - \frac{1+\delta^2}{\delta}\sin\left(\frac{\omega d_A}{v_A}\right)\sin\left(\frac{\omega d_B}{v_B}\right) \tag{1.39}$$

where $\delta = \rho_A v_A / \rho_B v_B$, ρ_A and ρ_B are the corresponding mass density and v_A and v_B are the sound velocities for phonons along [001] for both media. A plot of Eq. (1.39) is shown in Fig. 1.9 (b) for a typical superlattice structure (green line). The black curve is the dispersion relation of acoustic phonons in effective bulk material considering the average of two materials composing this superlattice. This modulation of the acoustic phonon gives rise to two significant features in superlattices: (i) the acoustic phonon dispersion curve will fold into the first Brillouin zone of the superlattice between $-\pi/D$ and π/D (also call mini-Brillouin zone); (ii) frequency gaps will be created at the center and edge of the mini-Brillouin zone due to perturbation (see Appendix A). As is the same with the Kronig-Penny model for electrons[76], two degenerate modes exist in the unperturbed dispersion relation at wavevector $\pm n\pi/D$, where n is an integer. With modulation of the acoustic phonons, the degeneracy will be remove by creating a gap with the second term in Eq. (1.39) with the factor δ.

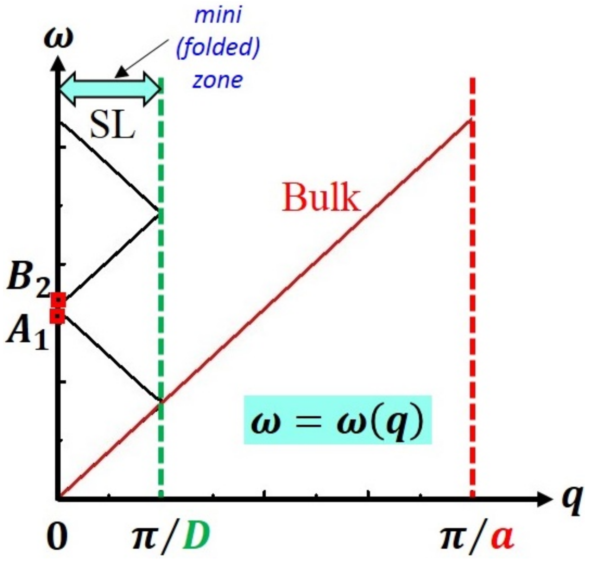

Figure 1.9 Phonon dispersion: Black curve is phonon dispersion for SL and red line is acoustic phonon dispersion in effective bulk material considering the average of two materials composing this superlattice where a is the lattice constant, D is the period thickness.

At the zone center and edge, the two eigenmodes are standing waves and can be labeled by their symmetry, one being odd (A_1) and the other even (B_2) with respect to inversion about the middle of each layer (see Fig. 1.8). The A_1 (lower) mode is Raman active, however the B_2 (upper) mode is forbidden[60].

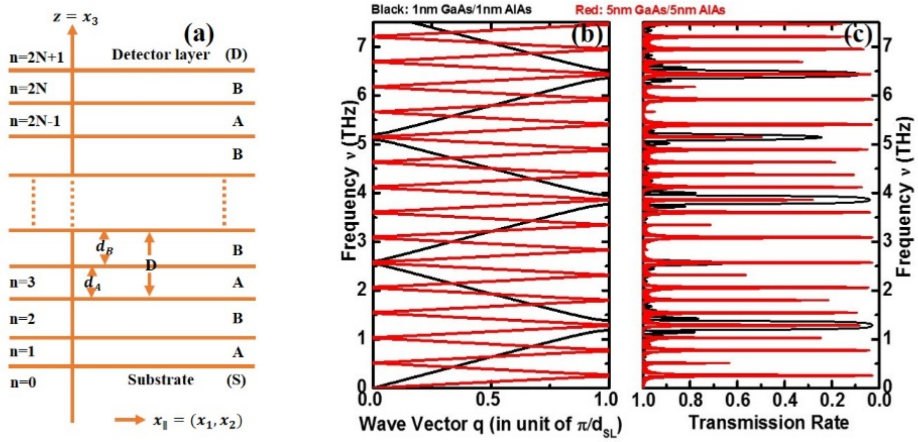

Figure 1.10 (a) Schematic finite SL system with alternative layers of A and B. The thickness for each layer is d_A and d_B respectively, so the period thickness is $D = d_A + d_B$. The layer interfaces lay in the $x = (x_1, x_2)$ plane, perpendicular to the z axis (x_3 axis). The phonons originate in the substrate S, propagate through N periods and are observed in the detector layer D; (b) Acoustic phonon dispersion curves in two SL structures with different periodicity calculated from Eq. (1.39). SL with a larger period introduces more phonon folding and stop bands. (c) Transmission rate for the SLs in (b) at normal incidence with 30 periods, dips occur at the Bragg reflection condition.

Fig. 1.10 (b) shows longitudinal acoustic (LA) phonon dispersion in two GaAs/AlAs SL structures with different periodicity calculated with the elastic continuum model. SL with a larger period (5/5, red) introduces more phonon folding and stop bands than that with the smaller period (1/1, black). As shown in Fig. 1.10 (c), the transmission rate can be calculated from the transfer matrix[72,75] and the transmission dips occur for frequencies that satisfy the Bragg reflection condition.

1.2.4 Generation and Detection of Coherent Acoustic Phonons

Generation and detection of high-frequency coherent acoustic phonons have been persistently pursued for decades by researchers in the ultrasonic field and the mechanisms for generation and detection processes have been studied[26,31]. Because of the long wavelength of light, optical probes can only couple to the excitations near the zone center of the crystal Brillouin zone. Recently several groups have detected terahertz coherent acoustic phonons with coherent phonon spectroscopy[77,78]. Coherent acoustic phonons can be generated with femtosecond laser pulses via launching a strain wave near sample surface, which is a group of coherent phonons traveling with the same velocity. When a probe photon is scattered by a phonon, the maximum phonon vector that can be detected is $k_{phonon} = 2k_{probe}$ (backscattering of probe photon, $2k = 4\pi n/\lambda$, where n is the refractive index for the wavelength λ), in order to satisfy momentum conservation. This process is called Stimulated Brillouin Light Scattering (SBLS). If the probe laser has a short penetration depth, it will only detect the acoustic wave packet after it is reflected at the interface and travels back to the sample surface. The temporal expansion of the acoustic echo (Δt) corresponds to coherence time, which is related to phonon coherence length, $l_c = v \cdot \Delta t$. The difference of time delays when the acoustic wave packet is detected the first time (τ_1) and second time (τ_2) is the round-trip time that the coherent phonon travels in the sample. Phonon group velocity can be derived as: $v = \frac{2 \cdot L}{\tau_2 - \tau_1}$. Eventually the acoustic wave packet will disappear when all phonons are scattered. This time constant of phonon amplitude decay is called the coherent phonon lifetime, which is related to phonon mean-free-path, $\Lambda = v \cdot \tau$. In bulk materials, phonons with $k_{phonon} = 2k_{probe}$ usually have very low frequency and hence are not thermally important. Fig. 1.9 (b) shows acoustic phonon dispersion in two SL structures with different periods calculated with an elastic continuum model[72,74]. In SL, due to phonon folding, many high frequency phonons also fall into $0 \sim 2k_{probe}$ region and hence more coherent phonons can be generated and detected. Broadband coherent optical phonons up to 2.5 *THz* have been detected in the InGaN/GaN SL with coherent phonon spectroscopy[78].

1.3 COHERENT HEAT TRANSPORT

Phonons are quantized lattice vibrations, characterized with frequency ω, wave vector k, phonon velocity v and lifetime τ. Phonons are major heat carriers in most crystalline solids. Lattice thermal conductivity is a macroscopic parameter summing over all phonon modes in the material $k_L = \sum_{\alpha} C_{\alpha} v_{\alpha}^{2} \tau_{\alpha}$ where C is specific heat and α represents individual phonon mode[79]. Not all phonons contribute to the heat transport process equally.

For example, in bulk Bi_2Te_3, phonons with wavelength ($\lambda = 2\pi v/\omega$) from 2 *nm* to 6 *nm* contribute to 60% of the total lattice thermal conductivity[80]. Phonons that are thermally important are called ‘thermal phonons’. Thermal phonons usually mean acoustic phonons. Optical phonons, even though they are thought to be insignificant in most materials to thermal transport because of their small group velocity, can still play a role by scattering acoustic phonons[81,82]. Similar to other fundamental particles (photons, electrons), phonons possess both wave-like and particle-like characters. When considering phonons as lattice waves, they can be called “coherent phonons” if atomic movements induced by the lattice wave are ‘correlated’. The distance that coherent phonons can travel before losing their “coherence” is called phonon coherence length[83] l_c. When considering phonons as particles, phonons can be scattered by other particles (electrons, phonons and defects) or boundaries/ interfaces. The average distance phonons can travel before being scattered is phonon mean free path $\Lambda = v \cdot \tau$. Since lattice wave cannot extend further after the phonon getting scattered, usually l_c is shorter than Λ. In bulk materials, where the sample thickness L_{bulk} is much longer than phonon coherence length l_c and phonon mean free path Λ, phonons are treated as “incoherent” and travel diffusively, which means atomic movements are random and phonons lose track of their original directions because of numerous scattering events. In nanostructures, if the characteristic length L_{nano} is comparable to or less than phonon mean free path Λ,. Phonons can travel through the material without any scattering, which is called ‘Ballistic Heat Transfer’. If the characteristic length further reduces to be less than phonon coherence length l_c, the wave features of phonons should be considered. In this regime, coherent heat transport needs to be considered[84]. However, this has been debated for a long time since if there is coherent heat transport, then people should observe a decreased thermal conductivity with increasing temperature due to the dominant Umklapp scattering. If the total thickness of the sample is thinner than the mean free path for some thermal phonons, it is difficult to distinguish between Bragg reflection of simply high interface phonon transmission and coherent thermal transport. The measured thermal conductivity would not be the intrinsic thermal conductivity of the SL structure, instead, it is similar to Si thin film thermal conductivity[85], which is dominated by the surface scattering, instead of the intrinsic thermal conductivity of bulk Si that is determined by the phonon dispersion. To really understand the effect of coherence on the SL thermal conductivity, one would need to observe the 'bulk' thermal conductivity of SL and verify that it decreases with increasing temperature due to intrinsic Umklapp scattering. Increasing thermal conductivity with increasing temperature always suggests that extrinsic scattering (defects and surfaces) is dominate. For a perfect infinitely large crystal, the thermal conductivity is supposed to increase with decreasing temperature to approach infinity at the low T limit[86]. Bivas et al.,[87] has reported the decreasing thermal conductivity with the increasing temperature in the TiN/AlScN superlattice with total thickness of around 240 *nm*, however, the temperature dependence is still not that strong, indicating that both extrinsic and intrinsic umklapp processes play some roles.

In the Chapter 4.3, Raman scattering and pump-probe experiments have been carried out on the GaAs/AlAs superlattice structures. In the GaAs/AlAs superlattice structure, we can see the decay constant from spontaneous Raman scattering (~4 *ps*, incoherent phonons) is smaller than that of the pump-probe experiment (~25 *ps*, coherent phonons). This is a very interesting phenomenon since in other materials, like diamond and polycrystalline Bi[88,89], the decay rate shows the same behavior for the coherent and incoherent phonons where a coherent anti-stokes Raman scattering (CARS) technique was used to measure the decay rate for coherent phonons, and therefore they concluded that the anharmonic decay is the main source of decoherence. However, in our measurement, the decay time for incoherent phonon is smaller than that of the coherent phonon which could be because of the insufficient resolution for the Low cut-off Raman scattering, or because in the superlattice structures, anharmonic scattering is greatly reduced for coherent phonons due to the selective scatterings paths, and thus the decay constant is larger. The coherent phonons may have the potential to suppress anharmonic scattering and increase the phonon coherence time, therefore, it's promising to introduce coherent phonons to tailor the thermal conductivity of the SL structures.

1.3.1 Boltzmann Tranport Equation

The Boltzmann Transport Equation (BTE) has been extensively used to study nanoscale heat transfer when phase coherence is not important[79] and phonons can be purely treated as particles. However, the phase information is not important when the thermal phonon coherence length can be neglected.

In an equilibrium system, the phonon distribution follows the Bose-Einstein distribution

$$f_0 = \frac{1}{\exp\left(\frac{\hbar\omega}{k_B T}\right) - 1} \tag{1.40}$$

Generally, the BTE is described as[90]

$$\frac{\partial f}{\partial t} + \vec{v}_g \cdot \nabla f + \vec{a}\frac{\partial f}{\partial \vec{v}} = \left(\frac{\partial f}{\partial t}\right)_{collision} \tag{1.41}$$

where $\vec{v}_g$ and $\vec{a}$ are the particle velocity and acceleration rate respectively. The term on the right-hand side stands for the scattering process, which can alter the phonon distribution function. There are two types of scattering processes: inelastic processes (including the Normal process, Umklapp process and scatterings on other carriers, etc.) and elastic processes (including scatterings on grain boundaries, impurities, etc.). With a single mode relaxation time approximation, which assumes there is an effective relaxation time τ_{eff} for all the phonon modes, the collision term can be written as

$$\left(\frac{\partial f}{\partial t}\right)_{collision} = \frac{f - f_0}{\tau_{eff}} \tag{1.42}$$

where τ_{eff} is a combination of relaxation time for the dominant scattering processes

$$\frac{1}{\tau_{eff}} = \frac{1}{\tau_N} + \frac{1}{\tau_U} + \frac{1}{\tau_i} + \cdots \tag{1.43}$$

Under the relaxation time approximation, the system restores its equilibrium distribution through an exponentially decaying process over a time scale τ_{eff}. However, the phonon dispersion and scattering mechanisms have to be known in advance to perform the BTE calculation.

1.3.2 Coherent Thermal Transport in Superlattices

Ballistic phonon transport has been studied extensively over the decades[91-93]. However, the importance of coherent phonons to the overall thermal transport has only recently been addressed by two recent experimental studies: a) Luckyanova et al.[94] reported that thermal conductivity of GaAs/AlAs SLs increases almost linearly with the total sample length L_{SL} over a wide temperature range, 30~297 K, which was explained with coherent thermal phonon transport. The phonons are called "coherent" in their study because the sample length is shorter than the phonon mean free path ($L_{SL} < \Lambda$). Even though similar phenomena have been observed in molecular dynamic simulations[95,96], the role of CTP was not mentioned in these studies. B) J. Ravichandran et al.[97] demonstrated a transition region from incoherent heat conduction to coherent phonon conduction by measuring a minimum thermal conductivity around certain period thickness d_{SL} in the $SrTiO_3$/$BaTiO_3$ SL, which was attributed to competition between interface scattering and phonon-folding in the transition region. In fact, the minimum thermal conductivity has been observed in many other experiments[87,95-100]. Later, several groups conducted molecular dynamics and interfering Monte Carlo studies to further understand the CTP transport observed in experiments, respectively[80,101-103]. Very recently, Latour et al. introduced a criterion to distinguish coherent vs. incoherent heat conduction, trying to reconcile the disagreements observed in experiments by bringing in the concept of temporal and spatial coherence[104,105]. Even though this picture provides some guidance for understanding coherent phonon conduction, it fails to interpret some experimental results. For example, in the GaAs/AlAs SL, l_c is estimated to be 1~2 nm[97], and Λ_{bulk} is about 1 μm. Based on Latour's picture, with $d_{SL} = 12\,nm > l_c$, thermal conductivity κ should be independent of sample length L. But Luckyanova's experimental results showed that κ has a strong dependence on sample length L. The second problem is that Latour defines phonons as "coherent" only when phonon coherence length l_c is greater than the SL period thickness d_{SL}. In Luckynova's experiment, phonons are called "coherent" because the phonon mean path Λ is greater than the sample length L. Recently this year, Hopkins' group[106] claims even in Luckyanova's experiment, incoherent phonon transport should dominate. To provide an unambiguous picture of coherent phonon transport in SLs, direct measurement of coherent phonons is necessary.

Chapter 2: Pump-probe Spectroscopy

In a standard time-resolved pump-probe experiment, one can measure the reflectivity change or transmittance change depending on whether the material is an opaque or transparent material with a delay time between pump and probe pulse. An optical delay stage is put in the probe beam optical path to control the delay time between pump and probe beams.

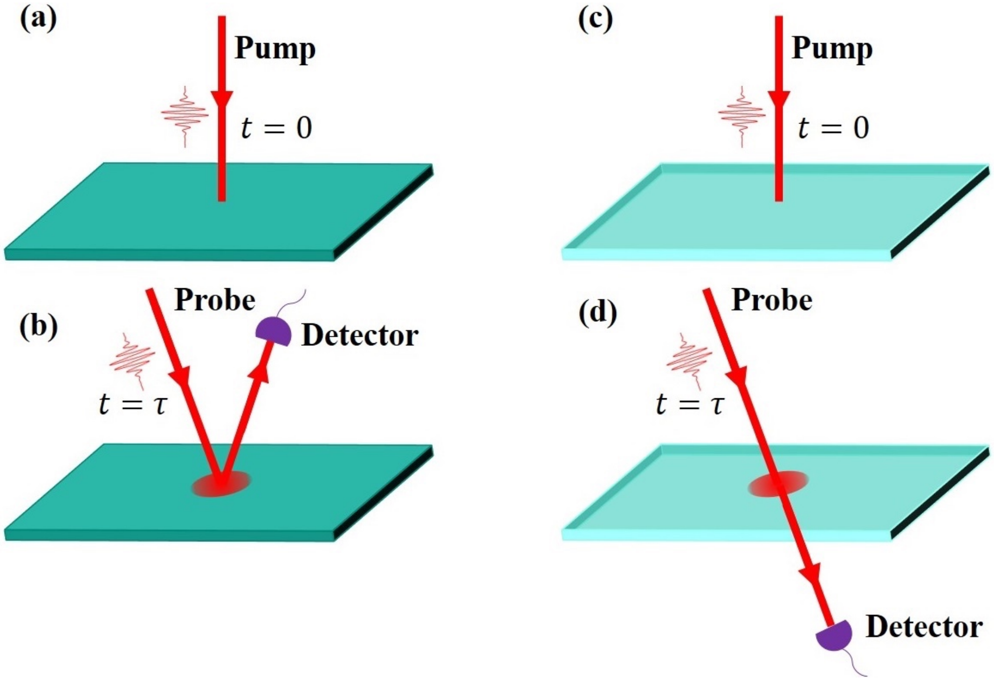

Figure 2.1 Illustration of pump probe dynamics: the pump pulse first excites the material at time zero, and the probe pulse detects the reflection/transmission change at time delay τ depending on whether the material is opaque (a) and (b), or transparent (c) and (d).

The basic idea of the pump probe experiment is described in Fig. 2.1. The system under study is first pumped with a short laser pulse to generate excited carriers; these carriers will modulate the dielectric function, and thus the refractive index of the material. Then this change will be probed by a second, less intense laser pulse by measuring the reflection/transmission change at time delay τ depending on whether the material is opaque or transparent as long as the lifetime of the excitations is longer than the pulse duration.

The development of the lasers makes it possible to apply the pump-probe technique to study lattice vibrations in the femtosecond scale. More importantly, with ultrafast laser pulse, the solids will sustain lattice vibrations with a high degree of temporal and spatial coherence which are called coherent phonons.

In this chapter, the characterization of our experimental systems will first be discussed and then two set-ups with specific experimental steps will be presented.

2.1 ULTRAFAST LASER SYSTEM

Our system consists of a titanium-doped (Ti-) sapphire oscillator (Tsunami, Spectra-Physics) and a regenerative amplifier (Spitfire ACE, Spectra-Physics).

The oscillator is pumped by a 5 *W* CW green DPSS laser at 532 *nm* (Millennia, Spectra-Physics) and the output laser pulses with a 35 *fs* pulse width (FWHM), 60 *nm* bandwidth, 80 *MHz* repetition rate and 900 *mW* average power at 800 *nm*. The spectrum of the laser pulse is showed as follows (see Fig. 2.2), measured by the Ocean-Optics spectrometer. The pulse width can be estimated if the Gaussian pulse is assumed, given by the uncertainty relation:

$$
\begin{gathered}
c = \lambda \cdot \nu \\
\Delta c = \Delta\lambda \cdot \nu + \lambda \Delta\nu = 0 \\
\Delta\nu = -\Delta\lambda \cdot \frac{\nu}{\lambda} = -\Delta\lambda \frac{c}{\lambda^2} \\
\Delta\nu \cdot \Delta t \geq 0.441 \\
\Delta t \geq \frac{0.441}{\Delta\nu} = \frac{0.441\lambda^2}{\Delta\lambda \cdot c}
\end{gathered}
\tag{2.1}
$$

where c is the speed of light, λ is the wavelength and ν is the frequency. The estimated pulse width for a 57 *nm* bandwidth (see Fig. 2.2) is about 16 *fs*.

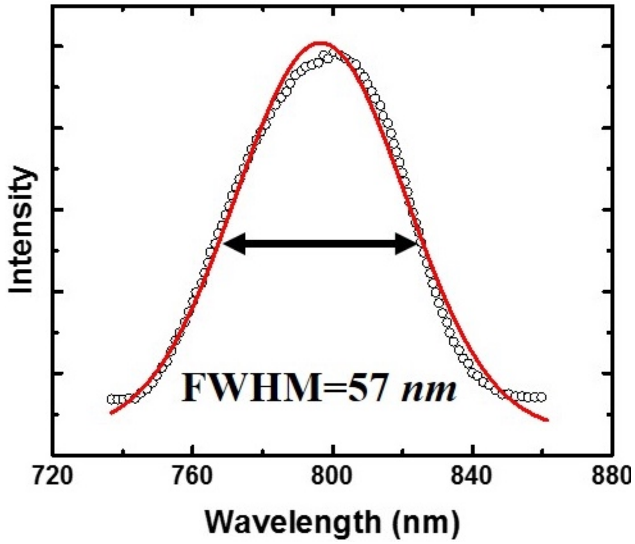

Figure 2.2 Spectrum of pulses from Tsunami measured by the Ocean-Optics spectrometer. With a Gaussian Fit, we can get that the FWHM is 57.2 *nm* with a variance of 0.3*nm*.

The amplifier is driven by a Q-switch Nd:YLF solid state laser (Spectra-Physics). The output laser pulse is at 800 *nm*, with a 35 *fs* pulse width (FWHM) and 5 *kHz* repetition rate. The average power is 6 *W*.

2.2 ULTRAFAST LASER PULSE CHARACTERIZATION

The ultrafast laser pulse is usually very short, on the scale of picoseconds or femtosecond, even attoseconds nowadays. The optical response of a photo-detector is not fast enough to resolve these pulses. In order to characterize the duration of the ultrafast lasers, different techniques have been developed, including auto-correlation, cross-correlation and the frequency-resolved optical gating (FROG) method[107,108].

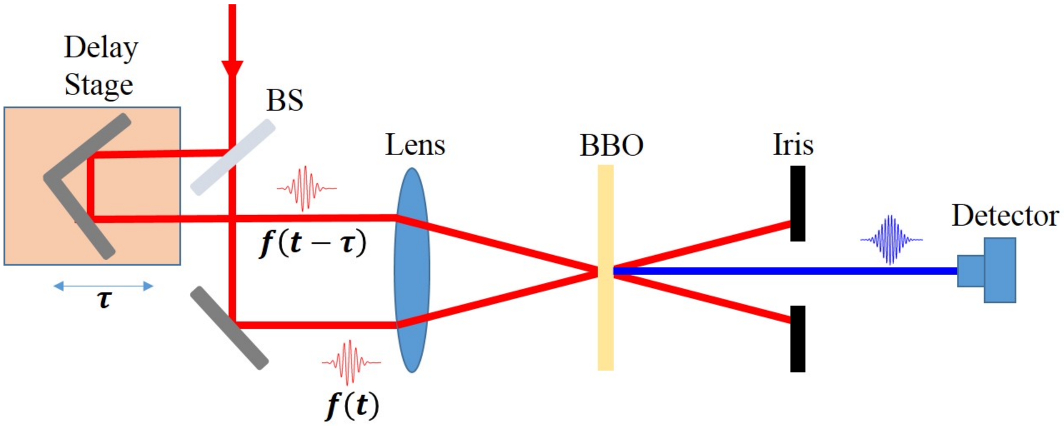

Figure 2.3 Intensity auto-correlator configuration: with the right angle (phase-matching condition) of the BBO (Beta-barium borate, nonlinear crystal) crystal, the intensity of the SHG signal is measured by the detector as a function of relative time delay where BS stands for beam splitter.

Auto-correlation is based on the idea that an ultrafast pulse can sample and check the temporal correlation trace with itself. In an Intensity auto-correlator (see Fig. 2.3), one pulse coming in is split into two identical (ideally) pulses by beam splitter (BS) with optical path differences, and thus the relative delay time of the two pulses is controlled mechanically by the delay stage. They are then focused and spatially overlapped on a χ^2

nonlinear crystal where sum-frequency generation processes[64], in this special case, second harmonic generation (SHG) can happen. With a proper angle (phase-matching condition[64]) and a small difference in the optical paths, the detector can record the power of the SHG as a function of time delay. The dependence of the autocorrelation signal on the temporal delay is given by

$$I_{SHG}(t) = I_\omega(t) \cdot I_\omega(t-\tau) \tag{2.2}$$

where $I_\omega(t) = f(t)f^*(t)$ and $f(t)$ is the electric field of the pulse and $f^*(t)$ is its complex conjugate. It's obvious that if the relative time delay is increased, and therefore the overlap of the two pulses in the nonlinear crystal is reduced, the mixing product becomes weaker. Since the photo-detector can only capture the time averaged intensity signal, the measured signal is therefore[107],

$$\langle I_{SHG}(t)\rangle = 1 + 2G_2(\tau) \tag{2.3}$$

where $G_2(\tau)$ is the second-order auto-correlation function given by

$$G_2(\tau) = \frac{\int_{-\infty}^{\infty} I(t)I(t-\tau)}{\int_{-\infty}^{\infty} I(t)I(t)} \tag{2.4}$$

The constant background term '1' in Eq. (2.3) can be eliminated by the nonlinear experimental setup (see Fig. 2.3), and thus the measured signal $\langle I_{SHG}(t)\rangle$ is proportional to $G_2(\tau)$. There is a conversion factor between the actual pulse width $\Delta\tau$ and the FWHM (full width at half-maximum) $\Delta\tau_G$ of the correlation function $G_2(\tau)$ depending on the pulse shape. For the commonly used Gaussian shape pulse, $\Delta\tau = \Delta\tau_G/\sqrt{2}$. The auto-correlation result (see Fig. 2.4) for the 800nm Gaussian pulse at the sample position shows the measured pulse width is 222 *fs*.

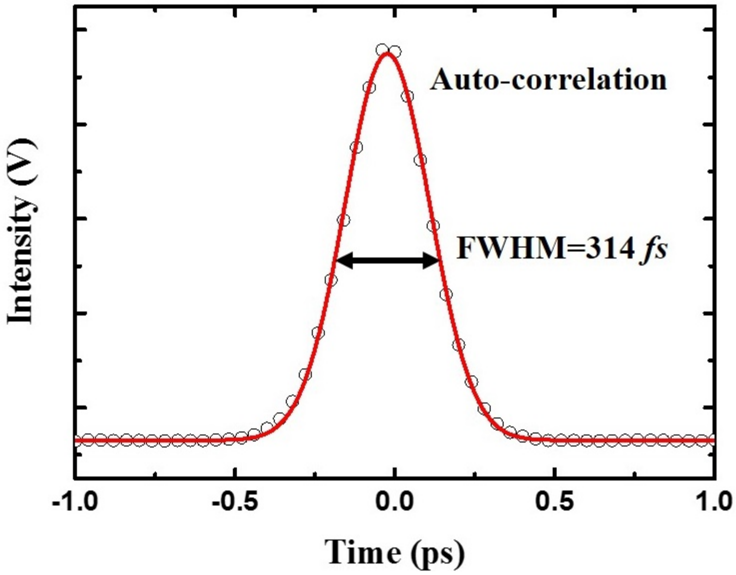

Figure 2.4 Auto-correlation result for 800 *nm* Gaussian pulse at the sample position.

Cross-correlation is a way to deal with the correlation between two different pulses by using a χ^2 nonlinear crystal where sum-frequency generation processes can happen. Apparently, we need to know one of the pulses to extract information for the other one. One thing we must know is for both auto-correlation and cross-correlation techniques, they are independent of the symmetry of the actual pulse, i.e. we can always get a symmetric signal with respect to its center even for asymmetric pulses, and thus, we cannot recover the original pulse intensity profile. Moreover, they are also not sensitive to the phase of the laser field, which disables them from characterizing chirped pulses or phase-modulated pulses. However, the phase information can be very important for the narrower pulses ($< 50\ fs$), leading to the development of FROG technique.

FROG is a technique for ‘complete’ characterization of ultrashort pulses, measuring not only the energy and duration of the pulses, but also the full spectrum and the frequency dependent phase information from the FROG algorithm. This technique has been pioneered by Rick Trebino’s group at Georgia Institute of Technology[108]. A typical set up for a FROG is similar to that of an Intensity auto-correlator (see Fig 2.3) except the photo-detector is replaced with a spectrometer.

2.3 EXPERIMENTAL SETUP

We’ve basically used two experimental systems to capture different ultrafast coherent phonon dynamics, one with coherent phonon spectroscopy (CPS) with the oscillator and the other one with the amplifier. These two systems have they own advantages and disadvantages.

The CPS system with the oscillator has a very high sensitivity up to 10^{-6}, so it can be used to capture small signals with long time averaging, which makes it to be capable to measure high frequency coherent phonons in superlattice structures. With a mode-locked Ti: Sapphire femtosecond laser (Tsunami, Spectra Physics), one-color pump-probe experiment is performed in non-collinear reflection geometry at room temperature. Both pump and probe pulses have an 800 *nm* central wavelength, 258 *fs* pulse width and 76 *MHz* repetition rate. Pump and probe beams are focused onto the sample surface by a 10x objective lens, with spot sizes (diameter) of 13.38 μm and 6.69 μm respectively. An optical delay stage is put in the probe beam optical path to control the delay time between the pump and the probe beams. The differential reflectivity $\Delta R/R$ is recorded by a Si detector (DET100, Thorlabs). A lock-in amplifier (model 7265, Singal recovery) with a chopper working at 2.7 kHz is used to acquire the data. We use the LabVIEW program to record the data from lock-in amplifier. More averages are needed for detecting high frequency coherent phonons.

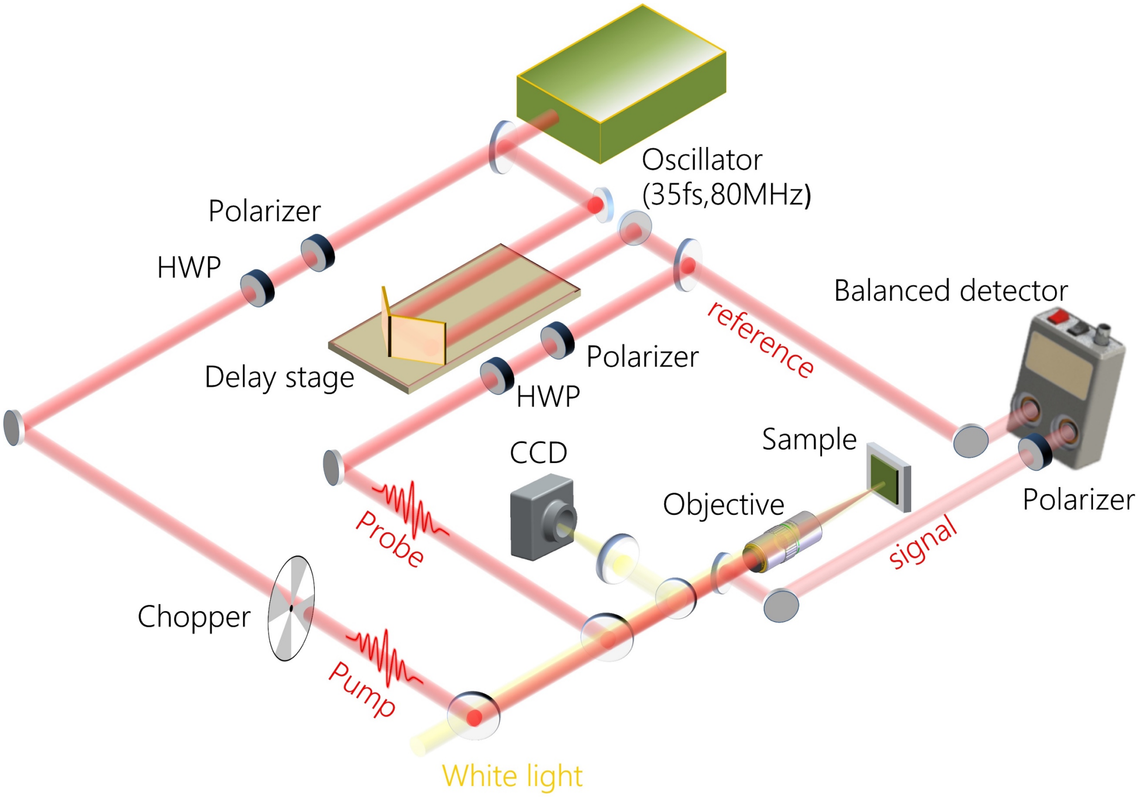

Figure 2.5 CPS system with oscillator: In the one-color pump-probe experiment, we use the polarizer to make the pump and the probe light perpendicular and use another polarizer in front of the detector to filter out the pump signal.

Meanwhile, since the amplifier system has a pulse energy up to 1 mJ, it can excite the carriers efficiently so there is no need to average too many passes with sensitivity up to 10^{-4}. This unique advantage makes it perfect for some crystals with a very strong coherent phonon signal, like CdSe and Bi. Using a mode-locked Ti: Sapphire femtosecond laser (Amplifier, Spectra Physics), the two-color pump-probe experiment is performed in collinear reflection geometry at room temperature. A second harmonic generation crystal (Beta-barium borate, BBO) is used to double the photon energy to 3.1*eV*, after which a band-pass filter is used to block the residue laser beam at 1.55 *eV*. Pump and probe pulse have a 400 *nm* and 800 *nm* central wavelength respectively, with a 100 *fs* pulse width and 5 *kHz* repetition rate. A 15 *cm* lens is used to focus two beams on the sample surface, with spot sizes of 245 μm and 60 μm respectively. An optical delay stage is put in the probe beam optical path to control the delay time between the pump and probe beams. The difference between the reflected and reference probe beams is measured by a balance detector (model 2307, Newport). A lock-in amplifier (model 7265, Singal recovery) with a chopper working at 585 *Hz* is used to acquire the data. In coorperation with the LabView program, we can record the data from lock-in amplifier.

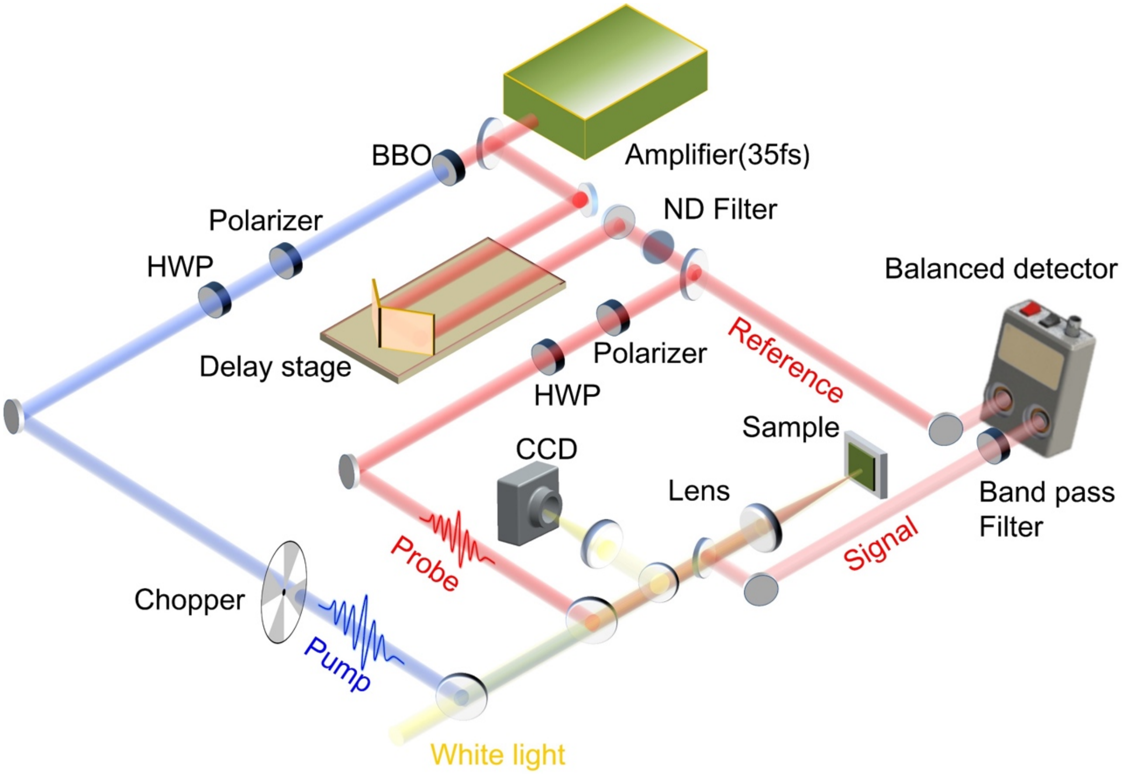

Figure 2.6 CPS system with amplifier: The combination of the half wave plate (HWP) and polarizer can attenuate the laser power. The neutral density (ND) filter in the probe path we used is 10^4; the 800 *nm* band pass filter can filter out the 400 *nm* pump pulse; we also use a white light source and CCD camera to obtain the sample image.

Chapter 3: Ultrafast Dynamics Studied with Pump-probe Measurement

In the standard time-resolved pump-probe experiment, one can measure the reflectivity change or transmittance change depending on whether it's an opaque or transparent material with a delay time between pump and probe pulse. An optical delay stage is put in the probe beam optical path to control the delay time between the pump and probe beams. The goal of this chapter is to show relevant mechanisms of excitation of coherent phonons by ultrashort pulses.

In this chapter, I will cover my three projects in three different semiconductor systems. The first section shows the thermal reversible ultrafast melting in bulk CdSe.[1] In the second section, the coherent thermal phonons in the Bi_2Te_3/Sb_2Te_3 superlattice are directly measured and compare with bulk Bi_2Te_3.[2] The third section reveals the evidence of quantum coherent coupling in the GaAs/AlAs superlattice.

3.1 CADMIUM SELENIDE

Cadmium Selenide (CdSe) is a widely used II–IV group semiconductor with a band gap lying in the solar spectrum[109]. Most effort has been devoted to developing high

---

[1] Wu, W., He, F., & Wang, Y. (2016). Reversible ultrafast melting in bulk CdSe. Journal of Applied Physics, 119(5), 055701. (Both Wu, W. and He, F. contribute equally. He, F. has performed the experiments.)

[2] He, F., Wu, W., & Wang, Y. (2016). Direct measurement of coherent thermal phonons in Bi_2Te_3/Sb_2Te_3 superlattice. Applied Physics A, 122(8), 777.

efficiency solar cells with CdSe quantum dot, which possesses discrete bands for multi-carrier excitation[110,111], meanwhile, the CdSe quantum dot has an extremely low thermal conductivity[112] due to size effect, leading to lower temperature required for phase transformation to happen than the bulk. While rare studies talk about light-induced phase transformation in bulk or nanocrystalline CdSe. In this work [21], transient reflectivity changes in bulk CdSe have been measured with two-color femtosecond pump-probe spectroscopy under a wide range of pump fluences. Three regions of reflectivity change with pump fluences have been consistently revealed for excited carrier density, coherent phonon amplitude, and lattice temperature.

3.1.1 Reversible Ultrafast Melting in Bulk CdSe

All the experiments were performed in a standard collinear two-color (3.10 *eV* pump and 1.55 *eV* probe) pump-probe scheme. Laser pulses with a 35 *fs* FWHM are generated by a mode-locked Ti: sapphire and a maximum pulse energy about 1.2 *mJ*. The pump and probe beams are focused onto the sample at normal incidence with diameters of 80 and 20 *μm*, respectively. The pump beam is modulated by an optical chopper at 500*Hz* which works with a lock-in amplifier to obtain the signal. The reflected probe beam is measured with a balance photodetector. The sample under investigation is a bulk CdSe (5×5×2 *mm*) polycrystal with a wurtzite structure, and the cleaved surface is perpendicular to the laser incident direction. At room temperature, the band gap of CdSe is 1.74 eV[113], therefore our pump pulse is well above the band gap and is able to excite free electrons and holes at the surface of bulk CdSe crystal.

Figure 3.1(a) and (b) show the transient reflectivity changes in bulk CdSe under a wide range of pump fluences. For all the fluences, $(-dR/R)$ demonstrates a positive sharp peak, after which its feature changes drastically with fluence. At very low fluences, e.g., 0.046 mJ/cm^2, $(-dR/R)$ decays exponentially back to its static value. At slightly higher fluences, e.g. 0.53 and 1.07 mJ/cm^2, the decay of $(-dR/R)$ clearly shows two stages: a rapid relaxation first and then a much slower one, with a turning point around 5 ps. At moderate fluences, e.g., 3.8 and 10 mJ/cm^2, the turning point still appears around 5 ps, but $(-dR/R)$ experiences a sign change. At highest fluences, $(-dR/R)$ continues to evolve after the turning point, reaching a minimum value, and then recovers slowly. The gigahertz oscillations observed here are caused by the interference of the probe light with coherent acoustic phonons (CAP) generated at the surface and travelling into the sample. Amplitudes of CAPs can be extracted by fitting the oscillations with damping harmonic functions.

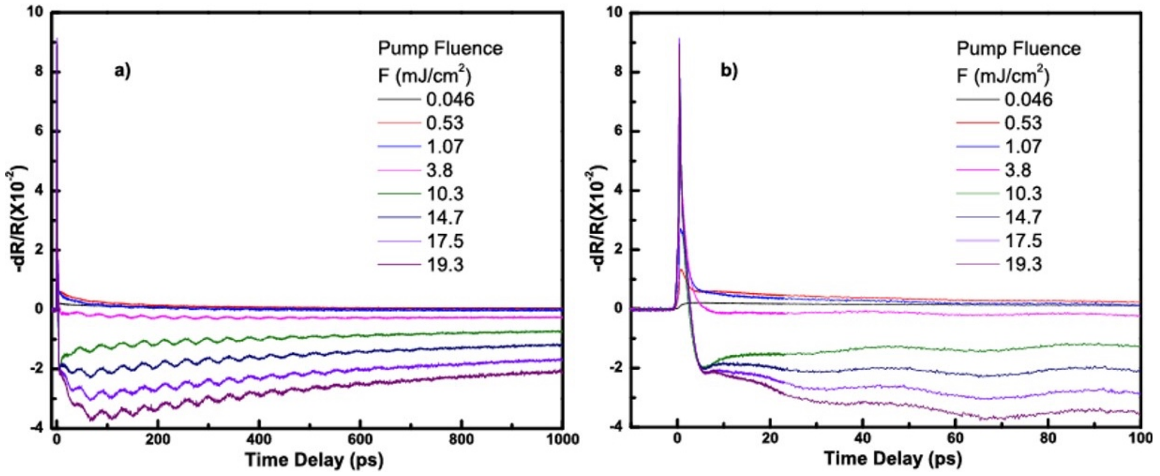

Figure 3.1 (a) Transient reflectivity $(-dR/R)$ signals of bulk CdSe measured under a wide range of pump fluences. The same transient reflectivity signals within 100 ps are shown in (b).

The changes of peak values $(-dR/R)_{max}$, amplitudes of CAPs, and values around the turning point $(-dR/R)_{5ps}$ with pump fluences have been analyzed. When the femtosecond pulses interact with semiconductor materials with bandgap smaller than photon energy, electrons on valence band absorb photons and are excited to conduction band. Electrons thermalize rapidly through electron-electron (e-e) scattering and reach a temperature (T_e) much higher than lattice temperature (T_L). Then, electrons transfer energy to lattice through electron-phonon (e-ph) scattering, and an equilibrium temperature is eventually established. The peak values of $(-dR/R)$ are usually associated with densities of excited carriers, as well as maximum electron temperature $T_{e,max}$. Since usually e-ph coupling only lasts for several picoseconds, we assume the electrons finish transferring energy to lattice around 5 ps, and $(-dR/R)_{5ps}$ is associated to the equilibrium temperature T_L.

All three curves show three distinct regions: (1) For $F \leq 1\ mJ/cm^2$, $(-dR/R)_{max}$ increases linearly, while $(-dR/R)_{5ps}$ stays at the same value. Data of CAP amplitude are not available at low fluences. (2) For $1\ mJ/cm^2 \leq F \leq 13\ mJ/cm^2$, $(-dR/R)_{max}$ continues to increase but with decreasing rates; CAP amplitudes increase along the similar trend of $(-dR/R)_{max}$; $(-dR/R)_{5ps}$ decreases rapidly, following an error-function like pattern. (3) For $F \geq 13\ mJ/cm^2$, both $(-dR/R)_{max}$ and CAP amplitudes saturate. $(-dR/R)_{5ps}$ also stops decreasing. We attribute the reason of saturation of $(-dR/R)_{max}$ to the rapidly increasing optical bandgap at high fluence; CAP amplitudes follow a similar trend because the amplitude of transient stress generating CAPs is linearly proportional to carrier density[114]. The lattice temperature T_L near sample surface can be estimated as: $T_L = T_0 + (1 - R_0)F/(\rho C_p \delta_{pump})$; where T_0 is room temperature, R_0 is static reflectivity of CdSe at room temperature, which is 0.23 at 400 *nm*, δ_{pump} is 50 *nm*[115], C_p is 0.277 *J/(gK)*, estimated at 800 K with the formula described[116]. It is a reasonable value to use for high fluences, since C_p becomes constant at high temperature. T_L is estimated to be about 1543 *K* at 13 mJ/cm^2, close to the melting temperature of bulk CdSe, 1541 K[117]. Considering the fact that probe spot size is smaller than that of pump, the actual lattice temperature sensed by probe is even higher than estimated T_L. As a result, the saturated feature of

CAP amplitude observed in Fig. 3.2(b) could be also be caused by melting at high laser fluences.

As explained earlier, $(-dR/R)_{5ps}$ is related to the equilibrium temperature T_L. Bandgap of bulk CdSe also changes with T_L[118,119]. $E_g(T_L)$ can be estimated as

$$E_g(T_L) = E_g(0) - \frac{\alpha T^2}{(T+\beta)} \tag{3.1}$$

where $E_g(0) = 1.834\ eV$ is the bandgap at zero temperature. α and β are coefficients fitted with experimental data[115], $\alpha = 4.24 \times 10^{-4}\ eV/K$ and $\beta = 118\ K$. At room temperature, E_g is 1.74 eV. When $T_L = 1543\ K$, $E_g(1543\ K)$ is estimated to be around 1.23 eV, which is smaller than probe photon energy of 1.55 eV. Bandgaps sweeping from above to below probe photon energy agrees with the sign change of $(-dR/R)_{5ps}$. For $F_{pump} \geq 13\ mJ/cm^2$, further increase of T_L is minimal because of melting, and hence no

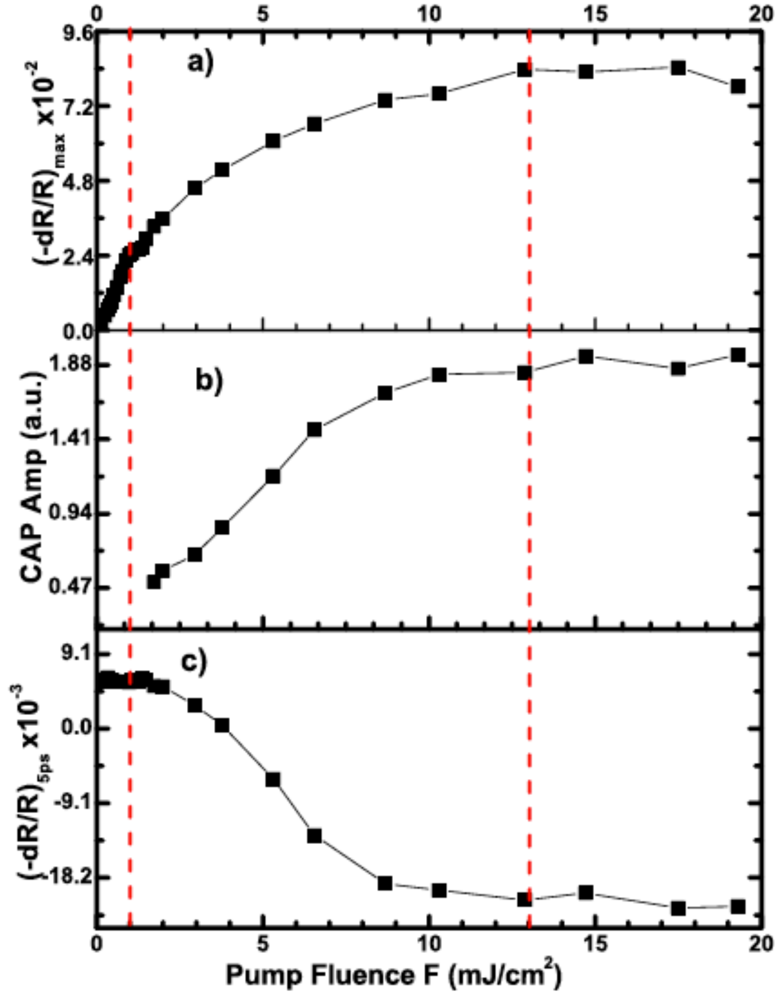

Figure 3.2 Change of (a) $(-dR/R)_{max}$, (b) coherent phonon amplitude, and (c) $(-dR/R)_{5ps}$ with pump fluences. Dashed lines mark three different regions.

further change of $(-dR/R)_{5ps}$ is observed. We want to emphasize that the picture of optical bandgap sensed by pump pulses[114] is still valid here because $(-dR/R)_{max}$ is usually reached much earlier than e-ph equilibrium. Excepetions are those with lower fluences, where $(-dR/R)_{max}$ happens around 5 ps. However, since effects of T_L are not significant at these fluences, the same explanations still hold.

Saturation features (see Fig. 3.2) all suggest that melting happens at $F_{pump} \geq 13\ mJ/cm^2$. Similar saturation features have been reported during the ultrafast melting process in $Pr_{0.5}Ca_{0.5}MnO_3$[120] and GaAs[121]. When pump fluences increases to 22.5 mJ/cm^2, after measurement, a small damaged area on sample surface was observed under the microscope, indicating an irreversible melting process under this fluence.

Even though the melting observed here happens within several picoseconds, the melting process is purely thermal, not the 'non-thermal melting' observed in some materials[122,123]. The direct evidence is that the estimated T_L at 13 mJ/cm^2 is close to melting temperature. Non-thermal melting usually happens at laser fluences much higher than single-pulse melting threshold, usually in ablation range[121]. Also, during non-thermal melting process, liquid-phase usually appears at sub-picosecond time scale, much faster than the time needed for energy transfer from carriers to phonon. Our conclusion is consistent with MD simulation results in Bi_2Te_3[81] and experimental observations in other phase change materials[124,125].

As shown in Fig. 3.1, at highest fluences, $(-dR/R)$ continues to decrease to another minimum point after the turning point, which could be attributed to propagation of melted region and then starts to recover. Recovery of $(-dR/R)$ at high fluences indicates that the ultrafast melting is reversible, comparing with the permanent melting cases where the transient reflectivity deviates further from its initial value at longer time delay[126]. Because of the uneven distribution of excited carriers in CdSe sample, T_L is highest on surface and decreases into the sample. At $F \geq 13\ mJ/cm^2$, right after e-ph equilibrium, the melted region has lattice temperature above melting temperature. However, the final state of the melted region is determined by two factors: (1) How long the lattice temperature stays above melting temperature and (2) how fast heat is extracted from the melted region due to temperature gradient. According to the MD simulation of ultrafast laser melting in Bi_2Te_3[81], isolated droplet-like liquid areas appear first, which then grow and get connected to form a continuous melted region. If laser fluence is not enough, heat will be dissipated deeper into the sample quickly, and lattice temperature will drop below melting temperature before the isolated liquid drops growing into a continuous melted region. In this case, the isolated liquid drops will recrystallize, and no amorphous structure could be observed at final state. This picture is consistent with the reversible melting observed in bulk CdSe. An amorphous structure could be achieved under relatively low laser fluence, if a thin film of CdSe with thickness less than pump laser absorption depth is deposited on a substrate with low thermal conductivity, e.g., glass, or in nanocrystalline CdSe[127], where heat transport is greatly suppressed by boundary scatterings. Figure 3.1 also reveals a change of sign of $(-dR/R)$ for $F \geq 13\ mJ/cm^2$. As discussed earlier that bandgap of bulk CdSe has a strong dependence on lattice temperature. $(-dR/R = 0)$ could be understood as a result of lattice temperature T_L^* at which $E_g(T_L^*)$ is slightly higher than $1.55\ eV$, where interband transition from probe photon is prohibited and no electrons are left on conduction band for free-carrier absorption. When laser fluence is below $3.8\ mJ/cm^2$, heat generated in excited region transport out of excitation area before lattice temperature reaches T_L^*, so $(-\,dR/R)$ never reaches zero.

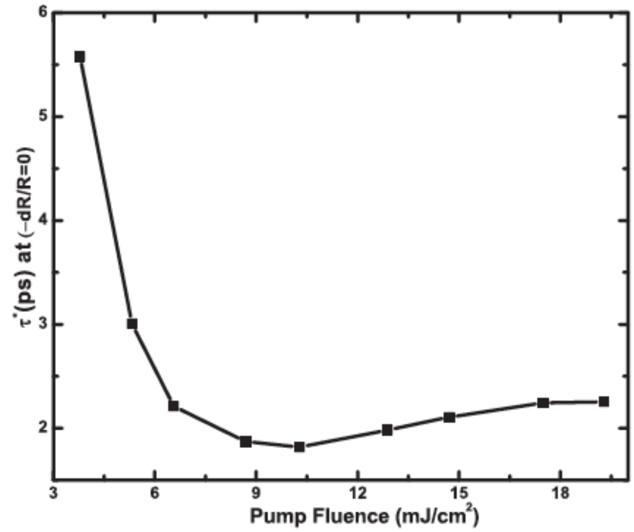

Figure 3.3 The time when $(-\,dR/R)$ is zero under different pump fluences.

The time delay τ^* when $(-\,dR/R)\sim 0$ is plotted in Fig. 3.3: τ^* decreases very rapidly for fluences above 3.78 mJ/cm^2 but below 13 mJ/cm^2. τ^* can be approximated to be the electron-phonon coupling time in bulk CdSe, which is the inverse of energy transfer rate γ from excited electron to phonon. Form the two-temperature model[128], γ is proportional to $g[T_e(t) - T_L(t)]$, where g is the electron-phonon coupling factor and T_e is the electron temperature. Before melting happens, g is roughly a constant, and $T_e(t) \gg T_L(t)$ for most of the time range. So τ^* is approximately proportionally to $1/T_e$. This conclusion qualitatively agrees with fluence-dependent $T_{e,max}$ (approximately proportional to $(-\,dR/R)_{max}$) as shown in Fig. 3.2. When $F \geq 13$ mJ/cm^2, electron-phonon coupling factor becomes smaller due to bond softening effect, and hence τ^* increases slightly and saturates at highest fluences when melting happens.

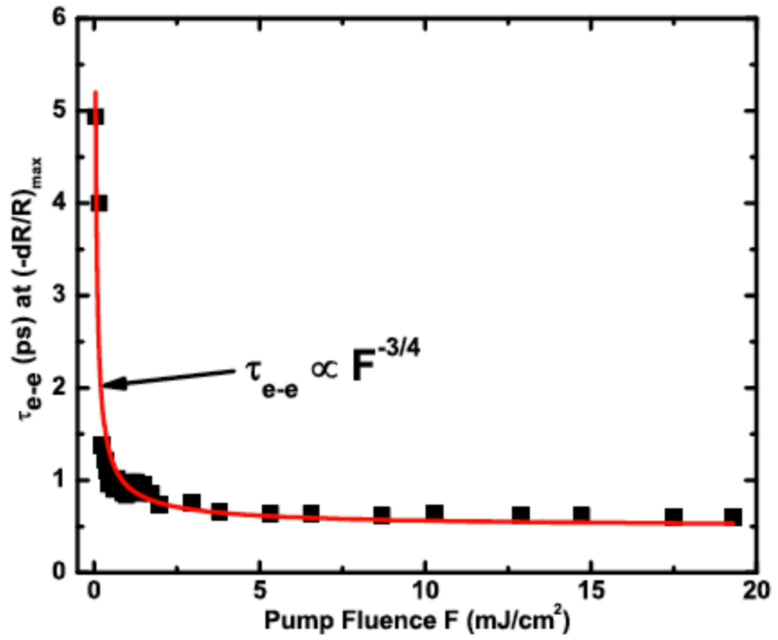

Figure 3.4 The time delay τ_{e-e} when $(-dR/R)$ reaches maximum under different fluences.

As discussed earlier, $(-dR/R)_{max}$ is related to $T_{e,max}$. The time delays when $(-dR/R)$ reaches maximum values are roughly the e-e thermalization time. Fig. 3.4 shows the τ_{e-e} at different pump fluences. It can be seen that τ_{e-e} first decreases rapidly and stops decreasing when F is above 1 mJ/cm^2. If the curve is fitted with a power function, τ_{e-e} is proportional to $F^{-3/4}$. The initial decrease of τ_{e-e} with pump fluence comes from stronger carrier-carrier scattering at higher carrier densities, which is consistent with earlier results[129]. The stabilized thermalization time is less than 1ps, which is also consistent with reported values in other materials[130].

3.1.2 Summary

In summary, we have measured the transient reflectivity changes in bulk CdSe with a two-color femtosecond pump-probe spectroscopy under a wide range of pump fluences. Three regions of reflectivity change with pump fluences have been consistently revealed in excited carrier density, coherent phonon amplitude, and lattice temperature. For laser fluences from 13 to 19.5 mJ/cm^2, ultrafast melting happens in several picoseconds. This melting process is purely thermal reversible. A complete phase transformation in bulk CdSe may be reached when the absorbed laser energy can be localized for a long enough time, as observed in nanocrystalline CdSe.

3.2 BISMUTH TELLURIDE AND ANTIMONY TELLURIDE SUPERLATTICE

Not all phonons contribute to the heat transport equally. Phonons that are thermally important are called 'thermal phonons'. Conventionally, we will not consider the coherence of the phonons in the bulk materials when we calculate the scattering rate using the Boltzmann equation[79]. However, in some special material systems, like superlattices, phase information can be important.

Bi_2Te_3/Sb_2Te_3 superlattices can be grown with a metal-organic chemical-vapor deposition (MOCVD) technique with high-quality interfaces[131,132]. Studies have shown that cross-plane thermal conductivity for Bi_2Te_3/Sb_2Te_3 superlattice is significantly lower than its bulk counterparts, even lower than its corresponding alloy, making it promising for achieving high ZT thermoelectric materials[95]. Thermal conductivity measurements of Bi_2Te_3/Sb_2Te_3 superlattices have also shown a minimum thermal conductivity around a period thickness of 4~6 *nm*[95], similar to that observed in $SiTiO_3/BaTiO_3$ superlattices[97]. Therefore, coherent phonon conduction could also play an important role in Bi_2Te_3/Sb_2Te_3 superlattices.

3.2.1 Coherent Thermal Phonons in Bi_2Te_3/Sb_2Te_3

Phonon lifetimes have been extracted from experimental data, with which mode-wise thermal conductivities have been calculated. Comparing with bulk Bi_2Te_3, the estimated mode-wise thermal conductivity of longitudinal acoustic phonons shifts to higher frequencies, due to constructive coherent phonon interference[33].

Using a mode-locked Ti: Sapphire femtosecond laser (Tsunami, Spectra Physics), a single-color pump-probe experiment is performed in non-collinear reflection geometry at room temperature. Both pump and probe pulses have 800 *nm* central wavelength, 35 *fs* pulse width and 76 *MHz* repetition rate. The pump and probe beams are focused onto the sample surface by a 72.5 *mm* lens, with spot sizes of 30 μm and 24 μm, respectively. An optical delay line placed in the pump-beam optical path is used to control the delay time between pump and probe beams. The difference between reflected and reference probe beams is measured by subtracting signals from two single detectors (DET110, Thorlabs).

A lock-in amplifier (model 7265, Signal recovery) with a chopper working at 2.2 *kHz* is used to acquire the data. A mechanical shaker was incorporated into the spectrometer for fast averaging. The sample studied is a Bi_2Te_3/Sb_2Te_3 SL grown with the metal-organic chemical-vapor deposition (MOCVD) technique on GaAs (100) substrates along the c axis of the films[95,131,133,134]. The SL has about 200 periods with a 1 *nm* Bi_2Te_3 layer and a 1 *nm* Sb_2Te_3 layer for each period. A Bi_2Te_3 buffer layer is placed between the SL and the substrate.

Coherent acoustic phonons can be generated with femtosecond laser pulses via launching a strain wave near sample surface, which is a group of coherent phonons traveling with the same velocity. As shown in Fig. 3.5 (a), the strain wave propagates into the sample, and be partially transmitted/reflected at the interface. When a probe photon is scattered by a phonon, the maximum phonon vector that can be detected is $k_{phonon} = 2k_{probe}$ (backscattering of probe photon), to satisfy momentum conservation. This process is called Stimulative Brillouin Light Scattering (SBLS). If the probe laser has a shorter penetration depth, it will only detect the acoustic wave packet after it is reflected at interface and travels back to sample surface. The acoustic wave packet detected in Bi_2Te_3/Sb_2Te_3 superlattice is shown in Fig. 3.5 (b)[135]. The temporal expansion of the acoustic echo (Δt) corresponds to coherence time, which is related to phonon coherence length, $l_c = v \cdot \Delta t$. The difference of time delays when the acoustic wave packet is detected first time (τ_1) and second time (τ_2) is the round-trip time that coherent phonon travels in the sample. Phonon group velocity can be derived as: $v = \frac{2 \cdot L}{\tau_2 - \tau_1}$. It can also be seen in Fig. 3.5 (b) that the amplitude of coherent phonon decreases after propagating a longer distance. Eventually the acoustic wave packet will disappear when all phonons are scattered. This time constant of phonon amplitude decay is called coherent phonon lifetime, which is related to phonon mean-free-path, $\Lambda = v \cdot \tau$. In bulk materials, phonons with $k_{phonon} = 2k_{probe}$ usually have a very low frequency and hence are not thermally important. Fig. 3.5 (c) shows acoustic phonon dispersion in two SL structures with different periods calculated with an elastic continuum model[72,74]. In the SL, due to phonon folding, many high frequency phonons also fall into the $0 \sim 2k_{probe}$ region and hence more coherent phonons can be generated and detected. Broadband coherent optical phonons up to 2.5 *THz* have been detected in InGaN/GaN SL with coherent phonon spectroscopy[78].

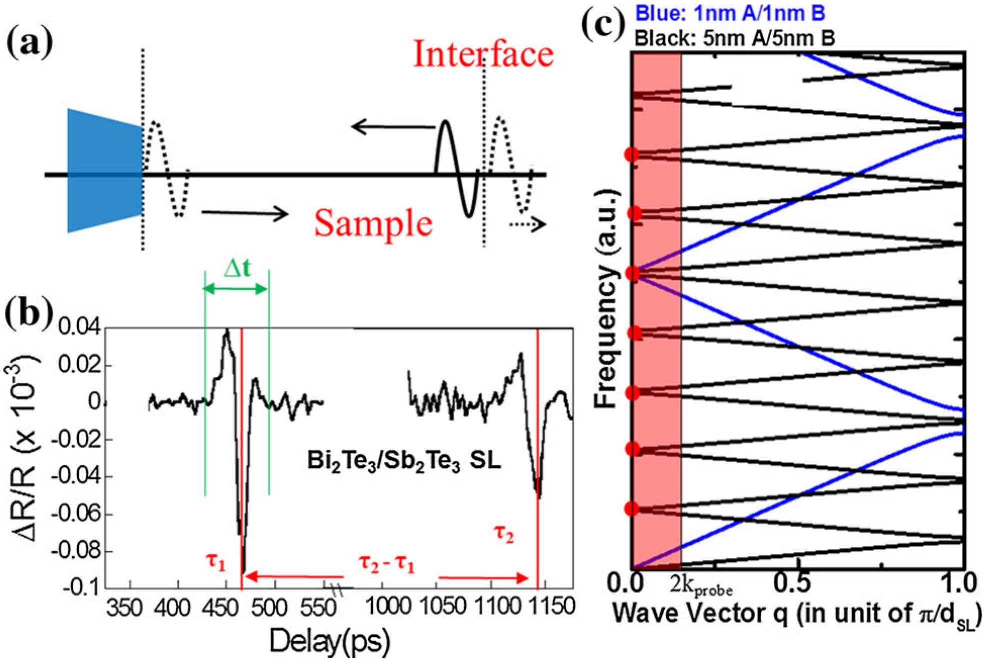

Figure 3.5 **(a)** Schematic picture of coherent phonon generation/propagation in bulk; **(b)** Acoustic echo measured in Bi_2Te_3/Sb_2Te_3 SL [Adapted from Ref. 135]; **(c)** Acoustic phonon dispersion in two SL structures with different periods calculated with an elastic continuum model; the SL with a larger period thickness introduces more phonon folding.

Figure 3.5 (a) shows the transient reflectivity signal measured in Bi_2Te_3/Sb_2Te_3 superlattice with degenerate CPS, with 800 *nm* wavelength, 35 *fs* pulse width for both pump and probe beam. The sharp decrease around zero-time delay is due to electron excitation by pump pulse. The decaying background represents electron relaxation, mainly a result of electron-phonon scattering. The oscillatory component is related to coherent phonons generated in SL structure. Inset of Fig. 3.6 (a) shows pure coherent phonon signals after removing electronic signals with a digital high-pass filter. The complex feature shown in coherent phonon signals comes from superposition of multiple phonon waves, which makes direct fitting to extract phonon information impractical.

Instead, the short-time Fourier transform (STFT) method has been applied to the pure coherent phonon signals to extract phonon frequencies, and to reveal the evolution of coherent phonons with time. A proper window size has been chosen to achieve reasonable resolutions in both time and frequency domains. From the frequency axis, two groups of phonons are clearly shown: acoustic phonons with a frequency below 1 *THz*, and optical phonons with a frequency between 1~2 *THz*, with a gap present between these two groups of phonons. A similar trend has been observed for phonons in bulk Bi_2Te_3[80].

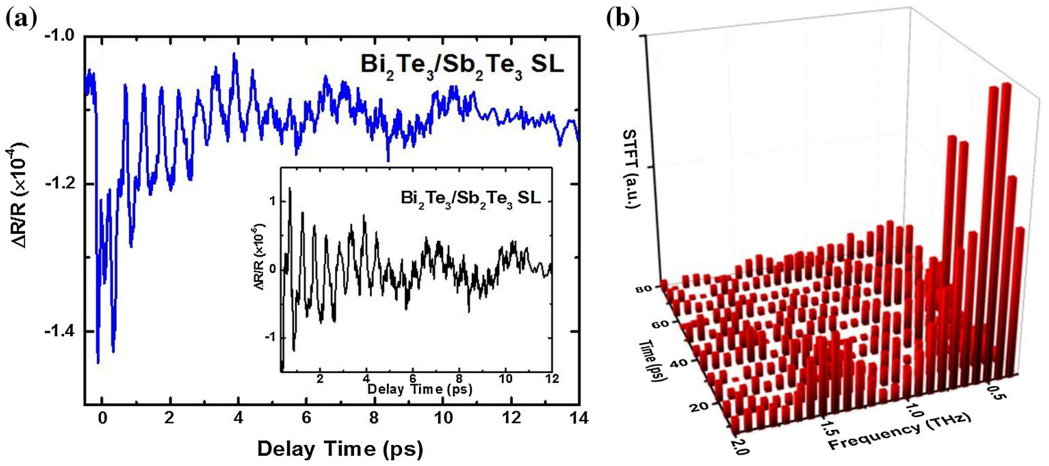

Figure 3.6 (a) High frequency coherent phonons measured in Bi_2Te_3/Sb_2Te_3 SL. Inset show coherent phonon signals after removing electronic background; (b) Short-time Fourier Transform (STFT) of phonon oscillations showing both optical and acoustic phonons.

STFT amplitudes of a phonon mode at 0.57 *THz* are plotted in Fig. 3.6(a). A decaying exponential function is used to fit STFT amplitudes to extract phonon lifetime, which is about 2.2 *ps* for phonon at 0.57 *THz*. Figure 3.6 (b) plots extracted phonon lifetimes of both acoustic and optical phonons in Bi_2Te_3/Sb_2Te_3 SL. Lifetimes of acoustic phonon range from 1 *ps* to 9 *ps*; those of optical phonons range from 2.5 *ps* to 7.5 *ps*. Acoustic phonons below 300 *GHz* are not plotted due to large uncertainties. In bulk Bi_2Te_3, the previously measured lifetime of the A_{1g} optical coherent phonon (1.88 *THz*) is about 5 *ps*[80], which falls into the same range with optical phonon lifetimes measured in this work. Lifetimes of acoustic phonons are generally shorter than those calculated in bulk Bi_2Te_3[80], due to scattering at SL interfaces.

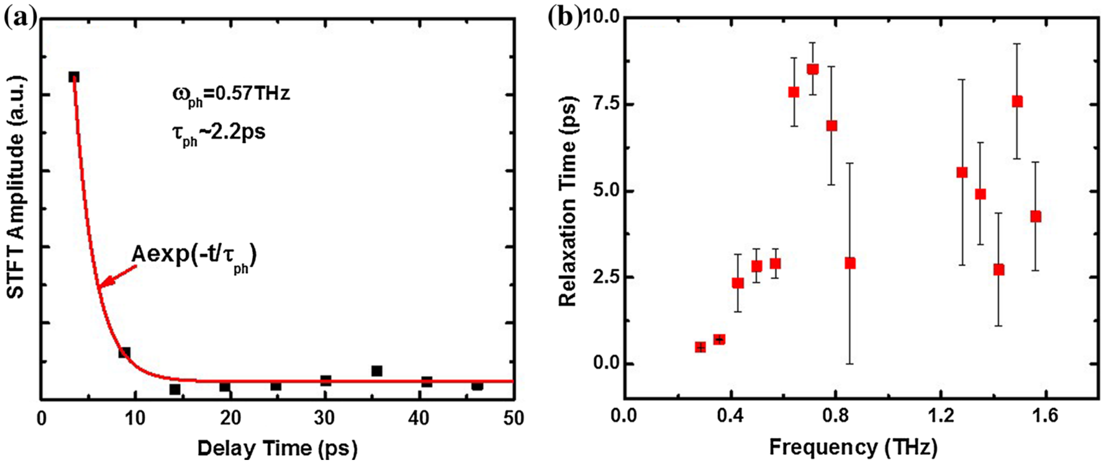

Figure 3.7 (a) STFT amplitudes of coherent phonon at 0.57 *THz* and its exponential fitting; the extracted phonon lifetime is about 2.2 *ps*; (b) Phonon lifetimes of longitudinal acoustic and optical phonons extracted from STFT.

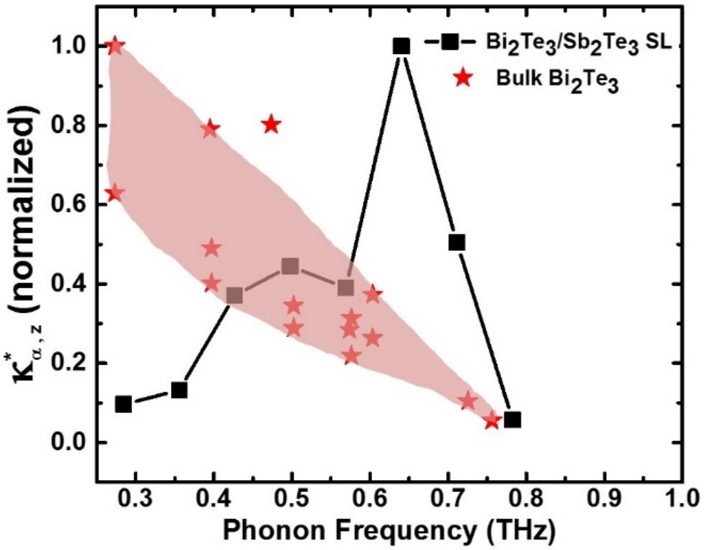

Figure 3.8 Normalized mode-wise thermal conductivities of longitudinal acoustic phonons along Γ-Z direction. Comparing with bulk Bi_2Te_3, the spectrum of mode-wise thermal conductivities in Bi_2Te_3/Sb_2Te_3 SL shifts to higher frequencies. The line and the shaded area are just for eye guidance.

The normalized mode-wise thermal conductivities (see Fig. 3.7) of longitudinal acoustic phonons along the Γ-Z direction, $\kappa^*_{L,z} = \frac{C_\alpha v_\alpha^2 \tau_\alpha}{(C_\alpha v_\alpha^2 \tau_\alpha)_{max}}$, for both bulk Bi_2Te_3 and Bi_2Te_3/Sb_2Te_3 SL. Phonon velocities of bulk Bi_2Te_3 are derived from dispersion curves calculated with Lattice Dynamics (GULP[136]), and phonon lifetimes of bulk Bi_2Te_3 are adapted from Ref. 80, calculated with Normal Mode Analysis (NMA)[80]. Specific heat per phonon mode is approximated as $1/2k_B$ (k_B is Boltzmann Constant) because Debye temperature of both Bi_2Te_3 (155 K)[80] and Sb_2Te_3 (165 K)[137] are much lower than room temperature. Phonon velocities of Bi_2Te_3/Sb_2Te_3 SL are approximated as the same as those of bulk Bi_2Te_3 at the same frequency, because Bi_2Te_3 and Sb_2Te_3 have very similar elastic properties[138,139]. Since the phonon velocity reduction caused by folding does not depend on phonon frequency, its effect is not reflected in normalized mode-wise thermal conductivity. In bulk Bi_2Te_3, $\kappa_{L,z}^{*}$ decreases with phonon frequency, while in SL, $\kappa_{L,z}^{*}$ spectrum shows a broad peak at intermediate frequencies, with much smaller values at lowest and highest frequencies. This spectrum shift of $\kappa_{L,z}^{*}$ in SL has several important implications: (a) with coherent phonon spectroscopy, only coherent phonons near the zone center region can be detected ($k_{phonon} = 2k_{probe}$), while results of bulk Bi_2Te_3 calculated with NMA include all the k points along Γ-Z direction. Successful detection of high-frequency coherent acoustic phonons in SL is a direct evidence of phonon zone-folding in SL, which generates new phonon modes near the zone-center region. (b) Phonon scattering in SL structure is selective, weaker on some modes, while stronger on others. (c) SL structure can preferably allow propagation of certain coherent phonon modes, which is a result of constructive interference. Therefore, it is possible to manipulate CTP in SL structures in a similar way to photons.

3.2.2 Summary

In summary, coherent phonon spectroscopy has been applied to excite and detect CTP in Bi_2Te_3/Sb_2Te_3 superlattice. Phonon lifetimes have been extracted by exponential fitting of the decaying STFT amplitudes. Comparing with bulk Bi_2Te_3, spectrum of mode-wise thermal conductivities of longitudinal acoustic phonons along Γ-Z direction in SL shows a shift to higher frequencies. Our results suggest that it is possible to use SL structure to manipulate coherent phonon propagation and to tailor thermal conductivity.

3.3 GALLIUM ARSENIDE AND ALUMINUM ARSENIDE SUPERLATTICE

GaAs/AlAs superlattices (SLs) are excellent systems to study coherent phonons[26-28,30,31,140-144] in nanostructured materials since the lattice mismatch is smaller than 0.1% (5.653 Å for GaAs and 5.660 Å for AlAs)[145], allowing for the fabrication of high quality lattice-matched SLs. Raman scattering study of GaAs/AlAs SLs has been established for a long time[60,73,146]. This also attracted attention of heat transport[94,106,147-149]. Recently, Chen et al.,[150] also reported the appearance of phonon localization. Perrin et. al., investigated the nonlinear response in GaAs/AlAs SLs and even strong optical-mechanical coupling in a GaAs/AlAs microcavity[25,52]. In addition, the direct bandgap for GaAs is 1.424 eV, AlAs is 3.03 eV at 300 K[145], which is suitable to study for most Ti-Sapphire femtosecond lasers.

3.3.1 Sample Information

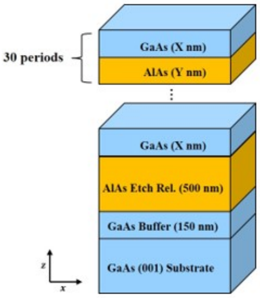

Sample ID X/Y	Actual SL period thickness (target) [Å]	Average T of Ga per period (target) [Å]	Average T of Al per period (target) [Å]
1/1	18.14 (20)	~18.14/2 (10)	~18.14/2 (10)
2/2	38.75 (40)	~38.75/2 (20)	~38.75/2 (20)
3/3	59.1 (60)	27.51 (30)	31.59 (30)
6/6	118.97 (120)	59.83 (60)	59.13 (60)
8/8	157.7 (160)	79.48 (80)	78.22 (80)
14/2	159 (160)	139.47 (140)	19.525 (20)
40/1	399 (410)	386 (400)	12.8 (10)

Figure 3.9 (Left) Schematic SL structure; (Right) Sample information with XRD characterization.

The samples studied are GaAs/AlAs SL sets with different periodicity grown with molecular beam epitaxy (MBE) by Nathanial Sheehan from Dr. Seth Bank's group. High quality SL structures will be grown on GaAs (001). As shown in Fig. 3.9, a 500 *nm* AlAs etching layer and a 150 *nm* GaAs buffer layer are grown on (001) GaAs wafer substrate for further transferring process. The SLs are prepared from 1 *nm*/1 *nm* to 40 *nm*/1 *nm* accordingly with 30 periods. The absorption depth for GaAs at 800nm is 743.2 *nm*[151].

Characterization of the period thickness for GaAs/AlAs SL sample sets have been performed with XRD (see Fig. 3.10), where we can see the significant peaks for SL (0) SL (-1) and SL (+1). We have also used photoluminescence (PL) (see Fig. 3.11) to determine the bandgap for different SL samples. Raman spectroscopy has been applied to reveal the folded acoustic phonons[73,146] in these semiconductor SLs. PL and low cut-off Raman spectroscopy are taken under the help with Jason in Dr. Lin's lab. In Fig. 3.11(a), we can clearly see that with decreasing periodicity, the band gap is increasing, which can be well explained in quantum mechanics, i.e., the narrower the quantum well is, the higher the ground state is.

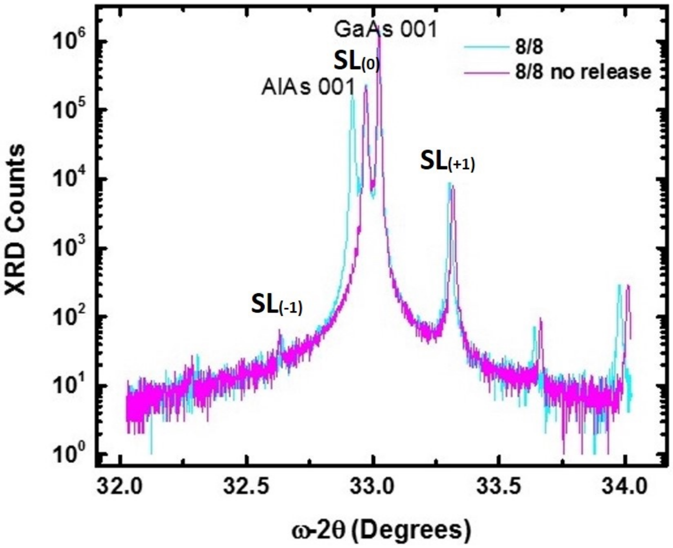

Figure 3.10 XRD characterization for 8/8 and 8/8 without AlAs releasing layer. The SL (0) SL (-1) and SL (+1) peaks are shown.

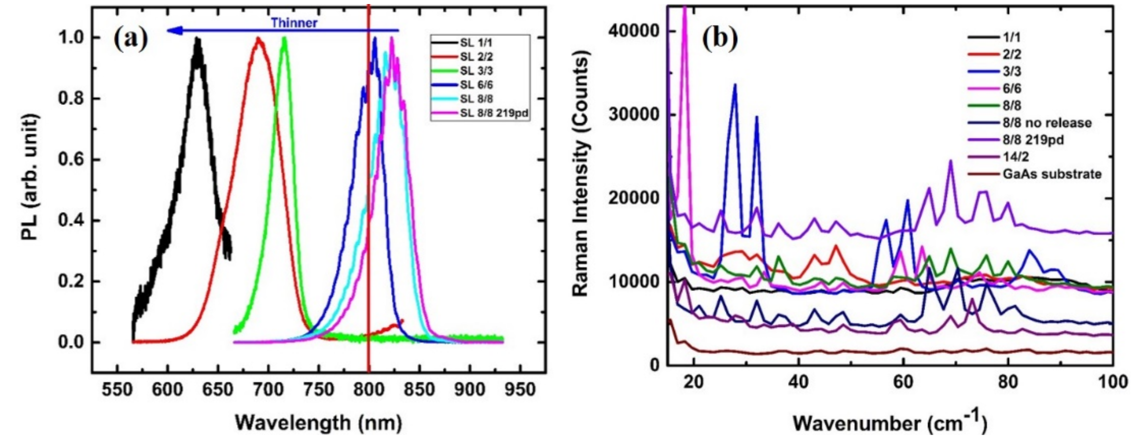

Figure 3.11 (a) PL of all SL structures: with thinner SL periods, PL has blue shifts; (b) Low cut-off Raman of all SLs: we can see multiple doublets for SL.

Low cut-off Raman spectra for the sample sets can be seen form Fig. 3.11(b), aiming to reveal the 2*k* doublets modes. The GaAs substrate shows no Raman peaks in the range of 20-100 cm^{-1} while the GaAs/AlAs sample sets all show Raman peaks in this range.

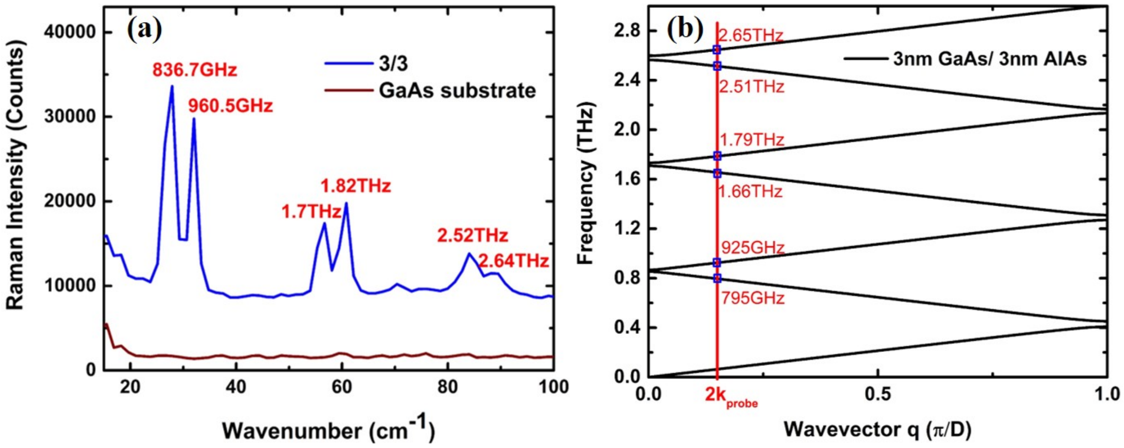

Figure 3.12 (a) Raman spectra for sample 3/3; (b) Calculated dispersion curve for LA phonons within the first mini-Brillouin zone using Eq. (1.39). Marked frequencies are the 2*k* modes.

To have a better understanding, sample 3/3 is chosen to study. Fig. 3.12(a) shows the Raman spectra for 3/3 and Fig. 3.12(b) shows the calculated LA dispersion curve for SL 3/3. By comparing the observed doublets with the computed doublets, we can see they match. To better match the experimentally observed doublets, further adjustment of the thickness for GaAs and AlAs will be needed. This Raman spectrum verifies the origin of the coherent phonons we observed in CPS in Fig. 3.13 is ISBS.

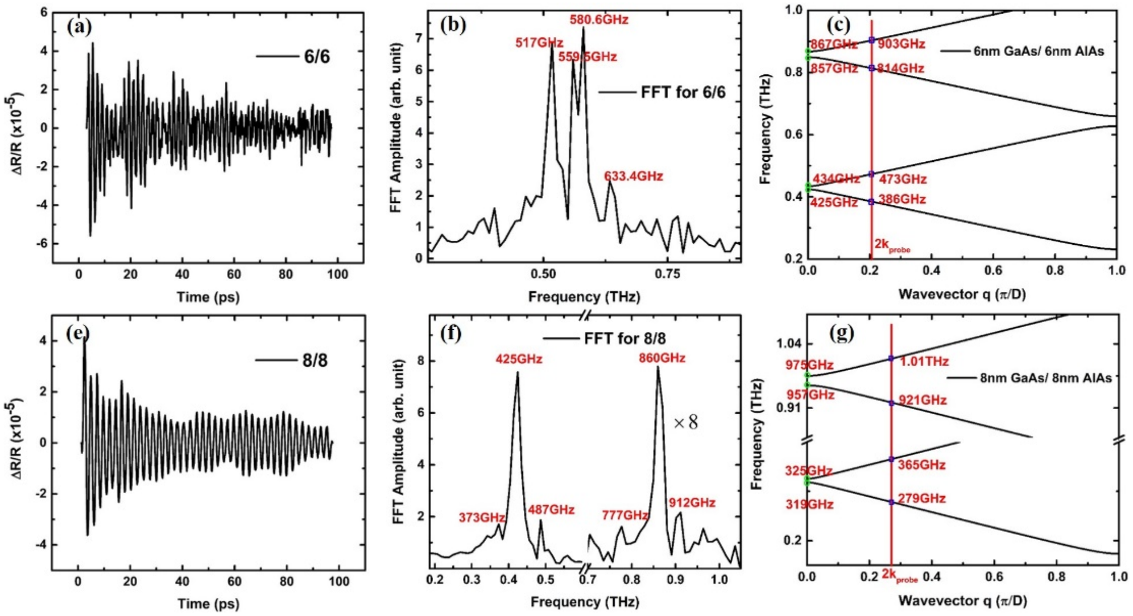

Figure 3.13 (a) (c) High frequency phonon signals after removing the electronic/thermal background measured in GaAs/AlAs 6/6 and 8/8 SL; (b) (f) Fourier amplitude spectra of coherent phonon oscillations for 6/6 and 8/8; (c) (g) Calculated dispersion curve for LA phonons within the first mini-Brillouin zone using Eq. (1.39).

High frequency phonon signals after removing the electronic/thermal background are shown in Fig. 3.13 (a)& (d). From the FFT amplitude spectra in Fig. 3.13 (b)& (f), we can clearly see oscillations in different frequencies. In Fig. 3.13 (c)& (g), the observed frequencies are compared to the computed dispersion curves for folded LA branch in the mini-Brillouin zone[27,28,72]. We used acoustic velocities of 4719ms^{-1} and 5718ms^{-1} for GaAs and AlAs respectively[152]. To match the experimentally observed frequencies, we'll need to adjust the thickness of GaAs/AlAs layer thickness. In Fig. 3.13 (b), we can observe four frequency peaks, where two (580.6 GHz and 559.5 GHz) of them are zone-center modes. The rest two (517 GHz and 633.4 GHz) are $q = 2k$ modes, where k is the wavenumber of the probe light. Although from the selection rule, only symmetric modes are Raman active, the finite number of periods can break the mode symmetry[27].

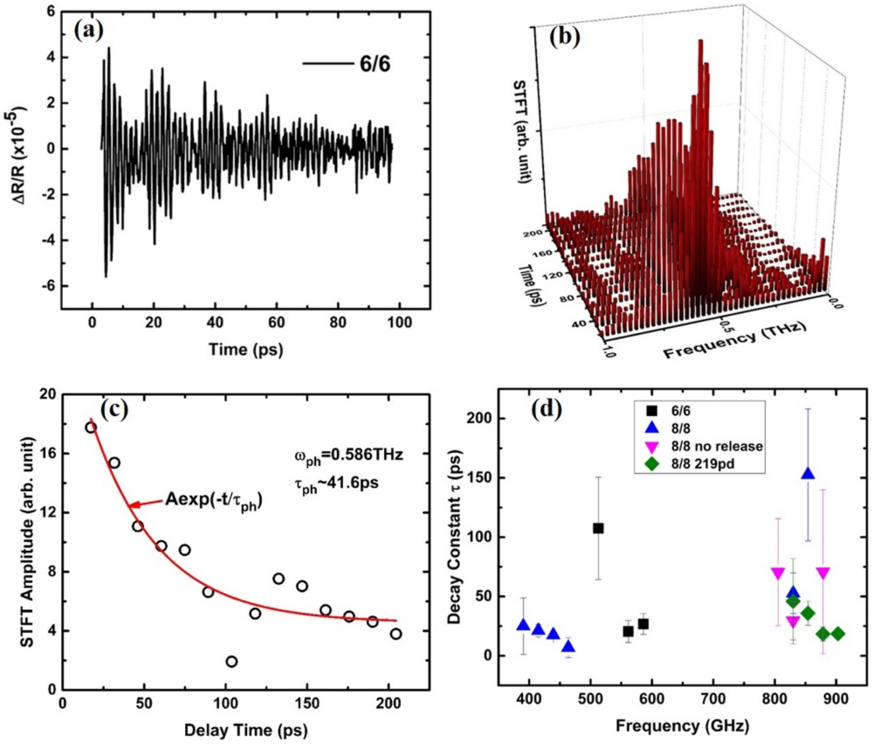

Figure 3.14 (a) High frequency phonons measured in GaAs/AlAs 6*nm*/6*nm* SL; (b) Short-time Fourier transfer (STFT) of phonon oscillations of a group of acoustic phonon around 0.5 *THz*; (c) STFT amplitudes of coherent phonon at 0.57 *THz* and its exponential fitting; the extracted lifetime is about 41.6 *ps*; (d) Phonon lifetimes for longitudinal acoustic (LA) phonons extracted from STFT.

Since from Fig. 3.13(b), we can see that the signal Fig. 3.14(a) comes from the superposition of multiple phonon modes, which makes direct fitting to extract phonon information impractical. Instead, a short-time Fourier transform (STFT) method has been applied to the pure coherent phonon signals to extract phonon frequencies and to reveal the evolution of coherent phonons with time. A proper window size has been chosen to achieve reasonable resolutions in both time and frequency domains. From the frequency axis, a group of phonons around 0.5 *THz* are clearly shown. STFT amplitudes of a phonon mode at 0.586 *THz* are plotted in Fig. 3.14 (c). A delaying exponential function is used to fit STFT amplitudes to extract the phonon lifetime, which is about 41.6 *ps* for phonon at 0.586 *THz*. Figure 8(d) plots the extracted phonon lifetimes for LA from STFT in different GaAs/AlAs SLs we have studied.

A Short-Time Fourier Transform (STFT) was applied to analyze the signal. It has different choices in 'FFT length', 'Window length' and 'Overlap'. The 'FFT length' is usually larger than the 'window length' and zeros will be added on both sides of each windowed data segment, increasing the frequency resolution. The size of the window is related to the time resolution and frequency resolution, the shorter the window, the higher the time resolution, but poor frequency resolution. The overlapping size, on the other hand, is related to the size of the STFT result matrix and can detect changes between adjacent data frames, but it will increase the computation time.

As shown in Fig. 3.15, (a) gives us the comparison of the Low cut-off Raman scattering spectrum for the GaAs substrate and the SL 6/6 where the SL 6/6 clearly shows significantly different doublets features than the bulk GaAs which is in agreement with other reports[60,73,146]. With a Lorentz peak fitting (see Fig. 3.15 (b)) and a conversion of the FWHW w of the fitted peak to the decay time using the relation[153] $t = \frac{5.3}{w} ps$, we can extract the decay time as shown in (c). By comparing with the decay constant extracted from the pump-probe experiment using STFT as shown in (d), we can see the decay constant from spontaneous Raman scattering (~4 *ps*, incoherent phonons) is smaller than that of the pump-probe experiment (~25 *ps*, coherent phonons). This is a very interesting phenomenon since in other materials, like diamond and polycrystalline Bi[88,89], the decay rate shows the same behavior for the coherent and incoherent phonons where a coherent anti-stokes Raman scattering (CARS) technique was used to measure the decay rate for coherent phonons, and therefore they concluded that the anharmonic decay is the main source of decoherence. However, in our measurement, the decay time for incoherent phonon is smaller than that of the coherent phonon which could be because of the insufficient resolution for the Low cut-off Raman scattering, or because in the superlattice structures, anharmonic scattering is greatly reduced for coherent phonons, and thus the decay constant is larger. The coherent phonons may have the potential to suppress anharmonic scattering and increase the phonon coherence time, therefore, it's promising to introduce coherent phonons to tailor the thermal conductivity of the SL structures.

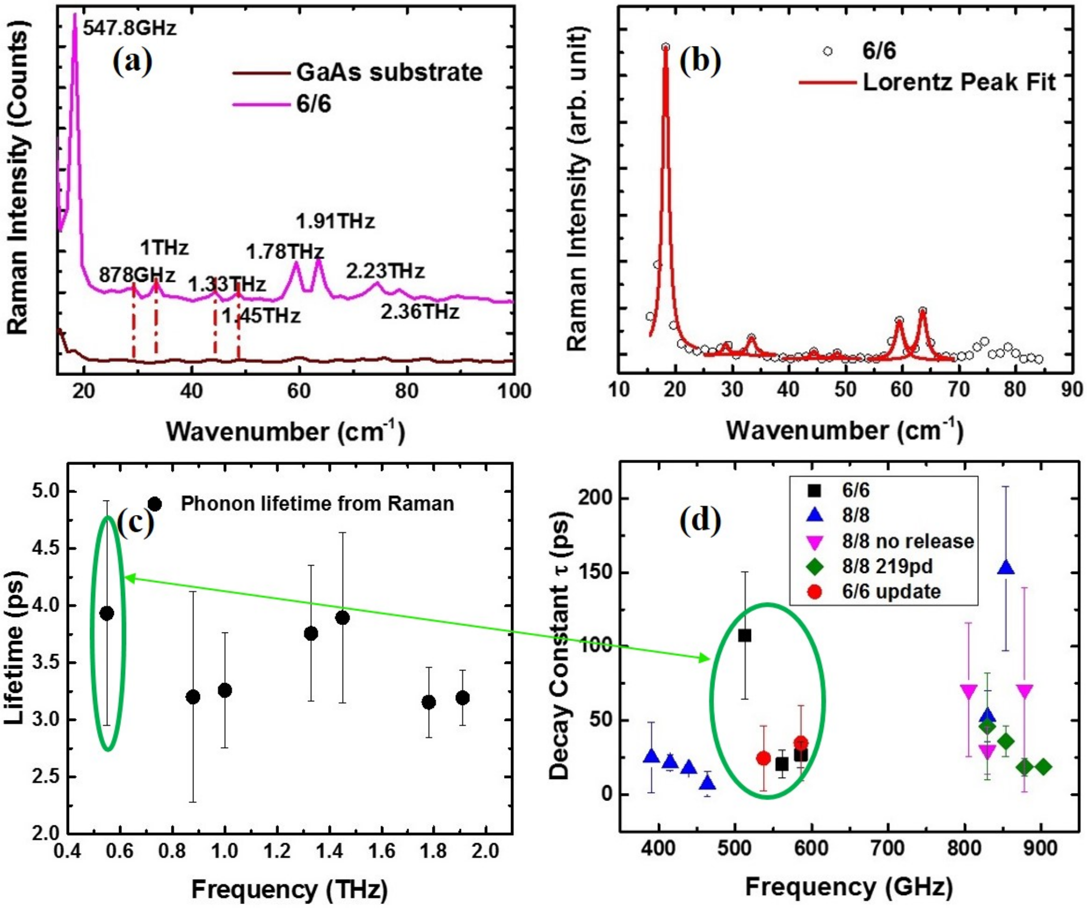

Figure 3.15 (a) Low cut-off Raman for 6/6 and GaAs substrate, we can observe significant doublets on the spectrum of 6/6; (b) Lorentz peak fit for 6/6 Raman scattering; (c) Decay time extracted from (b); (d) Decay constant extracted from STFT; the green circles are for the close frequencies.

3.3.2 Phonon-phonon Quantum Coherent Coupling in GaAs/AlAs Superlattice

Similar to photon-phonon quantum coherent coupling in the optomechanical cavities (see Chapter 1.1.4), one phonon mode is also able to couple with another phonon mode coherently through a nonlinear process[1,2,48,154] as long as the coupling constant between them is large enough and exceeds the decoherence rate of each phonon mode.

Misochko et al[32]. has observed the amplitude collapse and revival of the coherent phonons in Bi after entering the high nonlinear region, which they claimed to be nonclassical states. Although later it was claimed to be caused by the inhomogeneity excitation of the coherent phonons with the pump and probe beam size to be the same[155,156], it's still promising to observe the 'quantum beats' under very low temperatures where the decoherence rate is much smaller and introduce two pump pulses to cancel out the coherent phonon signal which is usually too strong[157].

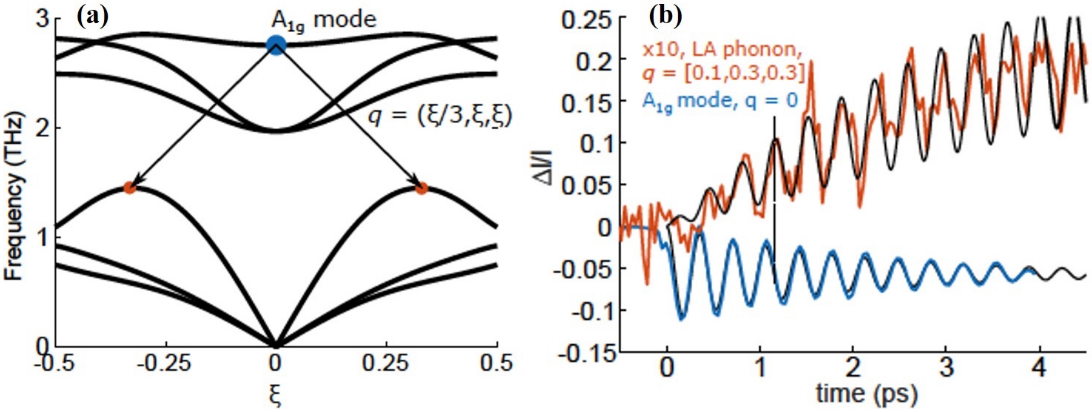

Figure 3.16 (a) Bismuth phonon dispersion relation along the $q = (\xi/3, \xi, \xi)$ direction, illuminating a decay channel of an A_{1g} mode into a pair of LA modes at q and $-q$; (b) ultrafast diffuse X-ray scattering experimental results show the decay of A_{1g} mode in Bi by the channel shown in (a). The blue (lower) curve shows the relative intensity change of A_{1g} mode and the orange (upper) curve shows the relative intensity change in a region near $q = (0.1, 0.3, 0.3)$ in the $(0,1,1)$ zone (multiplied by 10). The black lines are simulations. The dashed line indicates a $\pi/2$ phase shift between the A_{1g} mode and the target mode. Detailed information can be found in Ref. 34.

The three-phonon scattering mechanism has been proposed for a long time as the main anharmonic scattering mechanisms and also the main intrinsic phonon decaying mechanism[57,58]. However, due to the large population of phonons in the material, it's hard to observe the individual three-phonon scattering process directly out of the phonon bath. Recently, Teitelbaum et al. has directly observed anharmonic decay of the photoexcited coherent A_{1g} into target modes by observation of the build up of the coherent oscillations of the target modes using ultrafast diffuse x-ray scattering (see Fig. 3.16)[34,59]. They claimed this three-phonon scattering process can be understood as a parametric resonance process and prepare the target modes in a squeezed state. Moreover, they have extracted the anharmonic coupling constant which is comparable with the first principles calculations[59]. This is the first time that people have directly observed the three-phonon anharmonic decay channel experimentally 50 years since it was proposed[57,58].

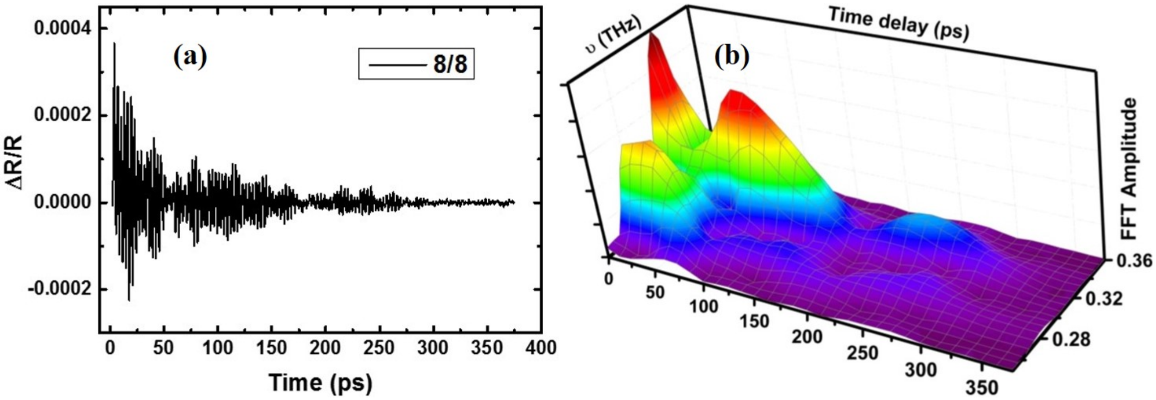

Figure 3.17 (a) Long time run at power 50 mW; (b) STFT for the data in (a) and a clear collapse and revival trend for multiple frequencies is displayed.

Since strong optical-mechanical coupling in GaAs/AlAs microcavity has been observed[52], and also the folding of phonon dispersion in SL structures provides more zone center modes (standing wave with long lifetime even at room temperature) which enables possibilities to observe a resonant parametric process and even quantum coherent coupling for the coherent zone center phonons. We have picked the SL 8/8, where the PL and low cut-off Raman spectrum show the appropriate absorption range and phonon frequencies for our experiment to study this strong coupling property. To observe the revolution of the zone center phonons, we have performed a long-time delay measurement at a relatively high power (see Fig. 3.17 (a)). From the STFT result shown in Fig. 3.17 (b), we can observe that the FFT amplitude is beating, i.e. collapses and revives and then collapses and revives again, similar to the Rabi oscillation[48] in the two-level system. Similar to the Bismuth case[34,57,58], we propose the strong coupling channels between zone center phonons with frequency ω_1 and two LA phonons with frequency ω_0 where ω_1 is the B_2 zone center mode (standing wave with long lifetime) in the quantum confined direction (out-of-plane) and $\omega_0 = {}^1\!/_2\,\omega_1$ is in unconfined directions (see Fig. 3.22). Compared to the Bi case[34], we have only observed the coherent zone center mode ω_1 except the resonant parametric modes ω_0 with large wavevector due to the detection mechanism in pump-probe experiment (Chapter 1.2.4), but our results show the coherent zone center mode ω_1 is in a stronger coupling region where there exists coherent energy transfer.

To understand more about this coherent energy transfer mechanism, we have conducted the power dependent CPS for the SL 8/8 and the results are shown in Fig. 3.18 (a) and the corresponding FFT results are shown in (b). The experimental details are covered in Chapter 2.3. We have subtracted the electron signal and a slowly decaying thermal background as well as the lowest coherent phonon at around 20 *GHz*. We have used the values for GaAs and AlAs[142] to modify the thickness of the SL 8/8 to be 9.62 *nm*/5.94 *nm* which deviates from our XRD thickness results too much.

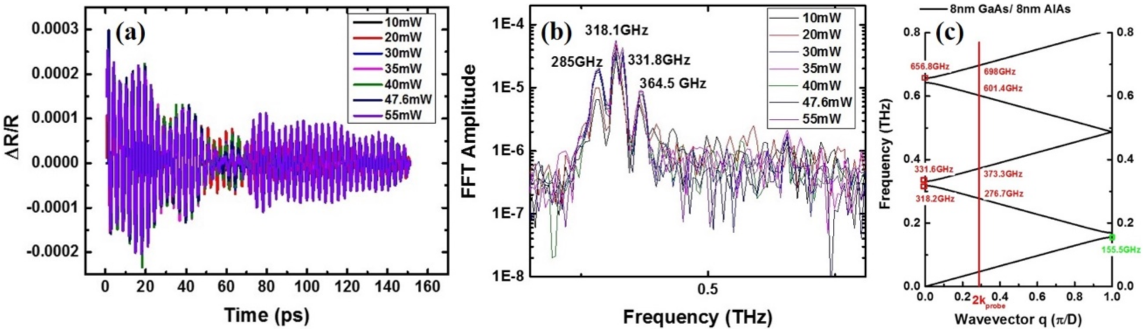

Figure 3.18 (a) Power-dependent CPS after extracting its electron signal and a slowly varying thermal background; (b) FFT results correspondingly; (c) the adjusted phonon dispersion curve.

We have applied STFT and chosen a Hanning window with a FFT length/ window length/ overlap to be 512/250/200 to analyze Fig. 3.18 (a) and the results (see Fig. 3.19 (a)) are displayed for 329.6 *GHz* (B_2 zone center mode). Since the size of the window is related to the time resolution and frequency resolution, i.e. the shorter the window, the higher the time resolution, but poor frequency resolution, and it's different than purely performing FFT, we have poor frequency resolution (12.2 *GHz*) than the FFT (6.63 *GHz*). The 329.6 GHz in Fig. 3.19 should correspond to 331.8 *GHz* in Fig. 4.18 (b).

From Fig. 3.19 (a), we can see at low powers, e.g. 10 *mW* and 20 *mW*, the FFT amplitude for 329.6 *GHz* is decaying with a decay constant (similar for these two powers) and we can barely see the quantum coherent coupling, while at higher powers, the FFT amplitudes will collapse first and revive again in a later delay time. By comparing 55 *mW* and 30*mW*, the FFT amplitude collapses earlier at a higher power (see Fig 3.17 (b)), 58 *ps* at 55 *mW* 69.6 *ps* at 30 *mW*, i.e. larger coupling constant/rate at higher power.

Another interesting phenomenon is the FFT amplitude seems to saturate and not linear with increasing power which is contradictory to the ISRS mechanism where the phonon amplitude should increase linearly with the incident intensity. In this way, we'll need to explain in the fashion of DECP mechanism.

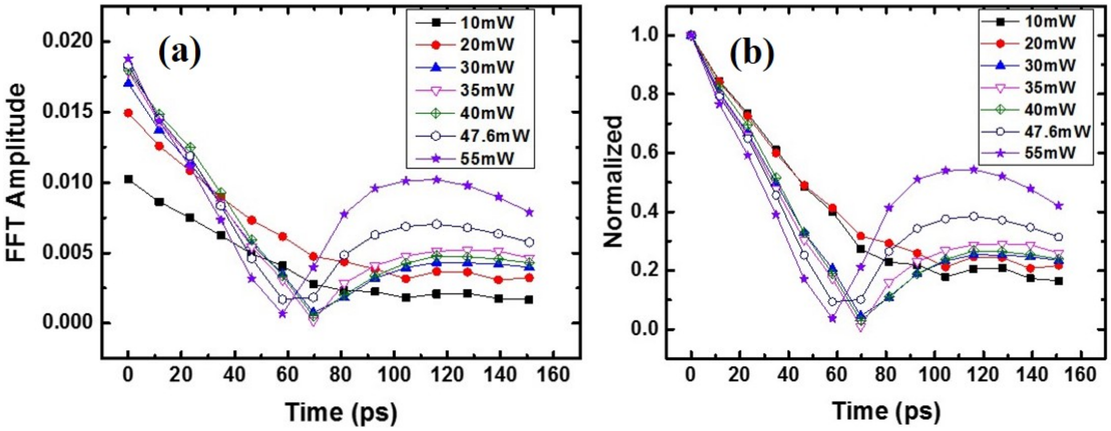

Figure 3.19 (a) STFT results for 329.6 *GHz*; (b) Normalized at first point in (a).

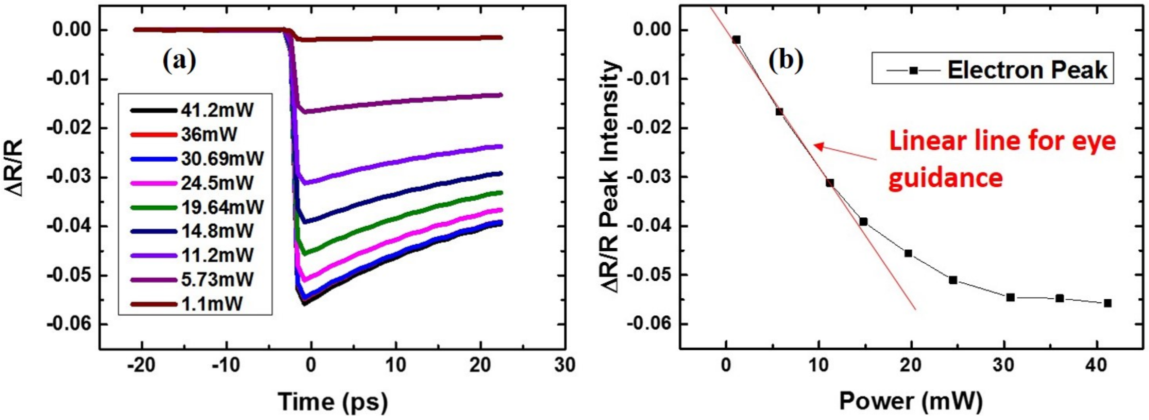

Figure 3.20 (a) Power-dependent electron signal; (b) Peak value vs. incident power (the red line is a linear line for eye guidance).

The electron signal is shown in Fig. 3.20 (a) and the peak values are plotted with power in (b). We can see the peak values are linearly increased with power under 15 mW, then starts to saturate at higher powers.

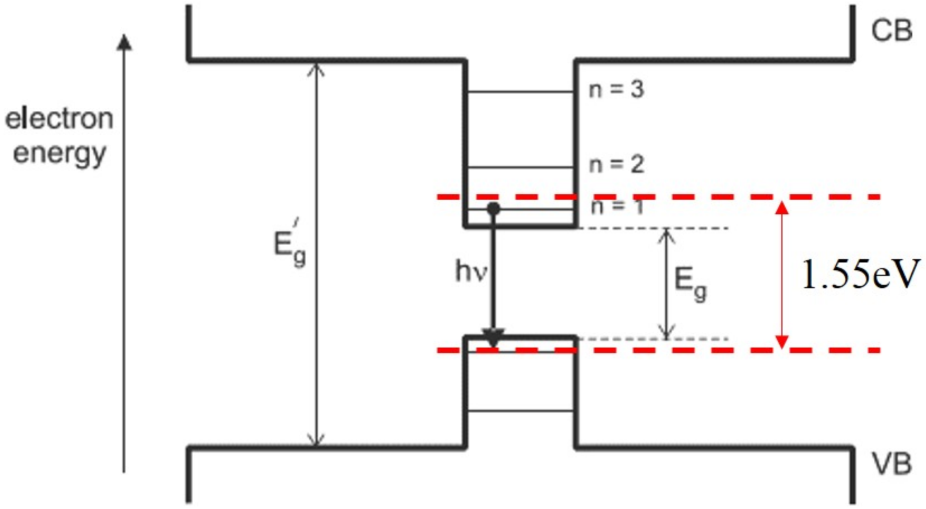

Figure 3.21 Schematic of simplified band structure of SL 8/8 where the smaller band gap E_g is for bulk GaAs (1.424 eV) and E_g' for bulk AlAs (3.03 eV). The $n = 1$ is the first quantized energy level for the SL which is around 1.5 eV. The 1.55 eV shown in the figure is our laser photon energy.

From the PL for SL 8/8 in Fig. 3.11 (a), we can see the energy gap is around $1.5eV$ and our pump photon energy ($1.55\ eV$) is slightly larger than it (see Fig. 4.21). The mechanism for light-matter interaction in the SL is the energy and coherence of photons will first transfer to the electrons and then the electrons will transfer the energy and coherence to the phonons in a short time (~hundreds of femtoseconds). SL first absorbs the incident photons and the excited electron population will increase linearly with photon number (incident power). Once the density of states (DOS) of electrons in the energy level $n = 1$ is fully occupied, no more photons can be absorbed, and the excited population of electrons saturates. Therefore, the energy transferred from electrons to phonons is also saturated.

Similar to the Bismuth case[34,57,58], we propose the strong coupling channels between the zone center phonon with frequency ω_1 and two LA phonons with frequency ω_0 where ω_1 is the B_2 zone center mode (standing wave with a long lifetime) in the quantum confined direction (out-of-plane) and $\omega_0 = {}^1\!/_2\,\omega_1$ is in unconfined directions (see Fig. 3.22). Compared to the Bi case[34], we have only observed the coherent zone center mode ω_1 except the resonant parametric modes ω_0 with large wavevector due to the detection mechanism in pump-probe experiment (Chapter 1.2.4), but our results show the coherent zone center mode ω_1 is in a stronger coupling region where there exists coherent energy transfer.

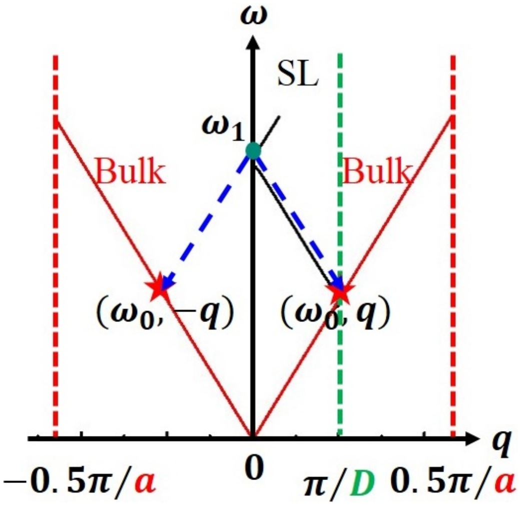

Figure 3.22 Phonon resonant parametric process proposed: zone center mode ω_1 in the SL coupled to two bulk acoustic modes with half the energy ω_0 and opposite wavevector $\pm q$ where *a* is the lattice constant and *D* is the period thickness for the SL.

The Hamiltonian of this system is

$$\begin{gathered}\mathcal{H} = \mathcal{H}_0 + \mathcal{H}_{int} \\ \mathcal{H}_0 = \hbar\omega_1\left(b_1^\dagger b_1 + \frac{1}{2}\right) \\ \mathcal{H}_{int} = \hbar\sum_q g_{01}\left(b_1 b_q^\dagger b_{-q}^\dagger + b_1^\dagger b_q b_{-q}\right)\end{gathered} \tag{3.2}$$

where $b_q^\dagger$ and b_q are the annihilation and creation operators for (ω_0, q) mode respectively and g_{01} is the coupling constant between $\omega_1$and ω_0. They can be written in terms of coordinate Q and momentum P as

$$\mathcal{H} = \frac{1}{2}(P_1^2 + \Omega^2 Q_1^2) + \frac{1}{2}(P_0^2 + \omega_0^2 Q_0^2) + g_{01} Q_1 Q_0^2 \tag{3.3}$$

Therefore, by using the Heisenberg equations of motion from Eq. (1.8), we can obtain

$$\ddot{Q}_1 + \gamma_1 \dot{Q}_1 + \omega_1^2 Q_1 = -g_{01} Q_0^2 + f(t) \tag{3.4}$$

$$\ddot{Q}_0 + \gamma_0 \dot{Q}_0 + \omega_0^2 Q_0 = -2g_{01} Q_1 Q_0 \tag{3.5}$$

where $f(t)$ is for the laser pulse field.

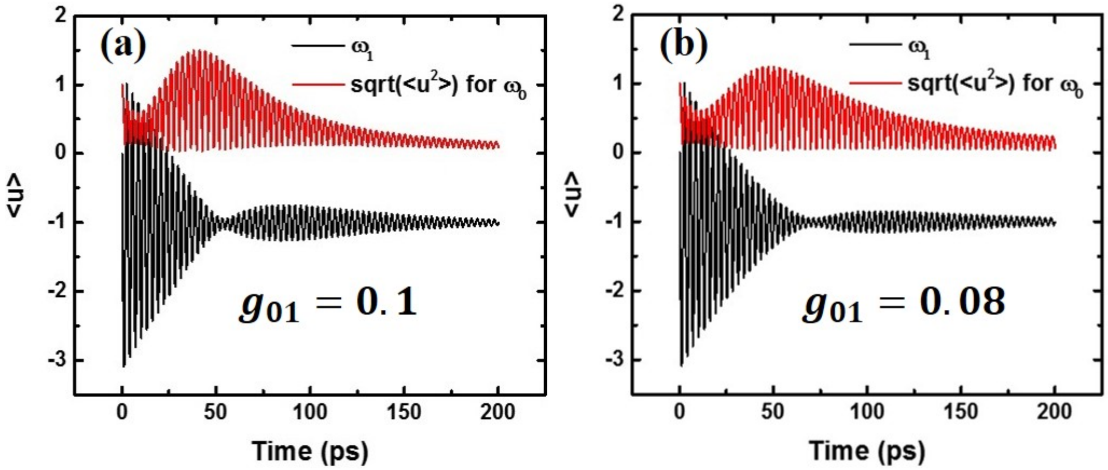

Figure 3.23 Simulation of mean displacement for ω_1 and ω_0 in the strong coupling region with the coupling constant to be $g_{01} = 0.1$ (a) and $g_{01} = 0.08$ (b).

By solving the coupled equations (3.4) and (3.5) simultaneously (see Appendix B) with parameters $\gamma_1 = 0.05\, ps^{-1}$ and $\gamma_0 = 0.0125\, ps^{-1}$ which are based on the theoretical three-phonon scattering trend yielding a $1/\omega^2$ frequency dependence[152], in addition with $g_{01} = 0.1$ and $g_{01} = 0.08$, we can produce the mean displacement of ω_1 and mean square displacement for ω_0. Figure 3.23 (a) & (b) plot the mean displacement of $\omega_1$and the square root of mean square displacement ω_0 in comparison. In comparison with Fig. 3.19, we can estimate the coupling constant is within the range in 0.08~0.1. Further detailed fitting processes are needed to determine the exact coupling constant.

3.3.3 Summary

In summary, we have used coherent phonon spectroscopy to study power-dependent coherent phonon dynamics in the GaAs/AlAs 8 *nm*/ 8 *nm* superlattice structure. The revolution of FFT amplitude of the B_2 zone center mode with a frequency of 329.6 *GHz* extracted from STFT method has shown a collapse and revival signature similar to the Rabi oscillation. We propose there is quantum coherent coupling and coherent heat transfer between ω_1 and ω_0 where the resonant parametric process happens. Our results suggest that it is possible to use SL structures to manipulate coherent phonon propagation in the nonlinear region to create the squeezed state. Future works would be: (i) reconstruct the mean displacement for 329.6 *GHz*; (ii) fit the experimental results of 329.6 *GHz* to get the real coupling constant; (iii) apply an X-ray diffuse scattering experiment to observe ω_0 along with ω_1.

Chapter 4: Surface Plasmon Enhanced Pump-probe Experiment

Surface plasmon resonance (SPR) has been widely used for gas detection and biosensing since last decade[158-163]. People are also trying to implement SPR into other spectroscopy[164-171] to enhance the signal to noise ratio and detect the optical properties of the materials[172-175], especially in the Raman scattering technique [176].

In this section, I will first briefly introduce the concept of SPR and the two common configurations with prism, the Kretschmann and Otto configuration, to generate SPR, then I will present how we prepare the samples for SPR and how we implement SPR into our pump-probe measurement along with some results we obtained.

4.1 SURFACE PLASMON RESONANCE

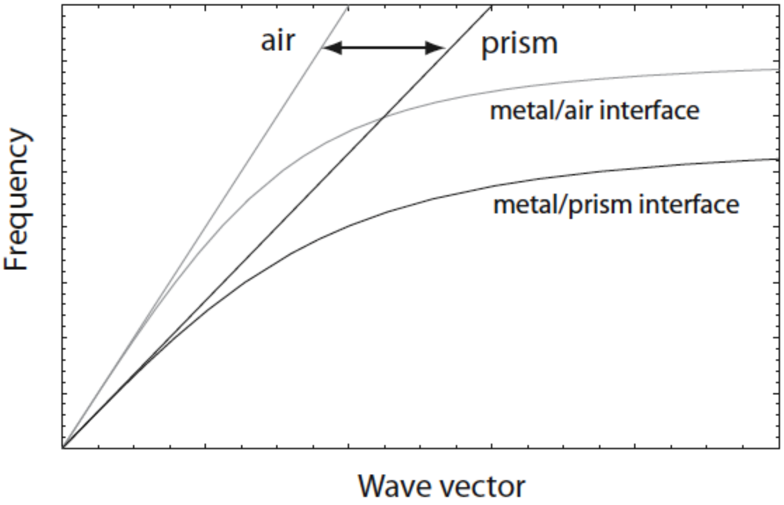

Figure 4.1 Prism coupling and Surface Plasmon Polariton (SPP) dispersion. Only in the cone between light line in air and in prism can the excited SPPs have propagation (Ref. 177).

Similar to the concept of phonons as quantized lattice vibrations, plasmons are quantized free electron oscillations. It is well known that light can be coupled with free electrons in a thin metal film. When the light wave vector matches that of free electron 'gas' or surface plasmon wave vector (phase matching condition[177]), resonance occurs (see Fig. 4.1).

To couple the light into the SP wave in thin metal film, it is necessary to use a prism or a grating. The most commonly used scheme is called attenuated total internal reflection, involving tunneling fields of excitation beam to the metal/air interface where the SPP excitation happens[177]. Two possible geometries for prism coupling are possible, one is the so-called Kretschmann configuration and the other Otto configuration (see Fig. 4.2).

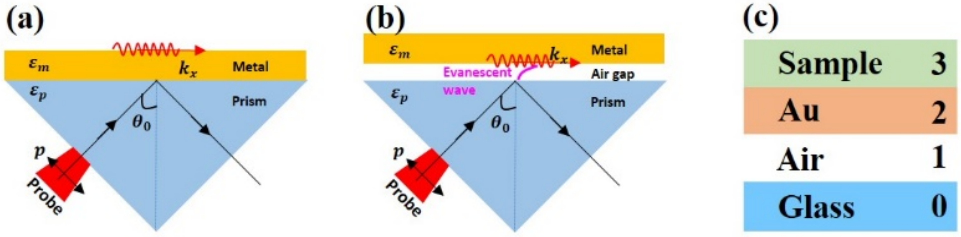

Figure 4.2 (a) Kretschmann configuration; (b) Otto configuration; (c) Simplified multilayer structure for Otto configuration.

The wave vector k_x of incident light should satisfy the condition of SPR excitation as follows[177]:

$$k_x = \sqrt{\varepsilon_P}\frac{\omega}{c}\sin\theta = k_{sp} = \frac{\omega}{c}\left|\frac{\varepsilon_m\varepsilon_\alpha}{\varepsilon_m + \varepsilon_\alpha}\right|^{1/2} \tag{4.1}$$

where ε_P, ε_m, ε_α are the dielectric constant of the prism, metal and detected materials, respectively. ω is the photon frequency of incident light, which is equal to $2\pi/\lambda$, λ is the wavelength of the incident light. θ is the incident angle and c is the light speed in vacuum. The incident angle or wavelength of the probe light can be tuned to satisfy the condition of SPR. To satisfy Eq. (4.1), the real part of the dielectric constant of the metal must be negative and its magnitude must be greater than that of the material under detection. This criterion can be satisfied at interfaces of noble metals (Au, Ag, Al) with common semiconductors.

As shown in Fig. 4.2 (a) & (b), when the incident angle of probe beam is close to the SP resonance, $dR/d\theta$ becomes very large and a small change of SP resonance angle will induce large reflectivity changes[165]. This character can be used to enhance the detection of coherent phonons. When coherent phonons travel into the region of the surface plasmon, the collective oscillation of atoms will modulate the local dielectric constant and slightly alter the resonance angle of the surface plasmon. Due to the large $dR/d\theta$, reflectivity change from coherent phonons can be greatly amplified. It is reported that the coherent phonon signals have been enhanced 10~100 times[166,167,169].

By using Fresnel's equations in a four-layer system (see Fig. 4.2c), the reflectance for the system is given as[173,178]

$$R_{0123} = \left| \frac{r_{01} + r_{123}\, exp(2ik_{z1}d_1)}{1 + r_{01}r_{123}\, exp(2ik_{z1}d_1)} \right|^2 \tag{4.2}$$

where

$$r_{123} = \frac{r_{12} + r_{23}\, exp(2ik_{z2}d_2)}{1 + r_{12}r_{23}\, exp(2ik_{z2}d_2)} \tag{4.3}$$

and

$$r_{ij} = \frac{\left(\frac{k_{zi}}{\varepsilon_i} - \frac{k_{zj}}{\varepsilon_j}\right)}{\left(\frac{k_{zi}}{\varepsilon_i} + \frac{k_{zj}}{\varepsilon_j}\right)},\ ij = 01,12,23 \tag{4.4}$$

and

$$k_{zi} = \frac{2\pi}{\lambda}\left(\varepsilon_i - \varepsilon_0 \sin^2\theta\right)^{1/2},\ i = 0,1,2,3 \tag{4.5}$$

Figure 4.3 shows the simulation obtained from the above equations when considering the air gap to be 1 μm, the gold layer to be 40 *nm* and three different thickness of our superlattice structures.

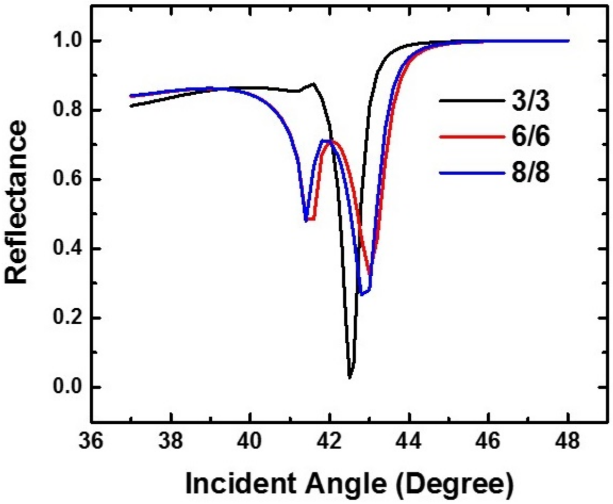

Figure 4.3 Simulation using Fresnel's equations in a four-layer system (see Fig. 4.2c).

As mentioned earlier, if coherent phonons are detected through the Stimulated Brillouin Light Scattering (SBLS) mechanism, only the phonons with wave vectors $k_{phonon} = 0 \sim 2k_{probe}$ can be detected. When using a probe beam to generate surface plasmon, the detected reflectivity change actually comes from the interference between the surface plasmon and coherent phonons. Phonon wave vectors are not constrained to the $0 \sim 2k_{probe}$, hence a broader band of CTPs can be detected. Recently, surface plasmon has been utilized to detect CTP in gold film up to $1THz$ [175].

4.1.1 Kretschmann Configuration

We have performed a pump-probe measurement in the Kretschmann configuration with 40nm Au thin film at four different incident angles. The reflectivity change with angle near the SPR angle where mark a is the SPR angle is shown in Fig. 4.4 (b). As shown in the inset of Fig. 4.4 (c), we generate coherent acoustic phonons by heating the front metal surface with a weakly focused pump beam and detect from the prism side with a p-polarized probe beam. The pump beam is ~10 times larger than the probe beam. Fig. 4.4(c) shows the differential reflectivity for four different incident angles. ΔR/R shows a sharp change immediately after time zero, which is due to the excitation of the hot electrons followed by electron-electron and electron-phonon coupling. The mark a gives the highest peak and mark b and c have almost the same height. After removing the electronic/thermal background, we'll see echo-like oscillations in Fig. 4.4 (d) for mark a and b. These oscillations are believed to be a pump induced round trip acoustic strain wave (1D standing wave)[169]. The calculated velocity of the acoustic phonons in our Au film is 3.16 *km/s* using $L = 40\ nm$ and $\tau = 25.3\ ps$ which agrees well with the sound velocity of 3.24 *km/s* in bulk gold[165].

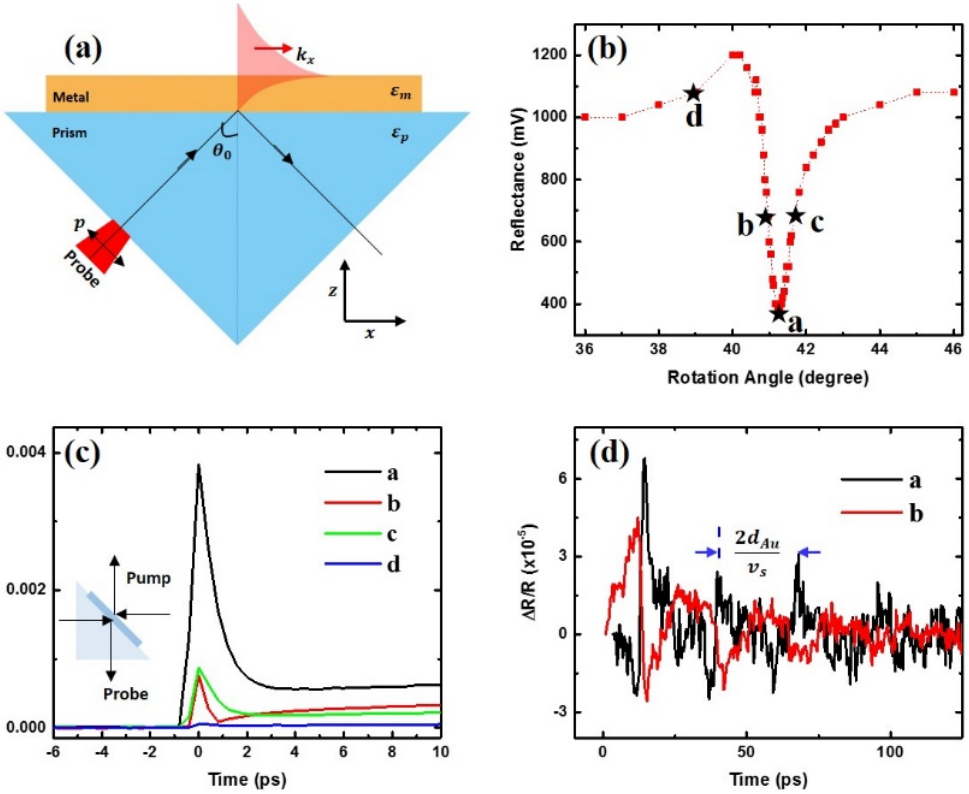

Figure 4.4 (a) Kretschmann configuration; (b) Reflectivity change with angle near SPR; (c) SPR embedded pump-probe differential reflectivity for a 40 *nm* Au film at four different incident angles; (d) Pure phonon signals after removing electronic/thermal background for position a & b.

4.1.2 Otto Configuration

The Kretschmann configuration, like Fig. 4.5 (a), is better for the pressure sensor and the semiconductor layer should be relatively thin, while the Otto configuration is better for the displacement sensor[163,179]. Our SLs have a range of 60-1200 *nm*, which will decrease the sensitivity too much for Kretschmann configuration. In this task, the Otto configuration (see Fig. 4.5 (b)) will be better to be implemented into our coherent phonon spectrometer to detect a broad band of CTPs with much higher sensitivity. The semiconductor samples will be grown with MBE and coated with a 40 *nm* Au thin film, then lifted off and transferred to an HF-etched BK7 glass slide. The BK7 glass slide will be attached to a BK7 prism with a refractive-index matching glue (NOA 65). The whole block (sample/metal film/ BK7 glass slide /prism) will finally be mounted on a rotary stage with high resolution to control the incident angle. The pump beam will illuminate the sample from the top to launch the CTPs, which will travel to the sample/metal film interface and interfere with surface plasmon generated by probe beam. Reflectivity change caused by CTPs will be recorded and analyzed.

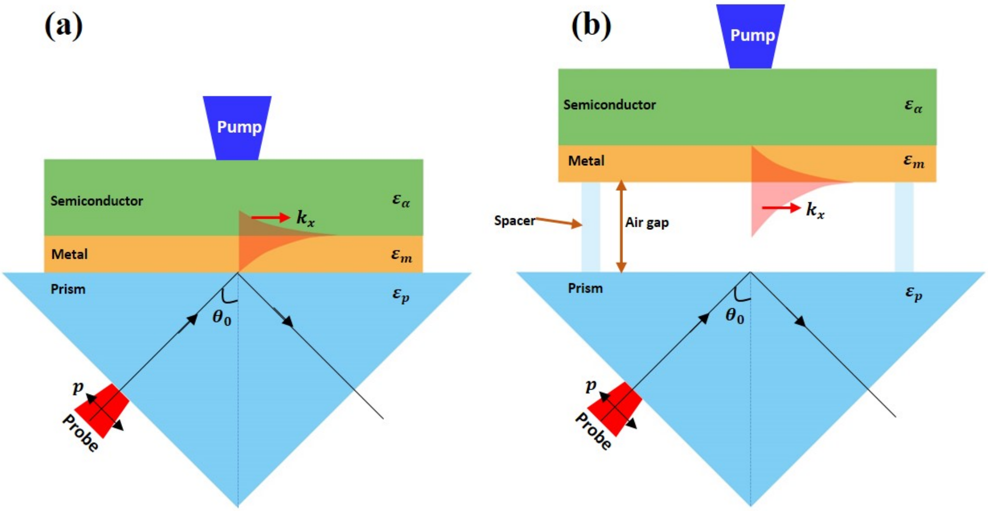

Figure 4.5 (a) Kretschmann configuration with the red shallow area between metal and semiconductor as the SPP; (b) Otto configuration with the red shallow area between metal and air as the SPP.

4.2 SAMPLE PREPARATION

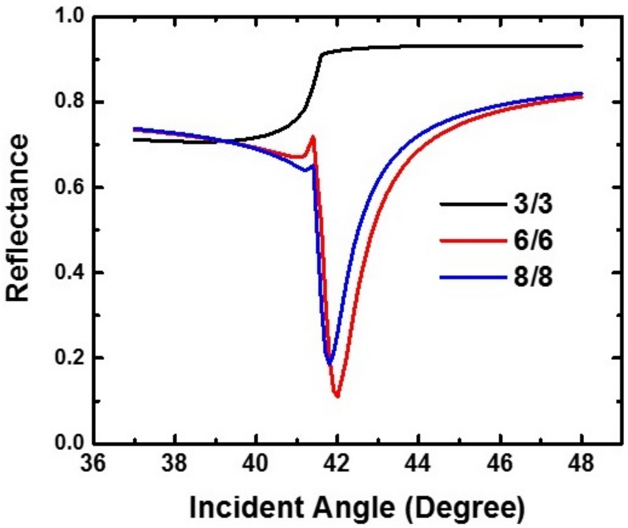

Figure 4.6 Simulation of reflectance vs. incident angle for Kretschmann device with a 25*nm* Au film.

Since the air gap size in the Otto configuration is not easy to control, we've tried both HF etching on the BK7 glass slide and photo-lithography on SU-8 but both give us a bad angle dependent reflection signal which we will attribute to the real air gap size is large due to roughness.

According to our simulation (see Fig. 4.6), we've tried to make the Kretschmann device using thinner SL structures, like 3 *nm*/3 *nm*, 6 *nm*/6 *nm* and 8 *nm*/8 *nm* (short for 3/3, 6/6/, 8/8) with 30 periods. From the simulation, we've tried to use a 25 *nm* Au film as the metal layer. The following shows the process (see Fig. 4.7).

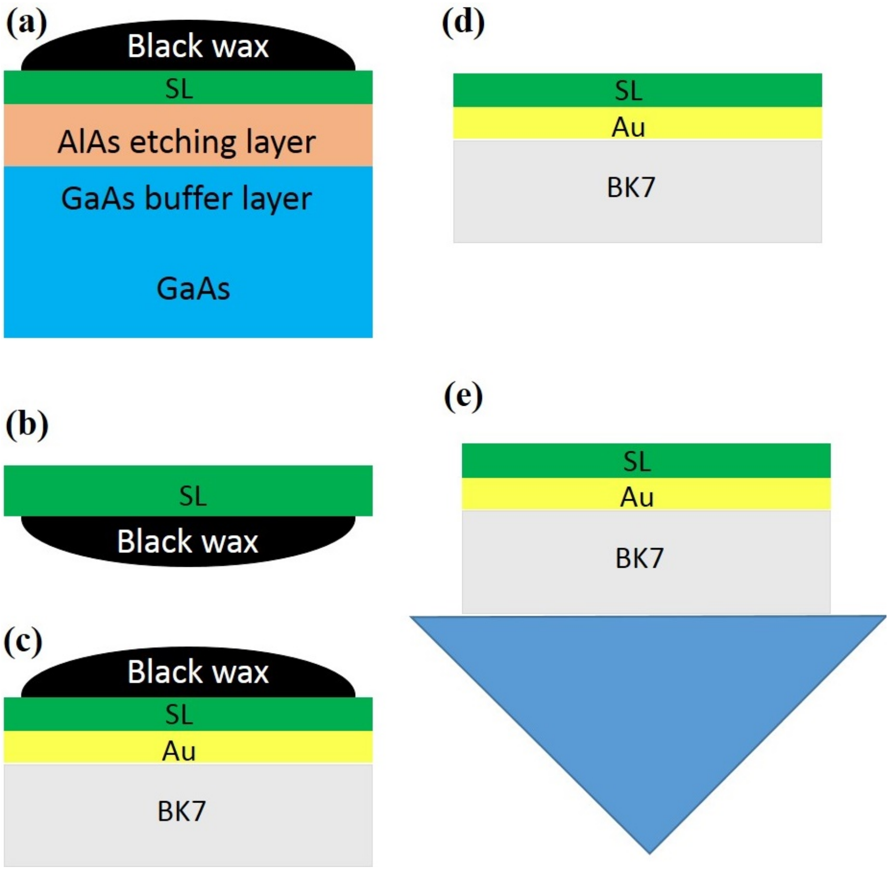

Figure 4.7 Process of making the Kretschmann device: (a) apply black wax on the sample; (b) etch away the AlAs etching layer; (c) lift the membrane with Au deposited glass; (d) dissolve the black wax; (e) use an optical index matching glue to attach the glass on the prism.

We first cleave the MBE grown sample into 65 *mm* × 65 *mm* pieces, then apply a small piece of black wax (Apiezon W) onto the cleaved sample, followed with heating at 150°C for around 30 minutes. After the black wax has formed a nice dome shape on the sample, it is cooled down for 5 minutes until the wax hardens, and then we can use Xylene and swab to clean the sides and bottom until no more wax is on the sides under microscope, so the etching layer can be etched (see Fig. 4.8 (c)).

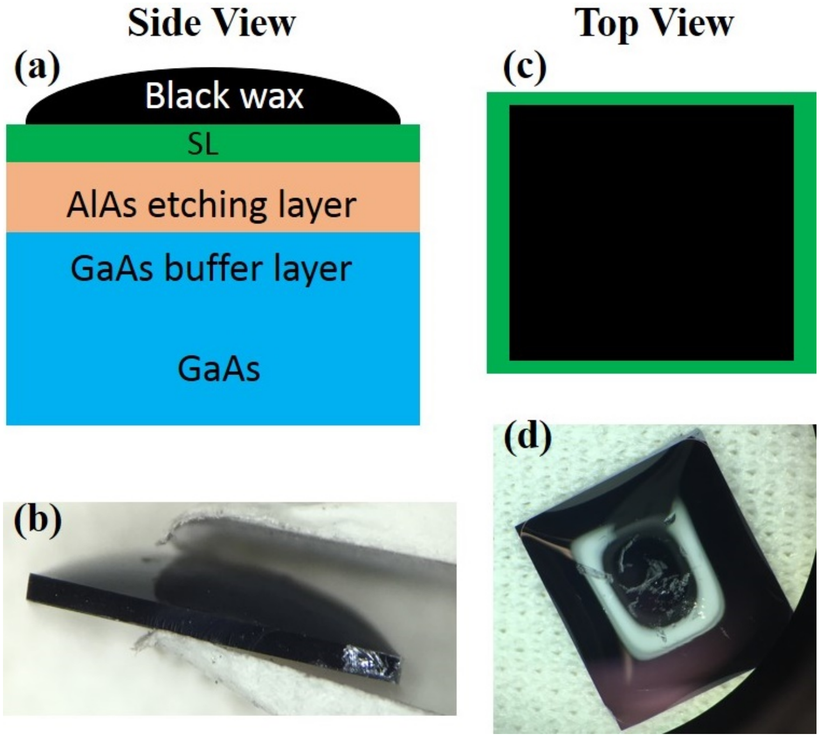

Figure 4.8 Side view and top view of the sample after applying the black wax. (a) and (c) are the scheme; (b) and (d) are for real sample.

After that, we can setup the acid bench to release the epitaxial membrane from the substrate. It usually takes 5-6 hours to finish etching. While we setup the acid bench, we can put a dipper in the bench, and put the samples with wax side up into the dipper. Then we can carefully pour HF (49%) into the HF beaker. Ideally, after the etch is complete, the wax layer with the membrane will float to the surface and we can handle it carefully with tweezers. Usually, we will need to jigger the dipper into the acid gently and then the membrane will release and float if the etch is done. Once the membrane is released, prepare the the Rinse beaker with water about 6-10 *mm* from the brim and the dipper is carefully moved from the Etch beaker to the Rinse beaker, capturing the membrane in the dipper and letting it float on the Rinse water. After a minute use tweezers to take the membrane out, dunk it 3 times, and put it on wipes. We then flip it over and over to make sure the wipes absorb-dry the sample and use a very light N_2 spray on each side if needed. Once the sample is dry, we then pipette a droplet on a clean gold-coated BK7 glass slide onto which we have used e-beam deposition to deposit a 25 *nm* gold layer, and use tweezers gently press the membrane/wax with the wax side up on the droplet and use paper kimwipes to absorb the excess water. After 30 minutes' waiting for the van der Waals force to form between the membrane and the gold film, we can pour Trichloroethylene in the beaker and sink the whole piece into the solvent. After about 20 minutes, the wax will be dissolved, and we can put the membrane/glass into acetone and rinse. For better bonding, we will leave the glass slide in the hood for 24 hours. To make the SPR device, we will use index-matching optical glue (NOA 65) to attach glass on the prism and expose it under UV light for 1 minute. Figure 4.9 shows the SPR device.

Figure 4.9 (a) and (b) are real Kretschmann devices with the 6/6 and 8/8 SL on top of 25 *nm* Au film. We can see from the center to the edge of the SL, the color is different. This could be different thicknesses of the transferred film. A hemicylindrical prism will help to probe at the same spot on the sample when rotating the stage. From the PL in Fig. 4.9 (c), the transferred 8/8 SL on glass (red line) shows a red shift compared with the As-grown 8/8 SL (black line) which can be attributed to the relaxed stress from the substrate.

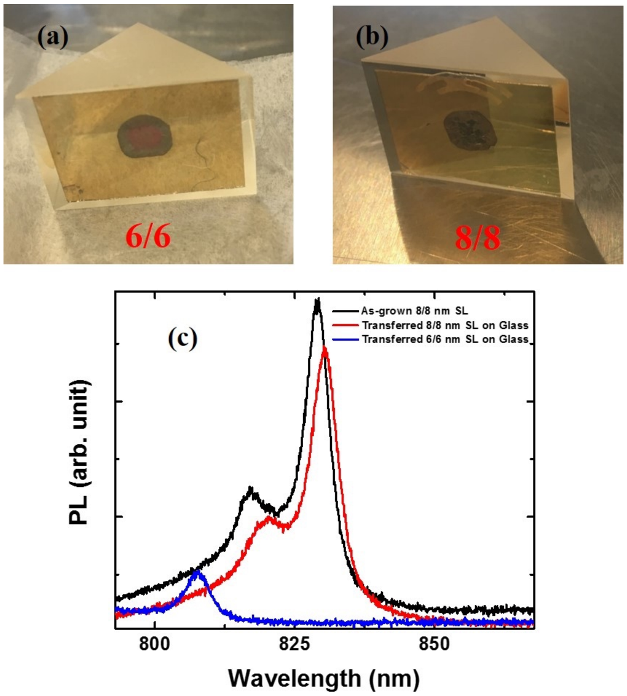

Figure 4.9 Real samples and PL: (a) and (b) are the pictures of the real Kretschmann devices with 6/6 and 8/8 SL respectively; (c) is the PL for transferred 6/6 and 8/8 SL on glass and also the As-grown 8/8 SL. The black line is for the As-grown 8/8 SL, the red line is for the transferred 8/8 SL on glass and the blue line is for the transferred 6/6 SL on glass.

From Fig. 4.10 (a) and (c), we can see the Kretschmann device with the SL 3/3 and SL 6/6 under the microscope respectively. The color in (a) is yellow which is basically coming from the Au film under the SL 3/3 since the SL 3/3 is too thin, and the color in (c) is pink which is from the SL 6/6. The Low cut-off Raman scattering spectrum for the Kretschmann device with SL 3/3 and SL 6/6 are shown in (b) and (d) respectively along with their As-grown samples as a comparison. We can see that the doublets feature smears out in Fig. 4.10 (b) while staying the same in Fig. 4.10 (d). The disappearance of the doublets feature is coming from the scattering of phonons by the electrons in the Au film which broadens the Raman peaks and the resolution of our Low cut-off Raman apparatus cannot resolve it.

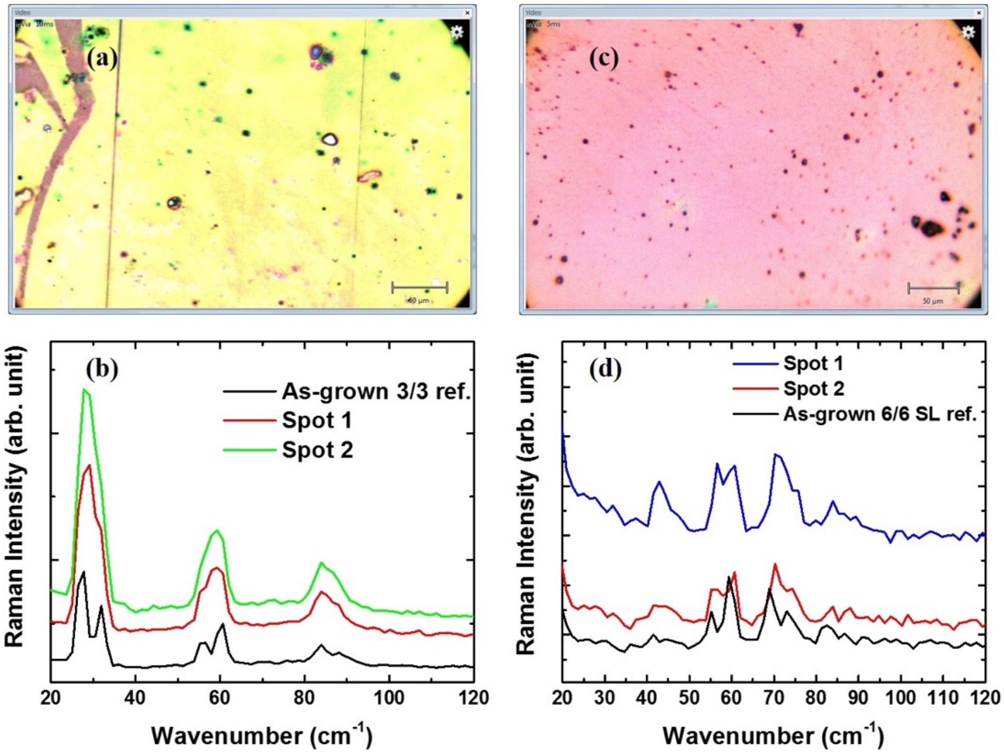

Figure 4.10 (a) and (b) are the 3/3 Kretschmann device under microscope (the scale bar is 60 μm) and the Low-cut Raman scattering of it respectively; (c) and (d) are the 6/6 Kretschmann device under the microscope (the scale bar is 50 μm) and the Low-cut Raman scattering of it respectively.

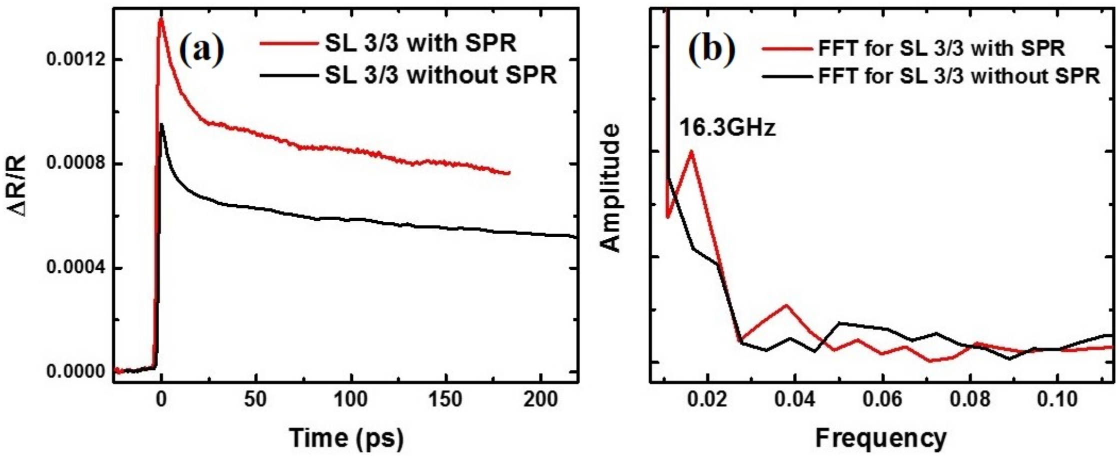

Figure 4.11 (a) CPS results for the SL 3/3 with and without SPR enhancement; (b) FFT results for (a).

In order to observe the enhancement of the SPR in the CPS technique, we have measured both the Kretschmann device with the SL 3/3 and the SL 3/3 membrane directly using the CPS under the same experimental condition (see Fig. 4.11). In comparison with the SL 3/3 without SPR, we can see the electron signal (the peak) with SPR is enhanced, in addition, the coherent phonon with frequency around 16.3 *GHz* is amplified.

4.3 EXPERIMENTAL SETUP

The SPR implemented pump-probe setup (see Fig. 4.5) will be similar to our CPS with amplifier system, except around the sample region, we have pump and probe pulse hitting on the sample from opposite directions (Front-back configuration). The main difficulty in this configuration is to overlap the pump and probe pulse. Usually we will start from 45 degrees which will make sure the probe is normal incident to one of the legs in right-angle prism, then we will find the signal at this angle and set the time delay at the large signal point, afterwards, we will rotate the stage slowly and tune the pump to maximize the signal. In this setup, a hemi-cylindrical prism will be better.

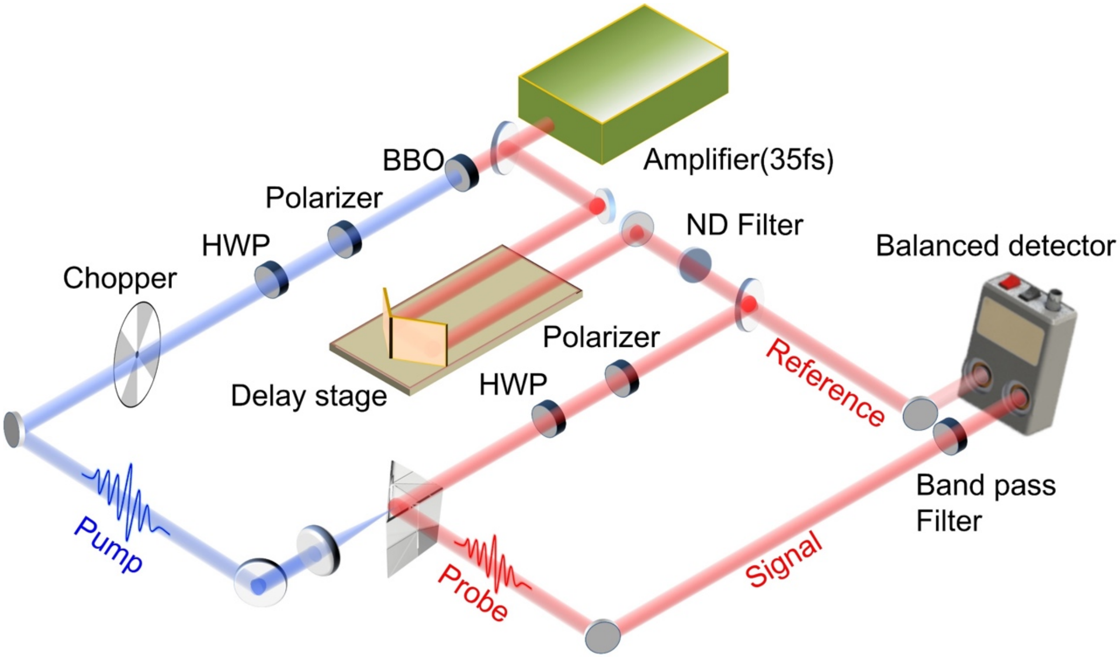

Figure 4.12 SPR imbedded system: the enlarged sample position will be like Fig. 4.5. The prism will be put on a rotational stage.

Chapter 5: Outlook

In this thesis, I've presented three time-resolved pump-probe studies of coherent phonons generated in semiconductors. The first experiment was performed using two-color ultrashort laser to study the thermal reversible melting mechanism by measuring the coherent phonon dynamics with a variety of pump fluences in bulk CdSe. A complete phase transformation in bulk CdSe may be reached when the absorbed laser energy can be localized for long enough time, as observed in nanocrystalline CdSe. In the second experiment, phonon lifetimes have been extracted by exponential fitting of the decaying STFT amplitudes of the coherent phonons in the Bi_2Te_3/Sb_2Te_3 superlattice. In comparison with bulk Bi_2Te_3, the spectrum of mode-wise thermal conductivities of longitudinal acoustic phonons along the Γ-Z direction in the SL shows a shift to higher frequencies. Our results suggest that it is possible to use the SL structure to manipulate coherent phonon propagation and to tailor thermal conductivity. In the third experiment, I have used coherent phonon spectroscopy to study power-dependent coherent phonon dynamics in the GaAs/AlAs 8 *nm*/ 8 *nm* superlattice structure. A clear collapse and revival trend in the FFT amplitude of the zone center mode has been revealed and quantum coherent coupling and coherent heat transfer between ω_1 and ω_0, where the resonant parametric process happens, is proposed. Our results suggest that it is possible to use SL structures to manipulate coherent phonon propagation in the nonlinear region to create the squeezed state. We also developed an experimental scheme with the implementation of surface plasmon resonance to enhance the signal to noise ratio to shorten the measuring time.

Furthermore, we demonstrate that our SPR enhanced technique is applicable to enhance the coherent phonon signal. This opens a new avenue which will be explored in the near future. For the strong coupling study in SLs, we can explore more: (i) fit the experimental results of 329.6 *GHz* to get the real coupling constant; (ii) apply the X-ray diffuse scattering experiment to observe ω_0 along with ω_1; (iii) design a microcavity to investigate the enhancement of the strong coupling; (iv) manipulate the coupling constant with different period thickness; and (v) prepare the squeezed state in the superlattice.

Appendices

A. PERTURBATION IN DISPERSION

An exact solution of the Schrodinger equation exists only for a few idealized problems; normally it has to be solved using an approximation method. Perturbation theory is applied to those cases in which the real system can be described by a small change in an easily solvable, idealized system. Hamiltonian of the system can be generalized as

$$\hat{H} = \hat{H}_0 + \hat{H}' \tag{A1}$$

where $\hat{H}_0$ is the for the unperturbed system and $\hat{H}'$ is the perturbation Hamiltonian which should be significantly smaller than $\hat{H}_0$. By applying continuity condition and periodicity condition[72], we get

$$cos(qD) = cos\left(\frac{\omega d_A}{v_A}\right) cos\left(\frac{\omega d_B}{v_B}\right) - \frac{1+\delta^2}{\delta} sin\left(\frac{\omega d_A}{v_A}\right) sin\left(\frac{\omega d_B}{v_B}\right) \tag{A2}$$

where $\delta = \rho_A v_A / \rho_B v_B$, since $cos(qD) \in [-1, 1]$, we can re-arrange Eq. in a perturbed form

$$cos(qD) = cos\left[\omega\left(\frac{d_A}{v_A} + \frac{d_B}{v_B}\right)\right] - \gamma\, sin\left(\frac{\omega d_A}{v_A}\right) sin\left(\frac{\omega d_B}{v_B}\right) \tag{A3}$$

where $\gamma = \frac{(1-\delta)^2}{2\delta}$ and we can treat $\gamma \sin\left(\frac{\omega d_A}{v_A}\right) \sin\left(\frac{\omega d_B}{v_B}\right)$ as small perturbation.

At m-th order Bragg scattering,

$$q = m\pi/D = q_m \tag{A4}$$

$$\omega = \omega_m + \Delta\omega_m/2 \tag{A5}$$

$$cos\left[\omega_m\left(\frac{d_A}{v_A}+\frac{d_B}{v_B}\right)\right]=(-1)^m \tag{A6}$$

where $\Delta\omega_m$ is the energy gap and satisfies $\Delta\omega_m/\omega_m \ll 1$. Therefore, for normal incidence and $\delta \approx 1$,

$$\omega_m = m\pi/\left(\frac{d_A}{v_A}+\frac{d_B}{v_B}\right) \tag{A7}$$

With Taylor expansion,

$$f(x)=f(a)+f'(a)(x-a)+\frac{f''(a)}{2!}(x-a)^2 \tag{A8}$$

Let $a=\omega_m$ and $\mathrm{x}=\omega$, and substitute $f(x)=cos\left[\omega\left(\frac{d_A}{v_A}+\frac{d_B}{v_B}\right)\right]$,

$$\begin{aligned} cos\left[\omega_m\left(\frac{d_A}{v_A}+\frac{d_B}{v_B}\right)\right] \\ &= cos\left[\omega_m\left(\frac{d_A}{v_A}+\frac{d_B}{v_B}\right)\right] \\ &-\frac{\Delta\omega_m}{2}\left(\frac{d_A}{v_A}+\frac{d_B}{v_B}\right)sin\left[\omega_m\left(\frac{d_A}{v_A}+\frac{d_B}{v_B}\right)\right] \\ &-\frac{cos\,\omega_m\left(\frac{d_A}{v_A}+\frac{d_B}{v_B}\right)}{2}\left(\frac{\Delta\omega_m}{2}\right)^2\left(\frac{d_A}{v_A}+\frac{d_B}{v_B}\right)^2 \end{aligned} \tag{A9}$$

Since $sin\left[\omega_m\left(\frac{d_A}{v_A}+\frac{d_B}{v_B}\right)\right]=0$, finally we can reduce Eq. (A3) to

$$\begin{aligned}(-1)^m = (-1)^m - \frac{cos\,\omega_m\left(\frac{d_A}{v_A}+\frac{d_B}{v_B}\right)}{2}\left(\frac{\Delta\omega_m}{2}\right)^2\left(\frac{d_A}{v_A}+\frac{d_B}{v_B}\right)^2 \\ -\gamma\, sin\left(\frac{\omega_m d_A}{v_A}\right)sin\left(\frac{\omega_m d_B}{v_B}\right)\end{aligned} \tag{A10}$$

And the energy gap is

$$\Delta\omega_m = \frac{2}{\left(\frac{d_A}{v_A} + \frac{d_B}{v_B}\right)} (2\gamma)^{1/2} \left| sin\left(\frac{\omega_m d_A}{v_A}\right) sin\left(\frac{\omega_m d_B}{v_B}\right) \right|^{1/2} \quad \text{(A11)}$$

B. MATLAB CODE FOR SOLVING COUPLED EQUATIONS

```
%% Analytic Solution


% oscillator parameters and coupling
om2 = 2*pi*0.33;   % optical mode
om1 = om2/2; % acoustc modes, at resonance

gam1 = 0.00;
gam2= 0.05;
g = 0.2;

% number of steps and temperature
numsteps=2000;
kT=0.0;  % units?!

%initial conditions
x1=0;
v1=0.0;
x2=1;
v2=0;
t1=0;
t2=200;

gau = @(x) -exp(-(x).^2/0.02)/0.021;
Fext = gau(linspace(t1, t2, numsteps));   % zeros(1,numsteps);
% Fext = zeros(1,numsteps);

% run a single mode
[X,F]=coupled_modes(om1, om2, gam1, gam2, g, [x1, v1, x2, v2], kT,
Fext, t1, t2, numsteps);

delays = linspace(t1, t2, numsteps);
figure(1); clf(); hold all
plot(delays,X(:,3),'b')
plot(delays,X(:,1),'r')
plot(delays, Fext/30, 'g')
xlim([0, 200])
ylim([-1.2, 1.2])


%% ensemble of N particles
N=5e3;

x1_0 = 1*randn(N,1);
v1_0 = 0.1*randn(N,1)*om1;

x2_0 = 1*ones(N,1);
v2_0 = zeros(size(x2_0));
```

```
Xtot = zeros(N, numsteps, 4);

% do an equilibration run first
for j=1:N
    [X,F]=coupled_modes_SWT(om1, om2, gam1, 0, g, [x1_0(j), v1_0(j),
x2_0(j), v2_0(j)],...
        kT, 0*Fext, t1, t2, numsteps);
    Xtot(j,:,:) = X;
end
%
for j=1:N
    [X,F]=coupled_modes_SWT(om1, om2, gam1, gam2, g, [x1_0(j), v1_0(j),
x2_0(j), v2_0(j)],...
        kT, Fext, t1, t2, numsteps);
    Xtot(j,:,:) = X;
end

%% plot distribution in phase space

figure(2);  axis equal
xmin=min(min(Xtot(:,:,1)));
xmax=max(max(Xtot(:,:,1)));
ymin=min(min(Xtot(:,:,2)/om1));
ymax=max(max(Xtot(:,:,2)/om1));

for j=1:10:numsteps
%%
%     j=1e4;
%     plot(w0*Q0(:,j),P0(:,j),'.');
    plot(Xtot(:,j,1), Xtot(:,j,2)/om1,'.b')
    hold on;
    plot(Xtot(:,j,3), Xtot(:,j,4)/om2,'.r')
%         plot(10*f(j),0,'og');1
    xlim([xmin xmax]); ylim([ymin ymax]); hold off; drawnow;
%     pause(.1);
end

%%
figure(3); clf
hold all
plot(delays,mean(Xtot(:,:,3),1)-mean(Xtot(:,1,3),1),'b')
% plot(delays,var(Xtot(:,:,3),1)/var(x2_0)-1,'g')
% plot(delays,mean(Xtot(:,:,1),1)-mean(Xtot(:,1,1),1),'b')
plot(delays,var(Xtot(:,:,1),1)/var(x1_0)-1,'r') % plot DII
xlim([0 200])
xlabel('time (ps)');
ylabel('<Q>')
set(gcf,'units','inches');
```

Coupled mode

```
function [X, F] = coupled_modes(om1, om2, gam1, gam2, g, xinit, kT,
Fext, t1, t2, numsteps)


%% parametrically driven oscillators
%
dt =(t2-t1)/numsteps;
F = sqrt(2/dt*gam1*kT)*randn(numsteps,1);

% X0 = [x1, v1, x2, v2];
X = zeros(numsteps, 4);
X(1,:) = xinit;
x1 = xinit(1);
v1 = xinit(2);
x2 = xinit(3);
v2 = xinit(4);



for i=2:numsteps
    x1 = x1+v1*dt;
    x2 = x2+v2*dt;
    v1 = v1 - gam1*v1*dt -om1^2*x1*dt + g*x1*x2*dt;
    v2 = v2 - gam2*v2*dt -om2^2*x2*dt + g*x1*x1*dt + F(i)*dt +
Fext(i)*dt;
    X(i,:) = [x1, v1, x2, v2];
end
1;
```

Coupled mode_SWT

```
function [X, F] = coupled_modes(om1, om2, gam1, gam2, g, xinit, kT,
Fext, t1, t2, numsteps)

%% parametrically driven oscillators
%

dt =(t2-t1)/numsteps;

% X0 = [x1, v1, x2, v2];
X = zeros(numsteps, 4);
X(1,:) = xinit;
x1 = xinit(1);
v1 = xinit(2);
x2 = xinit(3);
v2 = xinit(4);

% simple euler's method diff. eq.
```

```
for i=2:numsteps
    x1 = x1+v1*dt;
    x2 = x2+v2*dt;
    v1 = v1 - gam1*v1*dt -om1^2*x1*dt -2*g*x2*x1*dt; % re-factor
    v2 = v2 - gam2*v2*dt -om2^2*x2*dt -g*x1*x1*dt + Fext(i)*dt;
    X(i,:) = [x1, v1, x2, v2];
%     plot(x1, v2/om1,'.b')
%     hold on
%     plot(x2, v2/om2,'.r')
%     hold off
end
% 1;
F = [];
```

Bibliography

1 Forst, M., Mankowsky, R. & Cavalleri, A. Mode-selective control of the crystal lattice. *Acc. Chem. Res.* **48**, 380-387 (2015).

2 Först, M. *et al.* Nonlinear phononics as an ultrafast route to lattice control. *Nature Physics* **7**, 854 (2011).

3 Buzzi, M., Först, M., Mankowsky, R. & Cavalleri, A. Probing dynamics in quantum materials with femtosecond x-rays. *Nature Reviews Materials*, 1 (2018).

4 Juraschek, D. M. & Spaldin, N. A. Sounding out optical phonons. *Science* **357**, 873-874 (2017).

5 Nicoletti, D. & Cavalleri, A. Nonlinear light–matter interaction at terahertz frequencies. *Advances in Optics and Photonics* **8**, 401-464 (2016).

6 Mitrano, M. *et al.* Possible light-induced superconductivity in K_3C_{60} at high temperature. *Nature* **530**, 461 (2016).

7 Mankowsky, R. *et al.* Nonlinear lattice dynamics as a basis for enhanced superconductivity in $YBa_2Cu_3O_{6.5}$. *Nature* **516**, 71 (2014).

8 Nova, T. F. *et al.* An effective magnetic field from optically driven phonons. *Nature Physics* **13**, 132 (2017).

9 Shen, Y. R. & Bloembergen, N. Theory of stimulated Brillouin and Raman scattering. *Phys. Rev.* **137**, A1787 (1965).

10 Alfano, R. & Shapiro, S. Optical phonon lifetime measured directly with picosecond pulses. *Phys. Rev. Lett.* **26**, 1247 (1971).

11 Von der Linde, D., Laubereau, A. & Kaiser, W. Molecular vibrations in liquids: direct measurement of the molecular dephasing time; determination of the shape of picosecond light pulses. *Phys. Rev. Lett.* **26**, 954 (1971).

12 Zeiger, H. *et al.* Theory for displacive excitation of coherent phonons. *Phys. Rev. B* **45**, 768 (1992).

13 Cheng, T. *et al*. Impulsive excitation of coherent phonons observed in reflection in bismuth and antimony. *Appl. Phys. Lett.* **57**, 1004-1006 (1990).

14 Stevens, T., Kuhl, J. & Merlin, R. Coherent phonon generation and the two stimulated Raman tensors. *Phys. Rev. B* **65**, 144304 (2002).

15 Garrett, G. A., Albrecht, T., Whitaker, J. & Merlin, R. Coherent THz phonons driven by light pulses and the Sb problem: what is the mechanism? *Phys. Rev. Lett.* **77**, 3661 (1996).

16 Merlin, R. Generating coherent THz phonons with light pulses. *Solid State Commun.* **102**, 207-220 (1997).

17 Kittel, C., McEuen, P. & McEuen, P. *Introduction to solid state physics*. Vol. 8 (Wiley New York, 1996).

18 Wen, Y.-C. *et al*. Specular scattering probability of acoustic phonons in atomically flat interfaces. *Phys. Rev. Lett.* **103**, 264301 (2009).

19 Garrett, G., Rojo, A., Sood, A., Whitaker, J. & Merlin, R. Vacuum squeezing of solids: macroscopic quantum states driven by light pulses. *Science* **275**, 1638-1640 (1997).

20 Hu, J., Misochko, O. V. & Nakamura, K. G. Direct observation of two-phonon bound states in ZnTe. *Phys. Rev. B* **84**, 224304 (2011).

21 Wu, W., He, F. & Wang, Y. Reversible ultrafast melting in bulk CdSe. *J. Appl. Phys.* **119**, 055701 (2016).

22 Ma, W., Miao, T., Zhang, X., Kohno, M. & Takata, Y. Comprehensive study of thermal transport and coherent acoustic-phonon wave propagation in thin metal film–substrate by applying picosecond laser pump–probe method. *The Journal of Physical Chemistry C* **119**, 5152-5159 (2015).

23 Ruello, P. & Gusev, V. E. Physical mechanisms of coherent acoustic phonons generation by ultrafast laser action. *Ultrasonics* **56**, 21-35 (2015).

24 Huynh, A., Perrin, B. & Lemaître, A. Semiconductor superlattices: A tool for terahertz acoustics. *Ultrasonics* **56**, 66-79, (2015).

25 Legrand, R., Huynh, A., Vincent, S., Perrin, B. & Lemaître, A. Device for acoustic pulse echo experiments in the subterahertz range. *Phys. Rev. B* **95**, 014304 (2017).

26 Pascual-Winter, M., Fainstein, A., Jusserand, B., Perrin, B. & Lemaître, A. Spectral responses of phonon optical generation and detection in superlattices. *Phys. Rev. B* **85**, 235443 (2012).

27 Mizoguchi, K., Takeuchi, H., Hino, T. & Nakayama, M. Finite-size effects on coherent folded acoustic phonons in GaAs/AlAs superlattices. *Journal of Physics: Condensed Matter* **14**, L103 (2002).

28 Bartels, A., Dekorsy, T., Kurz, H. & Köhler, K. Coherent zone-folded longitudinal acoustic phonons in semiconductor superlattices: excitation and detection. *Phys. Rev. Lett.* **82**, 1044 (1999).

29 Li, W. *et al.* Coherent acoustic phonons in $YBa_2Cu_3O_7/La_{1/3}Ca_{2/3}MnO_3$ superlattices. *Appl. Phys. Lett.* **108**, 132601 (2016).

30 Wen, Y.-C. *et al.* Efficient generation of coherent acoustic phonons in (111) InGaAs/GaAs multiple quantum wells through piezoelectric effects. *Appl. Phys. Lett.* **90**, 172102 (2007).

31 Winter, M. P., Fainstein, A., Jusserand, B., Perrin, B. & Lemaître, A. Optimized optical generation and detection of superlattice acoustic phonons. *Appl. Phys. Lett.* **94**, 103103 (2009).

32 Misochko, O., Hase, M., Ishioka, K. & Kitajima, M. Observation of an amplitude collapse and revival of chirped coherent phonons in bismuth. *Phys. Rev. Lett.* **92**, 197401 (2004).

33 He, F., Wu, W. & Wang, Y. Direct measurement of coherent thermal phonons in Bi_2Te_3/Sb_2Te_3 superlattice. *Applied Physics A* **122**, 777 (2016).

34 Teitelbaum, S. W. *et al.* Direct measurement of anharmonic decay channels of a coherent phonon. *arXiv preprint arXiv:1710.02207* (2017).

35 Cho, G., Kütt, W. & Kurz, H. Subpicosecond time-resolved coherent-phonon oscillations in GaAs. *Phys. Rev. Lett.* **65**, 764 (1990).

36 Cheng, T. *et al.* Mechanism for displacive excitation of coherent phonons in Sb, Bi, Te, and Ti_2O_3. *Appl. Phys. Lett.* **59**, 1923-1925 (1991).

37 Scully, M. O. & Zubairy, M. S. *Quantum optics.* (Cambridge university press, 1997).

38 Matsumoto, Y. & Watanabe, K. Coherent vibrations of adsorbates induced by femtosecond laser excitation. *Chem. Rev.* **106**, 4234-4260 (2006).

39 Gardiner, C., Zoller, P. & Zoller, P. *Quantum noise: a handbook of Markovian and non-Markovian quantum stochastic methods with applications to quantum optics*. Vol. 56 (Springer Science & Business Media, 2004).

40 Hu, X. & Nori, F. Squeezed phonon states: modulating quantum fluctuations of atomic displacements. *Phys. Rev. Lett.* **76**, 2294 (1996).

41 Misochko, O. V. Nonclassical states of lattice excitations: squeezed and entangled phonons. *Physics-Uspekhi* **56**, 868 (2013).

42 Chaparro, T. & Ruben, K. Creation and detection of squeezed phonons in pump and probe experiments: a fully quantum treatment. (2015).

43 Braunstein, S. L. & Van Loock, P. Quantum information with continuous variables. *Rev. Mod. Phys.* **77**, 513 (2005).

44 Furusawa, A. *et al.* Unconditional quantum teleportation. *Science* **282**, 706-709 (1998).

45 Menicucci, N. C., Flammia, S. T. & Pfister, O. One-way quantum computing in the optical frequency comb. *Phys. Rev. Lett.* **101**, 130501 (2008).

46 Verhagen, E., Deléglise, S., Weis, S., Schliesser, A. & Kippenberg, T. J. Quantum-coherent coupling of a mechanical oscillator to an optical cavity mode. *Nature* **482**, 63 (2012).

47 Gröblacher, S., Hammerer, K., Vanner, M. R. & Aspelmeyer, M. Observation of strong coupling between a micromechanical resonator and an optical cavity field. *Nature* **460**, 724 (2009).

48 Okamoto, H. *et al.* Coherent phonon manipulation in coupled mechanical resonators. *Nature Physics* **9**, 480 (2013).

49 Yamaguchi, H., Okamoto, H. & Mahboob, I. Coherent control of micro/nanomechanical oscillation using parametric mode mixing. *Applied Physics Express* **5**, 014001 (2012).

50 Liu, Y.-C., Xiao, Y.-F., Chen, Y.-L., Yu, X.-C. & Gong, Q. Parametric down-conversion and polariton pair generation in optomechanical systems. *Phys. Rev. Lett.* **111**, 083601 (2013).

51 You, J. & Nori, F. Atomic physics and quantum optics using superconducting circuits. *Nature* **474**, 589 (2011).

52 Fainstein, A., Lanzillotti-Kimura, N. D., Jusserand, B. & Perrin, B. Strong optical-mechanical coupling in a vertical GaAs/AlAs microcavity for subterahertz phonons and near-infrared light. *Phys. Rev. Lett.* **110**, 037403 (2013).

53 Lo, C., Manousakis, E., Sollie, R. & Wang, Y. Correlated squeezed-state approach for the ground state of a system with strong electron-phonon interaction. *Phys. Rev. B* **50**, 418 (1994).

54 Hu, X. & Nori, F. Phonon squeezed states: quantum noise reduction in solids. *Physica B: Condensed Matter* **263**, 16-29 (1999).

55 Hussain, A. & Andrews, S. Absence of phase-dependent noise in time-domain reflectivity studies of impulsively excited phonons. *Phys. Rev. B* **81**, 224304 (2010).

56 Hu, X. & Nori, F. Phonon squeezed states generated by second-order Raman scattering. *Phys. Rev. Lett.* **79**, 4605 (1997).

57 Orbach, R. Nonlinear phonon generation. *Phys. Rev. Lett.* **16**, 15 (1966).

58 Klemens, P. Anharmonic decay of optical phonons. *Phys. Rev.* **148**, 845 (1966).

59 Fahy, S., Murray, É. D. & Reis, D. A. Resonant squeezing and the anharmonic decay of coherent phonons. *Phys. Rev. B* **93**, 134308 (2016).

60 Jusserand, B. & Cardona, M. in *Light Scattering in Solids V* 49-152 (Springer, 1989).

61 Laubereau, A. & Kaiser, W. Vibrational dynamics of liquids and solids investigated by picosecond light pulses. *Rev. Mod. Phys.* **50**, 607 (1978).

62 Yamanouchi, K., Agostini, P., Chin, S. L. & Ferrante, G. *Progress in Ultrafast Intense Laser Science II*. (Springer, 2015).

63 Begley, R., Harvey, A. & Byer, R. L. Coherent anti-Stokes Raman spectroscopy. *Appl. Phys. Lett.* **25**, 387-390 (1974).

64 Boyd, R. W. & Prato, D. *Nonlinear Optics*. (Elsevier Science, 2008).

65 Yan, Y. X., Gamble Jr, E. B. & Nelson, K. A. Impulsive stimulated scattering: General importance in femtosecond laser pulse interactions with matter, and

spectroscopic applications. *The Journal of chemical physics* **83**, 5391-5399 (1985).

66 Katsuki, H. *et al*. All-optical control and visualization of ultrafast two-dimensional atomic motions in a single crystal of bismuth. *Nat. Commun.* **4**, 3801 (2013).

67 Faist, J. *et al*. Quantum cascade laser. *Science* **264**, 553-556 (1994).

68 Köhler, R. *et al*. Terahertz semiconductor-heterostructure laser. *Nature* **417**, 156 (2002).

69 Williams, B. S. Terahertz quantum-cascade lasers. *Nat. Photonics* **1**, 517 (2007).

70 Harman, T., Taylor, P., Walsh, M. & LaForge, B. Quantum dot superlattice thermoelectric materials and devices. *Science* **297**, 2229-2232 (2002).

71 Maryam, W., Akimov, A. V., Campion, R. & Kent, A. Dynamics of a vertical cavity quantum cascade phonon laser structure. *Nat. Commun.* **4**, 2184 (2013).

72 Tamura, S., Hurley, D. C. & Wolfe, J. P. Acoustic-phonon propagation in superlattices. *Phys. Rev. B* **38**, 1427-1449 (1988).

73 Colvard, C., Merlin, R., Klein, M. & Gossard, A. Observation of folded acoustic phonons in a semiconductor superlattice. *Phys. Rev. Lett.* **45**, 298 (1980).

74 Colvard, C. *et al*. Folded acoustic and quantized optic phonons in (GaAl) As superlattices. *Phys. Rev. B* **31**, 2080 (1985).

75 Stroscio, M. A. & Dutta, M. *Phonons in nanostructures*. (Cambridge University Press, 2001).

76 Marder, M. P. *Condensed matter physics*. 163 (John Wiley & Sons, 2010).

77 Temnov, V. V. Ultrafast acousto-magneto-plasmonics. *Nat. Photonics* **6**, 728-736 (2012).

78 Maznev, A. *et al*. Broadband terahertz ultrasonic transducer based on a laser-driven piezoelectric semiconductor superlattice. *Ultrasonics* **52**, 1-4 (2012).

79 Kaviany, M. *Heat transfer physics*. (Cambridge University Press, 2014).

80 Wang, Y., Qiu, B., McGaughey, A. J., Ruan, X. & Xu, X. Mode-wise thermal conductivity of bismuth telluride. *Journal of Heat Transfer* **135**, 091102 (2013).

81 Wang, Y. & Xu, X. Molecular dynamics studies of ultrafast laser-induced nonthermal melting. *Applied Physics A* **110**, 617-621 (2013).

82 Zhang, Y. & Wang, Y. The effect of coherent optical phonon on thermal transport. *Applied Physics A* **117**, 2183-2188 (2014).

83 Chen, G. Size and interface effects on thermal conductivity of superlattices and periodic thin-film structures. *Journal of Heat Transfer* **119**, 220-229 (1997).

84 Xie, G., Ding, D. & Zhang, G. Phonon Coherence and Its Effect on Thermal Conductivity of Nanostructures. *arXiv preprint arXiv:1806.03401* (2018).

85 Cahill, D. G. *et al.* Nanoscale thermal transport. II. 2003–2012. *Applied Physics Reviews* **1**, 1, (2014).

86 Callaway, J. Model for lattice thermal conductivity at low temperatures. *Phys. Rev.* **113**, 1046 (1959).

87 Saha, B. *et al.* Phonon wave effects in the thermal transport of epitaxial TiN/(Al,Sc)N metal/semiconductor superlattices. *J. Appl. Phys.* **121**, 015109 (2017).

88 Lee, K. *et al.* Comparing phonon dephasing lifetimes in diamond using transient coherent ultrafast phonon spectroscopy. *Diamond and Related Materials* **19**, 1289-1295 (2010).

89 Hase, M., Mizoguchi, K., Harima, H., Nakashima, S.-i. & Sakai, K. Dynamics of coherent phonons in bismuth generated by ultrashort laser pulses. *Phys. Rev. B* **58**, 5448 (1998).

90 Ziman, J. M. *Electrons and phonons: the theory of transport phenomena in solids.* (Oxford university press, 1960).

91 Chen, G. Thermal conductivity and ballistic-phonon transport in the cross-plane direction of superlattices. *Phys. Rev. B* **57**, 14958 (1998).

92 Joshi, A. & Majumdar, A. Transient ballistic and diffusive phonon heat transport in thin films. *J. Appl. Phys.* **74**, 31-39 (1993).

93 Chiu, H.-Y. *et al.* Ballistic phonon thermal transport in multiwalled carbon nanotubes. *Phys. Rev. Lett.* **95**, 226101 (2005).

94 Luckyanova, M. N. *et al.* Coherent Phonon Heat Conduction in Superlattices. *Science* **338**, 936-939 (2012).

95 Venkatasubramanian, R., Siivola, E., Colpitts, T. & O'quinn, B. Thin-film thermoelectric devices with high room-temperature figures of merit. *Nature* **413**, 597-602 (2001).

96 Imamura, K., Tanaka, Y., Nishiguchi, N., Tamura, S. & Maris, H. Lattice thermal conductivity in superlattices: molecular dynamics calculations with a heat reservoir method. *Journal of Physics: Condensed Matter* **15**, 8679 (2003).

97 Ravichandran, J. *et al*. Crossover from incoherent to coherent phonon scattering in epitaxial oxide superlattices. *Nat. Mater.* **13**, 168-172 (2014).

98 Simkin, M. & Mahan, G. Minimum thermal conductivity of superlattices. *Phys. Rev. Lett.* **84**, 927 (2000).

99 Chen, Y., Li, D., Lukes, J. R., Ni, Z. & Chen, M. Minimum superlattice thermal conductivity from molecular dynamics. *Phys. Rev. B* **72**, 174302 (2005).

100 Garg, J. & Chen, G. Minimum thermal conductivity in superlattices: A first-principles formalism. *Phys. Rev. B* **87**, 140302 (2013).

101 Mu, X., Zhang, T., Go, D. B. & Luo, T. Coherent and incoherent phonon thermal transport in isotopically modified graphene superlattices. *Carbon* **83**, 208-216 (2015).

102 Zhu, T. & Ertekin, E. Phonon transport on two-dimensional graphene/boron nitride superlattices. *Phys. Rev. B* **90**, 195209 (2014).

103 Li, Q. & Ye, W. An interfering Monte Carlo method for partially coherent phonon transport in superlattices. *International Journal of Heat and Mass Transfer* **107**, 534-543 (2017).

104 Latour, B., Volz, S. & Chalopin, Y. Microscopic description of thermal-phonon coherence: From coherent transport to diffuse interface scattering in superlattices. *Phys. Rev. B* **90**, 014307 (2014).

105 Latour, B. & Chalopin, Y. Distinguishing between spatial coherence and temporal coherence of phonons. *Phys. Rev. B* **95**, 214310 (2017).

106 Cheaito, R. *et al*. Interplay between total thickness and period thickness in the phonon thermal conductivity of superlattices from the nanoscale to the microscale: Coherent versus incoherent phonon transport. *Phys. Rev. B* **97**, 085306 (2018).

107 Weiner, A. *Ultrafast optics*. Vol. 72 (John Wiley & Sons, 2011).

108 Kane, D. J. & Trebino, R. Characterization of arbitrary femtosecond pulses using frequency-resolved optical gating. *IEEE J. Quantum Electron.* **29**, 571-579 (1993).

109 Mane, R. & Lokhande, C. Chemical deposition method for metal chalcogenide thin films. *Materials Chemistry and Physics* **65**, 1-31 (2000).

110 Semonin, O. E. *et al.* Peak external photocurrent quantum efficiency exceeding 100% via MEG in a quantum dot solar cell. *Science* **334**, 1530-1533 (2011).

111 Beard, M. C. *et al.* Comparing multiple exciton generation in quantum dots to impact ionization in bulk semiconductors: implications for enhancement of solar energy conversion. *Nano Lett.* **10**, 3019-3027 (2010).

112 Feser, J. P., Chan, E. M., Majumdar, A., Segalman, R. A. & Urban, J. J. Ultralow thermal conductivity in polycrystalline CdSe thin films with controlled grain size. *Nano Lett.* **13**, 2122-2127 (2013).

113 Trindade, T., O'Brien, P. & Zhang, X.-m. Synthesis of CdS and CdSe nanocrystallites using a novel single-molecule precursors approach. *Chemistry of Materials* **9**, 523-530 (1997).

114 Wu, W. & Wang, Y. Ultrafast carrier dynamics and coherent acoustic phonons in bulk CdSe. *Opt. Lett.* **40**, 64-67 (2015).

115 Gupta, T. K. & Doh, J. Optical properties of polycrystalline CdSe films. *J. Mater. Res.* **7**, 1243-1246 (1992).

116 Freik, D., Nykyruy, L., Parashchuk, T. & Volochanska, B. Thermodynamic Properties of CdSe crystals using first principles calculations and experiment. *Int. J. Eng. Innovative Technol.(IJEIT)* **4**, 90-104 (2014).

117 Jia-Jin, T., Yan, C., Wen-Jun, Z. & Qing-Quan, G. Elastic and thermodynamic properties of CdSe from first-principles calculations. *Communications in Theoretical Physics* **50**, 220 (2008).

118 Teisseyre, H. *et al.* Temperature dependence of the energy gap in GaN bulk single crystals and epitaxial layer. *J. Appl. Phys.* **76**, 2429-2434 (1994).

119 Wu, J. *et al.* Temperature dependence of the fundamental band gap of InN. *J. Appl. Phys.* **94**, 4457-4460 (2003).

120 Jammalamadaka, S. N. *et al.* Martensite-like transition and spin-glass behavior in nanocrystalline $Pr_{0.5}Ca_{0.5}MnO_3$. *AIP Advances* **1**, 042151 (2011).

121 Sokolowski-Tinten, K., Schulz, H., Bialkowski, J. & von der Linde, D. Two distinct transitions in ultrafast solid-liquid phase transformations of GaAs. *Applied Physics A* **53**, 227-234 (1991).

122 Rousse, A. *et al*. Non-thermal melting in semiconductors measured at femtosecond resolution. *Nature* **410**, 65 (2001).

123 Sokolowski-Tinten, K. *et al*. Femtosecond X-ray measurement of coherent lattice vibrations near the Lindemann stability limit. *Nature* **422**, 287 (2003).

124 Waldecker, L. *et al*. Time-domain separation of optical properties from structural transitions in resonantly bonded materials. *Nat. Mater.* **14**, 991 (2015).

125 Callan, J. *et al*. Ultrafast laser-induced phase transitions in amorphous GeSb films. *Phys. Rev. Lett.* **86**, 3650 (2001).

126 Kim, J. & Na, S. Metal thin film ablation with femtosecond pulsed laser. *Optics & Laser Technology* **39**, 1443-1448 (2007).

127 Gajdardziska-Josifovska, M., Lazarov, V., Reynolds, J. & Yakovlev, V. Wavelength dependence of laser-induced phase transformations in semiconductor quantum dots. *Appl. Phys. Lett.* **78**, 3298-3300 (2001).

128 Guo, L., Hodson, S. L., Fisher, T. S. & Xu, X. Heat transfer across metal-dielectric interfaces during ultrafast-laser heating. *Journal of Heat Transfer* **134**, 042402 (2012).

129 Vengurlekar, A., Prabhu, S., Roy, S. & Shah, J. Large reduction in hot-carrier energy-loss rates in cdse caused by nonequilibrium optical phonons. *Phys. Rev. B* **50**, 15461 (1994).

130 Othonos, A. Probing ultrafast carrier and phonon dynamics in semiconductors. *J. Appl. Phys.* **83**, 1789-1830 (1998).

131 Venkatasubramanian, R., Colpitts, T., Watko, E., Lamvik, M. & El-Masry, N. MOCVD of Bi_2Te_3, Sb_2Te_3 and their superlattice structures for thin-film thermoelectric applications. *J. Cryst. Growth* **170**, 817-821 (1997).

132 Touzelbaev, M., Zhou, P., Venkatasubramanian, R. & Goodson, K. Thermal characterization of Bi_2Te_3/Sb_2Te_3 superlattices. *J. Appl. Phys.* **90**, 763-767 (2001).

133 Venkatasubramanian, R. Lattice thermal conductivity reduction and phonon localizationlike behavior in superlattice structures. *Phys. Rev. B* **61**, 3091 (2000).

134 Venkatasubramanian, R. *et al*. Low-temperature organometallic epitaxy and its application to superlattice structures in thermoelectrics. *Appl. Phys. Lett.* **75**, 1104-1106 (1999).

135 Wang, Y., Liebig, C., Xu, X. & Venkatasubramanian, R. Acoustic phonon scattering in Bi_2Te_3/Sb_2Te_3 superlattices. *Appl. Phys. Lett.* **97**, 083103 (2010).

136 Gale, J. D. & Rohl, A. L. The general utility lattice program (GULP). *Molecular Simulation* **29**, 291-341 (2003).

137 Yang, X. *et al*. Raman spectroscopy determination of the Debye temperature and atomic cohesive energy of CdS, CdSe, Bi_2Se_3, and Sb_2Te_3 nanostructures. *J. Appl. Phys.* **112**, 083508 (2012).

138 Giraud, S. & Egger, R. Electron-phonon scattering in topological insulators. *Phys. Rev. B* **83**, 245322 (2011).

139 Giraud, S., Kundu, A. & Egger, R. Electron-phonon scattering in topological insulator thin films. *Phys. Rev. B* **85**, 035441 (2012).

140 Yamamoto, A., Mishina, T., Masumoto, Y. & Nakayama, M. Coherent Oscillation of Zone-Folded Phonon Modes in GaAs-AlAs Superlattices. *Phys. Rev. Lett.* **73**, 740-743 (1994).

141 Maznev, A. *et al*. Lifetime of sub-THz coherent acoustic phonons in a GaAs-AlAs superlattice. *Appl. Phys. Lett.* **102**, 041901 (2013).

142 Hofmann, F. *et al*. Intrinsic to extrinsic phonon lifetime transition in a GaAs–AlAs superlattice. *Journal of Physics: Condensed Matter* **25**, 295401 (2013).

143 Mizoguchi, K. *et al*. Umklapp process in observation of coherent folded longitudinal acoustic phonons in a GaAs/AlAs long-period superlattice. *Physica E: Low-dimensional Systems and Nanostructures* **21**, 646-650 (2004).

144 Mizoguchi, K., Hase, M., Nakashima, S. & Nakayama, M. Observation of coherent folded acoustic phonons propagating in a GaAs/AlAs superlattice by two-color pump-probe spectroscopy. *Phys. Rev. B* **60**, 8262 (1999).

145 Madelung, O. *Semiconductors: Group IV Elements and III-V Compounds*. (Springer Berlin Heidelberg, 2012).

146 Jusserand, B., Alexandre, F., Paquet, D. & Le Roux, G. Raman scattering characterization of interface broadening in GaAs/AlAs short period superlattices grown by molecular beam epitaxy. *Appl. Phys. Lett.* **47**, 301-303 (1985).

147 Capinski, W. *et al*. Thermal-conductivity measurements of GaAs/AlAs superlattices using a picosecond optical pump-and-probe technique. *Phys. Rev. B* **59**, 8105 (1999).

148 Luckyanova, M. N. *et al*. Anisotropy of the Thermal Conductivity in GaAs/AlAs Superlattices. *Nano Lett.* **13**, 3973-3977 (2013).

149 Tamura, S.-i., Tanaka, Y. & Maris, H. J. Phonon group velocity and thermal conduction in superlattices. *Phys. Rev. B* **60**, 2627 (1999).

150 Luckyanova, M. N. *et al*. Phonon Localization in Heat Conduction. *arXiv preprint arXiv:1602.05057* (2016).

151 Aspnes, D., Kelso, S., Logan, R. & Bhat, R. Optical properties of Al x Ga1− x As. *J. Appl. Phys.* **60**, 754-767 (1986).

152 Maznev, A. A. *et al*. Lifetime of sub-THz coherent acoustic phonons in a GaAs-AlAs superlattice. *Appl. Phys. Lett.* **102**, 041901 (2013).

153 Auston, D. H. *et al*. *Ultrashort laser pulses and applications*. Vol. 60 (Springer Science & Business Media, 2013).

154 von Hoegen, A., Mankowsky, R., Fechner, M., Först, M. & Cavalleri, A. Probing the interatomic potential of solids with strong-field nonlinear phononics. *Nature* **555**, 79 (2018).

155 Misochko, O., Lebedev, M. V. & Ishioka, K. in *International Conference on Ultrafast Phenomena*. 09. Wed. P03. 31 (Optical Society of America).

156 Semenov, A. Collapse and revival of photoinduced oscillations in the optical reflectivity of bismuth. *Journal of Experimental and Theoretical Physics* **122**, 277-282 (2016).

157 Henighan, T. *et al*. Control of two-phonon correlations and the mechanism of high-wavevector phonon generation by ultrafast light pulses. *Phys. Rev. B* **94**, 020302 (2016).

158 Liedberg, B., Nylander, C. & Lunström, I. Surface plasmon resonance for gas detection and biosensing. *Sensors and actuators* **4**, 299-304 (1983).

159 Homola, J., Yee, S. S. & Gauglitz, G. Surface plasmon resonance sensors. *Sensors and Actuators B: Chemical* **54**, 3-15 (1999).

160 Davis III, L. & Deutsch, M. Surface plasmon based thermo-optic and temperature sensor for microfluidic thermometry. *Rev. Sci. Instrum.* **81**, 114905 (2010).

161 Akowuah, E. K., Gorman, T. & Haxha, S. Design and optimization of a novel surface plasmon resonance biosensor based on Otto configuration. *Optics express* **17**, 23511-23521 (2009).

162 Wu, S., Ho, H., Law, W., Lin, C. & Kong, S. Highly sensitive differential phase-sensitive surface plasmon resonance biosensor based on the Mach–Zehnder configuration. *Opt. Lett.* **29**, 2378-2380 (2004).

163 Nuster, R., Paltauf, G. & Burgholzer, P. Comparison of surface plasmon resonance devices for acoustic wave detection in liquid. *Optics express* **15**, 6087-6095 (2007).

164 Katayama, K., Sawada, T., Shen, Q. & Harata, A. Detection of photoinduced electronic, thermal, and acoustic dynamics of gold film using a transient reflecting grating method under three types of surface plasmon resonance conditions. *Phys. Rev. B* **58**, 8428 (1998).

165 Wang, J. & Guo, C. Effect of electron heating on femtosecond laser-induced coherent acoustic phonons in noble metals. *Phys. Rev. B* **75**, 184304 (2007).

166 Brüggemann, C. *et al.* Modulation of a surface plasmon-polariton resonance by subterahertz diffracted coherent phonons. *Phys. Rev. B* **86**, 121401 (2012).

167 Devizis, A., Vaicikauskas, V. & Gulbinas, V. Ultrafast pump-probe surface plasmon resonance spectroscopy of thin gold films. *Appl. Opt.* **45**, 2535-2539 (2006).

168 Chen, Z. & DeCamp, M. F. Measuring optical phonon dynamics in a bismuth thin film through a surface plasmon resonance. *J. Appl. Phys.* **112**, 013527 (2012).

169 Yamaguchi, S. & Tahara, T. Coherent acoustic phonons in a thin gold film probed by femtosecond surface plasmon resonance. *Journal of Raman Spectroscopy* **39**, 1703-1706 (2008).

170 Kolomenskii, A. A., Mueller, R., Wood, J., Strohaber, J. & Schuessler, H. A. Femtosecond electron-lattice thermalization dynamics in a gold film probed by pulsed surface plasmon resonance. *Appl. Opt.* **52**, 7352-7359 (2013).

171 Temnov, V. V. *et al.* Femtosecond surface plasmon interferometry. *Optics express* **17**, 8423-8432 (2009).

172 Patskovsky, S., Bah, S., Meunier, M. & Kabashin, A. V. Characterization of high refractive index semiconductor films by surface plasmon resonance. *Appl. Opt.* **45**, 6640-6645 (2006).

173 Paliwal, A., Sharma, A., Tomar, M. & Gupta, V. Optical properties of WO_3 thin films using surface plasmon resonance technique. *J. Appl. Phys.* **115**, 043104 (2014).

174 Chiang, H. *et al.* Effects of temperature on the surface plasmon resonance at a metal–semiconductor interface. *Thin Solid Films* **515**, 6953-6961 (2007).

175 Temnov, V. V. *et al.* Femtosecond nonlinear ultrasonics in gold probed with ultrashort surface plasmons. *Nat. Commun.* **4**, 1468 (2013).

176 Campion, A. & Kambhampati, P. Surface-enhanced Raman scattering. *Chemical society reviews* **27**, 241-250 (1998).

177 Maier, S. A. *Plasmonics: fundamentals and applications*. (Springer Science & Business Media, 2007).

178 Born, M. & Wolf, E. Fundamentals of optics. *M: Nayka* (1973).

179 Fontana, E., Kim, J.-M., Llamas-Garro, I. & Cavalcanti, G. O. Microfabricated Otto chip device for surface plasmon resonance-based optical sensing. *Appl. Opt.* **54**, 9200-9204 (2015).